

Die approbierte Originalversion dieser Dissertation ist an der Hauptbibliothek der Technischen Universität Wien aufgestellt (<http://www.ub.tuwien.ac.at>).

The approved original version of this thesis is available at the main library of the Vienna University of Technology (<http://www.ub.tuwien.ac.at/englweb/>).

First-Principle Studies on Quasi 1-Dimensional Structures on Pt(110) Surfaces

A Dissertation Submitted in Fulfillment
of the Requirements for the Degree of
DOKTOR DER TECHNISCHEN WISSENSCHAFTEN
in the Technische Universität Wien,
Technisch-Naturwissenschaftliche Fakultät

under supervision of
Ao. Prof. Dipl.-Ing. Dr. techn. Josef Redinger
E134
Institut für Allgemeine Physik

by
Rinaldo Zucca

Vienna, 26 march 2008

Ai miei genitori

Abstract

Halogens interact strongly with metal surfaces and are also known to form halogen-bridged transition metal linear-chain compounds. These are two reasons that make halogens on anisotropic transition metal surfaces interesting systems to study low-dimensional phenomena, even more so if one considers the well-known tendency of the linear-chain compounds to form competing ground states as a result of a delicate balance between various interactions. A microscopic control of these interactions should allow to switch between many different phases and reveal the extraordinary potential of low-dimensional systems in materials design and development. Preliminarily, a compared analysis of halogen adsorption with a coverage of $1/2$ of a ML was performed. While Cl is found both experimentally and theoretically in a stable $p(2\times 1)$ phase and calculations provide a global $c(2\times 2)$ phase for I, for Br both phases are energetically degenerate. The brominated surface appears in a global $c(2\times 2)$ phase at room temperature and undergoes fluctuations and phase separation at low temperature. A theoretical study of the next-neighbour interactions allowed a deeper insight in the phenomenon.

The further adsorption of Br on the quasi one-dimensional $c(2\times 2)$ phase causes the system to go through a succession of complex phases, comprising not only commensurate, long-range-ordered structures. By means of DFT calculations, together with data supplied by quantitative LEED, the structure of the commensurate phases (3×1) at $2/3$ ML Br and (4×1) at $3/4$ ML Br coverage were analysed. While for $c(2\times 2)$ only short-bridge sites are occupied leading to Br-Pt chains along the dense packed Pt rows, also long-bridge sites are populated for the other two. Also a further adsorption on Cl both on the Cl- $p(2\times 1)$ and on the Br- $c(2\times 2)$ phase causes similar transitions.

A similar succession of complex phases is also triggered by adsorption of CO and NO. Various mixed CO/Br (NO/Br) phases on Pt(110) at increasing CO(NO) coverages were analysed. It is thus possible to show that although excess CO behaves quite similar to Br, there are differences which shed new light on the experimental evidence.

The hydrogen-modified missing-row Pt(110) surface can be used as a template for the growth of one-dimensional adsorbate structures. Contrary to all former assignments, the present DFT study, together with LEED data, allows to conclude that at 1/2 ML coverage Hydrogen chemisorbs on atypically low coordinated adsorption positions above the outermost close-packed rows. Adsorption sites on the (111) microfacets are occupied only at higher coverage. Subsurface adsorption sites are ruled out.

Kurzfassung

Halogene interagieren stark mit Metalloberflächen. Bedenkt man die bekannte Neigung von linearen Metall-Halogen Kettenverbindungen zu konkurrierenden Grundzuständen, die das Resultat einer delikaten Balance zwischen verschiedenen Wechselwirkungen sind, so erkennt man, dass Halogenadsorbate auf anisotropen Metalloberflächen interessante Systeme zur Studie von quasi eindimensionalen Phänomenen abgeben können.

Eine vergleichende experimentelle und theoretische Analyse mittels DFT Rechnungen von $1/2$ Monolage Halogen adsorbiert auf Pt(110) zeigte, dass Cl eine $p(2 \times 1)$ und I eine $c(2 \times 2)$ Phase ausbilden; im Falle von Br ergibt sich, dass die globale $c(2 \times 2)$ Raumtemperaturphase fluktuiert und beim Abkühlen in $p(2 \times 1)$, $c(2 \times 2)$ und $p(3 \times 2)$ artige Phasen zerfällt, die die gleiche Bedeckung aufweisen, und wie DFT Rechnungen zeigen bei tiefen Temperaturen energetisch entartet sind.

Weitere Adsorption von Br auf der $c(2 \times 2)$ Raumtemperaturphase ruft eine Abfolge von komplexen langreichweitig geordneten Strukturen hervor. Die Strukturen der kommensurablen Strukturen $p(3 \times 1)$ bei $2/3$ ML und $p(4 \times 1)$ bei $3/4$ ML Br Bedeckung wurden analysiert mittels Kombination von LEED und DFT Rechnungen. Ähnliche strukturelle Abfolgen wurden auch für eine weitere Adsorption von Cl sowohl auf einer $p(2 \times 1)$ -Cl als auch auf einer $c(2 \times 2)$ -Br Phase untersucht.

Ein solches Verhalten wird auch durch eine Adsorption von CO(NO) auf einer Br Phase mit $1/2$ ML Bedeckung hervorgerufen. Verschiedene CO/Br (NO/Br) Mischphasen wurden für steigende CO(NO) Bedeckungen mittels DFT Rechnungen analysiert. Wie die Rechnungen zeigten, verhält sich überschüssiges CO ähnlich zu Br, obwohl Unterschiede auftreten, welche die experimentellen Resultate in neuem Licht erscheinen lassen.

Zum Schluss wurde die rekonstruierte mit Wasserstoff modifizierte Pt(110) Oberfläche untersucht, die ebenfalls als Template zum Wachsen eindimensionaler Adsorbatstrukturen verwendet werden kann. Im Gegensatz zu allen früheren Festlegungen, bestätigen die vorliegenden DFT Rechnungen neue LEED Modelle, die für eine 1/2 ML Wasserstoffbedeckung einen atypische Adsorptionsplatz auf den obersten niedrig koordinierten und dichtgepackten Pt Reihen fanden.

Contents

1	Theory and Methods	4
1.1	Density Functional Theory	4
1.2	Vienna <i>Ab initio</i> Simulation Package	10
1.3	Scanning tunnelling Microscopy	14
1.4	Low Energy Electron Diffraction	18
1.5	Computational Details	19
2	Halogen adsorption on Pt(110), low coverages	21
2.1	The Clean Pt(110) Surface	22
2.2	Halogens on the unreconstructed Pt(110) surface	28
2.2.1	1/4 ML Coverage: The Single Halogen Approximation	28
2.2.2	1/2 ML Coverage, General Trends	30
2.3	Br/Pt(110): Fluctuations and Phase Separation	32
2.3.1	Geometry	33
2.3.2	Electronic Properties	33
2.3.3	Fluctuations and phase separations: Experimental Evidence	34
2.3.4	Discussion	40
2.4	Cl/Pt(110): A Global p(2×1) Phase	45
2.4.1	Geometry	46
2.4.2	Electronic Properties	47

2.5	I/Pt(110): A Global SB-c(2×2) Phase	48
3	Halogens on Pt(110), high coverages	51
3.1	Bromine on Platinum	51
3.1.1	Experimental Evidence	51
3.1.2	Interpretation: The Global Br-(3×1) Phase	54
3.1.3	The Br-(4×1) Phase	58
3.1.4	Conclusions	65
3.2	Chlorine on Platinum	66
3.2.1	Experimental Evidence	66
3.2.2	DFT Interpretation: The Pure (3×1) and (4×1) Phases	67
3.2.3	The Cl-(4×2) Phase	69
3.2.4	Cl Adsorption on c(2×2)-Br/Pt(110)	72
4	Adsorption of CO and NO on Pt(110)	78
4.1	CO and NO Adsorption on a Clean Pt(110) Surface	78
4.2	Mixed Adsorption CO (NO) with Br	84
4.3	CO, NO adsorption on the c(2×2)-Br/Pt(110) Surface	85
4.3.1	Experimental Evidence	86
4.3.2	Discussion	92
5	Hydrogen adsorption on Pt(110)	102
5.1	Computational Details	103
5.2	Discussion	104
5.2.1	The β_2 Surface	106
5.2.2	Higher Coverages	114
5.2.3	Conclusions	119

List of Figures

1.1	Schematic picture of tunnelling geometry	17
2.1	Representation of the ideal and MR-reconstructed Pt surface unit cell	23
2.2	Relaxation parameters of the unreconstructed Pt surface	24
2.3	Pairings of the MR-Pt-(1×2) surface	25
2.4	Bucklings of the MR-Pt-(1×2) surface	26
2.5	Relaxation parameters of the MR-reconstructed Pt surface	26
2.6	Adsorption sites on the (1×1)-Pt(110) surface	28
2.7	Single-adsorbate approximation	29
2.8	Adsorption arrangements with 1/2 ML halogen coverage	31
2.9	The (3×2) 1/2 ML halogen phase	33
2.10	Comparison between the p states of Br and the d states of Pt	35
2.11	DOS of the p states of Br in the SB-c(2×2) phase	36
2.12	Electronical structure of the bonding	37
2.13	LEED spot-profile analysis of the 1/2 ML Br system	38
2.14	1/2 ML Br on Pt upon cooling: STM images	39
2.15	1/2 ML Br on Pt structures, vibrational potentials	41
2.16	Generic phase diagram of quasi-1D systems.	43
2.17	Coexisting Br phases at low temperature	45
2.18	Comparison between the p states of Cl and the d states of Pt	47

2.19	DOS of the p states of Cl in the SB- $p(2\times 1)$ phase	48
2.20	LT-STM ($T \simeq 110$ K) images of $p(2\times 1)$ -Cl/Pt(110)	49
2.21	Charge densities of the Cl- and Br- $p(2\times 1)$ structures	49
3.1	STM pictures for a Br coverage slightly above $1/2$ ML	52
3.2	STM pictures of global (3×1) -Br/Pt(110) phase	53
3.3	STM picture of (4×1) -Br/Pt(110)	53
3.4	Potential barrier in the (3×1) phase	54
3.5	Ball scheme of the (3×1) -Br/Pt(110)	56
3.6	Br- (3×1) phase: Density of states	57
3.7	experimental and VASP-calculated STM images of the Br/Pt(110)- $p(3\times 1)$ surface	59
3.8	Br- (4×1) arrangements	60
3.9	Geometry of the (4×1) -Br/Pt(110) surface	60
3.10	Br/Pt(110)- $p(4\times 1)$ phase: LEED intensity versus energy	62
3.11	Br- (4×1) phase: Density of states	63
3.12	experimental and VASP-calculated STM images of the Br/Pt(110)- $p(4\times 1)$ surface	64
3.13	RT-STM images of high coverage Cl on Pt	66
3.14	Cl- (3×1) phase: Density of states	68
3.15	Ball model of the (4×2) -PtCl ₄ /Cl/Pt(110) adsorbate system	71
3.16	Energies per cell of various arrangements with (4×2) periodicity	72
3.17	Experimental and simulated RT-STM images of (4×2) -PtCl ₄ /Cl/Pt	73
3.18	RT-STM: (3×1) -Cl Br/Pt(110)	74
3.19	LT-STM (~ 110 K): (3×1) -Cl Br/Pt(110)	75
3.20	Ball scheme for the mixed systems BrCl/Pt(110)	76
4.1	Adsorption sites on the MR and on the (1×1) Pt surface	79

4.2	CO(NO) vs. Br	81
4.3	CO (NO) Diffusion barrier	82
4.4	Difference between the adsorption energy on SB and T sites	83
4.5	Br-CO (NO) interactions	84
4.6	CO (NO)-Br adsorbate-adsorbate interactions	85
4.7	LEED pictures of the $c(2\times 2) \Rightarrow (3\times 1)$ phase transition	86
4.8	RT-STM pictures of the $c(2\times 2) \Rightarrow (3\times 1)$ phase transition	87
4.9	LT-STM image of CO on $c(2\times 2)$ -Br/Pt(110)	88
4.10	STM images acquired during the adsorption of NO on the $c(2\times 2)$ - Br/Pt(110) at RT	89
4.11	RT-STM images showing the transition from a (3×1) to a (4×1) phase	90
4.12	The (3×1) phase is transformed into an array of (3×1) antiphase domains	91
4.13	CO (NO) induced $c(2\times 2) \Rightarrow (3\times 1) \Rightarrow (4\times 1)$ phase transition	94
4.14	Estimation of the CO critical coverage	96
4.15	comparison between the global (3×1) phase, right the alternate (4×1) - bare soliton Br-CO (NO) phase	97
4.16	The compound (7×1) -CO (NO)/Br phase	98
4.17	The (4×1) -CO (NO)/Br phase	99
4.18	Experimental and calculated STM images of the CO (NO)-induced (4×1) phase	100
4.19	Calculated charge density of a CO (NO)-induced (4×1) phase	101
5.1	TPD spectra for D_2	104
5.2	I/V curves for the $(1, 1/2)$ beam of the clean and β_2 surface	105
5.3	Model of the Pt atom geometry on clean and hydrogen-modified H/Pt(110) (1×2) surfaces	107

5.4	fig 3	109
5.5	Calculated density of states image of the β_2 surface	110
5.6	fig 5	112
5.7	Adsorption energy calculated for different distances from the SB ad- sorption site on the Pt row	113
5.8	Adsorption energies along three representative surface lines from the Pt-row to the groove	115
5.9	TPD spectra of H ₂ with and without preadsorption of CO	116
5.10	LEED diffraction patterns at T = 130 K and 49 eV electron energy after various D ₂ exposures	118
5.11	DFT adsorption energies for H on (1×2) Pt(110)	119

List of Tables

2.1	Changes in interlayer spacings of the unreconstructed Pt(110) surface	25
2.2	Experimental and theoretical results for the missing-row Pt(110) surface	27
2.3	Binding energy per Pt atom	27
2.4	low coverage halogens adsorption, general trends	30
2.5	Adsorption energies and bondlengths of the 1/2 ML arrangements . .	32
2.6	DFT and LEED results for the Br/Pt(110)-c(2×2) phase	34
2.7	Structural parameters of the Cl/Pt(110)-p(2×1) phase	46
2.8	Structural parameters of the I/Pt(110)-c(2×2) phase	50
3.1	Structural characterisation of the (3×1) structure	58
3.2	Geometrical characterisation of the Br-(4×1) phase	61
3.3	Comparison of the Cl- and Br-(3×1) structures	67
3.4	Adsorption energy of the Cl-(4×1) structure	69
4.1	Adsorption energies and bondlengths for 1/4 ML CO (NO) adsorption on Pt(110)	80
4.2	Comparison of the (3×1)-phase and (4×1)-phases adsorption energies	95
5.1	Structural data Pt(110)-MR	108
5.2	Interlayer spacing and adsorption energies relative to the short bridge site of the β_2 surface	111

Introduction

The determination of the surface structure and adsorption energetics is a key issue in surface science. The chemisorption of reactants may cause dramatic modifications of the substrate like relaxations and reconstructions, which strongly modify the properties of the system. DFT based approaches as well as STM and LEED techniques are very powerful tools to investigate the geometrical and electronic structure of both adsorbate and substrate, but only the combined application of theoretical and experimental studies provides a complete picture of this complex problem.

Low dimensional materials display a rich and technologically highly interesting phase diagram [1]. The dimensionality determines the strength of the many-body effects, in particular dimensional reduction introduces strong correlation even in materials which are uncorrelated in the extended bulk. Consequently, it determines the macroscopic materials properties [2, 3]. Strongly anisotropic single crystal surfaces and their adsorbate-covered, reconstructed or stepped modifications are promising templates for the design and characterisation of one-dimensional systems on surfaces [4]

The interaction of halogens with transition metal surfaces has received much attention recently for practical reasons concerning electrochemistry, heterogeneous catalysis and corrosion, as well as for fundamental aspects like halogen-induced competing ground states. Halogen atoms, as strong adsorbates modifying the atomic positions and the charge distribution of the surface, efficiently poison several cat-

alytic reactions, but are also used as promoters in particular cases. On the other hand the halogen adsorption on anisotropic surfaces like the Pt(110) surface was found to represent a system with good prospects for the investigation of low dimensional phenomena on surfaces.

A modulation of the surface geometry can also be caused by the co-deposition of different adatom species. By adsorption of CO or NO on a pre-halogenated Pt(110) surface different phases are indeed observed as a function of the adsorbate coverage. A study of such adsorption allows also to determine of halogens on catalytic reactions.

Also the hydrogen modified Pt(110) surface can be used as a template for the growth of one-dimensional adsorbate structures with atypical characteristics as a low correlated chemisorption site on the outmost close-packed rows.

Layout of the Thesis

The thesis is organised in the following way.

1. In the first chapter a brief summary of the theoretical background of the Vienna Ab-initio Simulation Package (VASP) is given. The Tersoff-Hamann approach used for calculating STM images and the Low Energy Electron Diffusion experimental method are also shortly described.
2. The second and third chapters are dedicated to the adsorption of halogens on a Pt(110) surface: chapter 2 is about the clean Pt surface and halogen adsorption up to 1/2 monolayer, while chapter 3 is focused on the adsorption of Br and Cl at higher coverages.
3. In the fourth chapter the adsorption of CO and NO both on the clean Pt(110) and on the prehalogenated Br/Pt(110) surfaces is treated.
4. In the fifth chapter the adsorption of H on the Pt(110) surface is described.

5. General conclusions are reported in the sixth chapter.

Chapter 1

Theory and Methods

1.1 Density Functional Theory

The main theoretical problem in solid state physics is the solution of the many body Schrödinger equation $\hat{H}|\psi\rangle = \varepsilon|\psi\rangle$. In this respect first principles methods, based on density functional theory (DFT) within all its approximations, proved to be reliable and computationally tractable tools.

The Hamiltonian of the Schrödinger equation which must be solved to determine the physical properties of a system of N interacting electrons in an external potential V_{ext} has the form:

$$\hat{H} = \hat{T} + \hat{V}_{ext} + \hat{U} \quad (1.1)$$

where $\hat{T} = -\sum_{j=1}^N \frac{\hbar^2}{2m} \nabla_j^2$ is the kinetic energy of the electrons, $\hat{V}_{ext} = \sum_{j=1}^N v(\mathbf{r}_j)$ the external potential generated by the ions ($-\frac{Ze^2}{r_j}$) and any other possible additional source, and $\hat{U} = \frac{1}{2} \sum_{j,k=1, j \neq k}^N \frac{e^2}{|\mathbf{r}_j - \mathbf{r}_k|}$ the electron-electron interaction. The solution of such an equation turns out to be impossible for two reasons: first, the presence of an interaction term in the Hamiltonian, which can not be treated analytically, and second, because the wavefunction depends on $3N$ ($4N$ if including spins) independent coordinates. In the case of the nitrogen atom one must deal with 7 electrons and therefore 21 coordinates, assuming roughly 10 entries per coordinate and 4 bytes per

entry it results in 4×10^{21} bytes. A common CD can store 7×10^8 bytes so it turns out that to store the wavefunction of the nitrogen atom one needs $\sim 6 \times 10^{12}$ CDs or 4 milliards 1 Tbyte-HDs. This is clearly a quantity of data that can not technically be dealt with.

An alternative way to obtain a solution to the many body problem is given by Density Functional Theory (DFT) originally proposed by Hohenberg and Kohn [5] and Kohn and Sham [6] the essence of which can be summarised as follows:

- Every observable quantity of a stationary quantum mechanical system is determined by the ground-state density alone. (Hohenberg-Kohn, H-K theorem)
- The ground-state density of the interacting system of interest can be determined by calculating the ground-state density of a connected non-interacting system. (Kohn-Sham, K-S theorem)

The H-K theorem asserts that not only an external potential V_{ext} determines via solution of the Schrödinger equation, the wavefunction Ψ and therefore the electron density $n(\mathbf{r}) = \langle \Psi | n(\hat{r}) | \Psi \rangle$, but that a potential that determines a given density n is unique. Hohenberg and Kohn prove that the relation between the external potential and the electronic density is surjective and injective, and thus fully invertible.

The existence of the inverse mapping $n \rightarrow \Psi \rightarrow V_{ext}$ allows to assert that the ground state expectation value of any observable is a unique functional of the exact ground state density. The H-K theorem concludes by proving that the exact ground state density can be determined by minimisation of the variational functional

$$E[n] = \langle \Psi[n] | \hat{T} + \hat{V}_{ext} + \hat{U} | \Psi[n] \rangle, \quad E_0 = \min_{n \in \mathcal{N}} (E[n]) \quad (1.2)$$

which can be written as:

$$E[n] = F[n] + \langle \Psi[n] | \hat{V}_{ext} | \Psi[n] \rangle \quad (1.3)$$

with

$$F[n] = \langle \Psi[n] | \hat{T} + \hat{U} | \Psi[n] \rangle \quad (1.4)$$

Since $F[n]$ does not depend on the external potential \hat{V}_{ext} it is an universal functional, $F[n]$ is thus the same density functional for atoms, molecules and solids since \hat{U} , in all cases, it represents the Coulomb repulsion between the electrons.

The variational principle of Hohenberg and Kohn allows the determination of the exact ground state density of a specific many-particles system, but does not describe the route to it. In order to find the electronic density of a physical system the Kohn-Sham theorem can be used, that asserts that the ground state density of the interacting system of interest is the same as the ground state density of non-interacting particles moving in an effective potential $V_{KS}[n](\mathbf{r})$, depending on the density n . The K-S orbitals of the system (one-electron wavefunctions) obey the one-particle Schrödinger equation:

$$\left(-\frac{\hbar^2 \nabla^2}{2m} + V_{KS}[n](\mathbf{r}) \right) \phi_j(\mathbf{r}) = \varepsilon_j \phi_j(\mathbf{r}) \quad (1.5)$$

The ground state density is then:

$$n(\mathbf{r}) = \sum_{j=1}^N |\phi_j(\mathbf{r})|^2, \quad (1.6)$$

for the lowest ε_j , with N total number of particles. Equations 1.5 and 1.6 are the well known Kohn-Sham equations.

From $n(\mathbf{r})$, it is possible to derive the classical Coulomb energy for an electronic system, known as Hartree term $E_H[n]$:

$$E_H[n] = \frac{1}{2} \iint d\mathbf{r} d\mathbf{r}' \frac{n(\mathbf{r})n(\mathbf{r}')}{|\mathbf{r} - \mathbf{r}'|} = \frac{1}{2} \int d\mathbf{r} V_H(\mathbf{r})n(\mathbf{r}) \quad (1.7)$$

The kinetic energy of the non-interacting system is defined as:

$$T_s[n] = -\frac{\hbar^2}{2m} \sum_{j=1}^N \langle \phi_j | \nabla^2 | \phi_j \rangle, \quad (1.8)$$

for the lowest ε_j .

The density functional $F[n]$ can be written through equations 1.7 and 1.8 in the form:

$$F[n] = T_s[n] + E_H[n] + E_{xc}[n] \quad (1.9)$$

which implicitly defines the so called exchange and correlation functional $E_{xc}[n]$ as [7, 8]:

$$E_{xc}[n] = \frac{1}{2} \iint d\mathbf{r} d\mathbf{r}' n(\mathbf{r}) \frac{n_{xc}(\mathbf{r}, \mathbf{r}')}{|\mathbf{r} - \mathbf{r}'|} \quad (1.10)$$

where n_{xc} is the exchange-correlation hole, representing the depletion of the electronic density at \mathbf{r} due to the presence of an electron located in \mathbf{r}' and satisfies the following conditions:

- The exchange-correlation hole is a local modification of the density, it vanishes at large distances from \mathbf{r} :

$$\lim_{|\mathbf{r}-\mathbf{r}'| \rightarrow \infty} n_{xc}(\mathbf{r}, \mathbf{r}') = 0 \quad (1.11)$$

- The reduction of the density at the location of the electron \mathbf{r} accounts for the Pauli principle: i.e. it reduces the density to zero:

$$\lim_{|\mathbf{r}-\mathbf{r}'| \rightarrow 0} n_{xc}(\mathbf{r}, \mathbf{r}') = -n(\mathbf{r}) \quad (1.12)$$

- The integral of the exchange-correlation charge over the system yield exactly one positive charge (thus exchange-correlation hole):

$$\int n_{xc}(\mathbf{r}, \mathbf{r}') d\mathbf{r}' = -1 \quad (1.13)$$

V_{KS} is obtained via a variational principle (H-K theorem):

$$\frac{\delta E_{tot}[n]}{\delta n(\mathbf{r})} = \frac{\delta T_s[n]}{\delta n(\mathbf{r})} + V_{ext}(\mathbf{r}) + V_H(\mathbf{r}) + V_{xc} - \mu = 0 \quad (1.14)$$

under the constraint (Lagrange multiplier μ):

$$\int n(\mathbf{r}) \, d\mathbf{r} = N \quad (1.15)$$

and where V_{xc} is simply the partial derivative of E_{xc} with respect of $n(\mathbf{r})$:

$$V_{xc} = \frac{\delta E_{xc}[n]}{\delta n(\mathbf{r})} \quad (1.16)$$

Now, using the K-S orbitals, under the orthonormality condition $\langle \phi_i | \phi_j \rangle = \delta_{ij}$ as variational parameters for the equation 1.14, this assumes the form of the Schrödinger equation 1.5, where the eigenvalues ε_j represent the Lagrange multipliers and the K-S potential $V_{KS}[n](\mathbf{r})$ is expressed as:

$$V_{KS} = V_{ext} + V_H + V_{xc} \quad (1.17)$$

Thus, the knowledge of the exchange-correlation potential (Eq. 1.16) together with Kohn-Sham equations 1.5 and 1.6 allows to transform the problem of N interacting particles in a potential V_{ext} (eq. 1.1), in a problem of N non-interacting particles via inclusion of the interactions through an effective potential V_{KS} . The eigenvalues of the K-S Schrödinger equation, which strictly cannot be interpreted as excitation energies as e.g. also not in Hartree Fock theory by Koopmans' theorem, are in many cases in reasonable agreement with experimental findings.

The practical problem in applying DFT is the exchange-correlation energy and potential. Thus far, no exact expression has been found as the term $E_{xc}[n]$ contains all many-body interactions. However, the correct functional dependence is very complicated, and hence has to be approximated. Two generations of approximations for $E_{xc}[n]$ have been used in the present work:

1. Local Density Approximation (LDA):

$$E_{xc}^{LDA}[n] = \int d\mathbf{r} \, \epsilon_{xc}^{hom}(\mathbf{r}) n(\mathbf{r}) \quad (1.18)$$

with $\epsilon_{xc}^{hom}(\mathbf{r})$ the exchange-correlation energy per particle of a *homogeneous* electrons gas having the same local density $n(\mathbf{r})$ as the inhomogeneous system at point \mathbf{r} . For an homogeneous gas ϵ_{xc}^{hom} has two contributions:

$$\epsilon_{xc}^{hom}(\bar{n}) = \epsilon_x(\bar{n}) + \epsilon_c(\bar{n}) \quad (1.19)$$

and for $\epsilon_x(\bar{n})$ the exact Hartree-Fock result can be used:

$$\epsilon_{xc}^{hom}(\bar{n}) = -\frac{3}{2} \left[\frac{3\bar{n}}{8\pi} \right]^{\frac{1}{3}} + \epsilon_c(\bar{n}) \quad (1.20)$$

The correlation term $\epsilon_c(\bar{n})$ can be calculated by parametrizations[9] of numerical simulations of the homogeneous gas (e.g. Quantum Monte Carlo) []. The two most widespread forms for the energy per particle are those suggested by Hedin and Lundqvist (1971) and by Perdew and Zunger (1981) [10] (PZ-LDA).

For spin polarised electron densities, the local spin density approximation (LSDA) for the exchange-correlation term must be additionally introduced:

$$E_{xc}^{LSDA}[n] = \int d\mathbf{r} \epsilon_{xc}^{hom}(\bar{n}_\uparrow, \bar{n}_\downarrow) \Big|_{(n_\uparrow(\mathbf{r}), n_\downarrow(\mathbf{r}))} n(\mathbf{r}) \quad (1.21)$$

The efficiency of LDA and LSDA is limited in two aspects:

- higher derivatives of the density are not considered
- self-interaction error:

i.e. the self-Coulomb energy contained in $\frac{1}{2} \iint \frac{n(\mathbf{r})n(\mathbf{r}')}{|\mathbf{r}-\mathbf{r}'|} d\mathbf{r}d\mathbf{r}'$ is not cancelled exactly by $E_{xc}^{LDA}[n]$. As a consequence:

$$\lim_{\mathbf{r} \rightarrow \infty} V_{xc}^{LDA} \sim -e^{-a\mathbf{r}}, \quad \text{for finite systems} \quad (1.22)$$

while:

$$\lim_{\mathbf{r} \rightarrow \infty} V_{xc}^{exact} \sim -\frac{1}{\mathbf{r}} \quad (1.23)$$

2. Generalised Gradient Approximation (GGA):

Particularly striking errors arise from LDA calculations when the electron density is strongly inhomogeneous, like for free atoms, molecules or surfaces, or for localised states. This leads to the so called overbinding effect, resulting in too short bonds and too large binding energies. In these cases, non-local corrections to the exchange-correlation functional E_{xc} are necessary. A first step towards non-locality is a gradient expansion of E_{xc} :

$$E_{xc}^{GGA}[n] = \int d\mathbf{r} g_{xc}(n(\mathbf{r}), \nabla n(\mathbf{r}), \dots)n(\mathbf{r}) \quad (1.24)$$

The gradient approximation proposed by Perdew and Wang (1991) [11] (PW91-GGA) is the most often used approximation throughout this thesis.

1.2 Vienna *Ab initio* Simulation Package

The method used to perform the simulations in this thesis is the Vienna *Ab initio* Simulation Package (VASP) [12], mainly developed by G. Kresse and J. Furthmüller [13]. VASP is a package for performing ab-initio quantum-mechanical molecular dynamics which uses pseudopotentials and a plane wave basis set. In the following the concept of pseudopotential will be briefly summarised

Pseudopotentials

Most numerical methods for solving the Schrödinger equation imply the decomposition of the wavefunctions in a set of basis functions. In principle any complete set of basis functions can be used, as e.g. atomic and *muffin-tin* orbitals or plane waves. Plane waves are a very attractive basis set because, by using them, the problem can be cast in a very simple form:

- Plane wave basis function are independent of the location of the atoms

- Basis set convergence is easily checked by increasing the highest kinetic energy plane wave contained in the basis set
- To pass from a real-space to a reciprocal-space representation requires only a fast Fourier transform of the wave functions or potentials
- The valence electronic structure of quite a few solids is not too different from that of jellium

However, if all the electrons are included, plane waves do not work at all:

- The potential near the atom has a Coulomb singularity. This will result in wave functions having cusps. These cusps can not be easily expanded in plane waves
- The lowest eigenvalues will converge to core states, which can be highly localised in contrast to valence states. The plane waves will need to span widely different length scales (large cut-off)
- Orthogonality conditions will require that valence states will have numerous nodes, again requiring a huge number of plane waves

The tightly bound core states contain little chemical information, i.e. the chemical properties depend almost exclusively on the valence electrons. For this reason one can construct a potential, which preserves the chemical information of a solid but does not explicitly include the core states. The basic idea is to modify the plane wave basis functions in such a way that they are automatically orthogonal to the core orbitals (this is the so called Orthogonalised plane waves approach (OPW)). The OPW method reflect the following properties:

- Near the nucleus, the wave function looks like atomic-like functions

- In the bonding region between atoms, the wave function looks like a plane wave
- The valence wave functions are orthogonal to the core states

Within the OPW approach, the pseudopotential can thus be written in the following form (Phillips-Kleinman Cancellation Theorem):

$$V_{pseudo} = V_{all-electron} + V_R \quad (1.25)$$

with V_R cancelling the all-electron potential inside the cut-off radius (r_c).

The essential property of the (non-local) pseudopotential is that in the function space orthogonal to the core states (i.e. the valence states), its eigenvalues spectrum is identical to that of the all-electrons potential. This is a rather weak requirement and without any further restrictive conditions, whole families of pseudopotentials may be constructed all satisfying this requirement. When constructing a pseudopotential, three important aspects must be considered:

- It should be as soft as possible in order to allow the expansion of the valence wave function using a basis set as small as possible
- It should be as transferable as possible: the pseudopotential is constructed for a reference configuration, usually the free atom. It is applied to a molecular or solid-state calculation where the atom is eventually in an ionic configuration. Transferability essentially requires that the equality (or near-equality) of pseudo- and all-electron logarithmic derivatives extends over as large an energy interval as possible
- The pseudo-charge density should reproduce the valence charge density as accurately as possible

Ultrasoft Pseudopotentials and Projector Augmented-Wave Potentials

In this respect one can distinguish between norm-conserving (Hamann, Schlüter and Chiang [14, 15]) and ultrasoft pseudopotentials (Vanderbilt [16]). Both types of pseudopotentials are based on the concept of replacing the wave functions with nodeless pseudo-wavefunctions. In addition, norm conservation requires the norm of the pseudo-wavefunctions and the exact all-electron wavefunctions to be identical within the cut-off radius. It is now well established that within the norm-conserving pseudopotential concept, good transferability requires a cut-off radius (r_c) around the outermost maximum of the all-electron wave function. Therefore for elements with strongly localised orbitals (i.e. $3d$ elements) the resulting pseudopotentials require a large plane-wave basis set. To overcome this limitation one usually increases the cut-off radius, but this is not in general a good solution because the transferability is always adversely affected when r_c is increased.

To solve this problem, Vanderbilt proposed a radically new concept based on relaxing the norm-conserving constraint: as with norm-conserving pseudopotentials the all-electron and pseudo wave functions are required to be equal outside r_c , but inside r_c they are allowed to be as soft as possible. As a consequence, the pseudo wave functions are not normalised inside r_c , resulting in a charge deficit. This problem is solved by introducing localised atom-centered augmentation charges (i.e. the pseudo-charge density is not obtained by computing $\sum |\phi|^2$). The success of the method (widely adopted, especially for $3d$ metals) is obstructed by the rather difficult construction of the pseudopotentials due to the fact that too many parameters must be chosen.

Some of these disadvantages are avoided in the Projector Augmented-Wave Potentials (PAW) method, based on a linear transformation of the pseudo wave

function ($\tilde{\psi}$) to the all-electron wave function (ψ):

$$|\psi_n\rangle = |\tilde{\psi}_n\rangle + \sum_i |\phi_i\rangle \langle \tilde{p}_i | \tilde{\psi}_n\rangle - \sum_i |\tilde{\phi}_i\rangle \langle \tilde{p}_i | \tilde{\psi}_n\rangle \quad (1.26)$$

with $\tilde{\psi}_n$ variational quantities. The index i refers to a sum over the atomic site, the angular momentum and reference energies. ϕ and $\tilde{\phi}$ are the all-electron and pseudo partial waves that match at the core radius. Finally p_i are the projector functions that have to be created in a way to be dual to the partial waves:

$$\langle \tilde{p}_i | \tilde{\psi}_j\rangle = \delta_{ij} \quad (1.27)$$

Thus, the PAW method, implemented in VASP, works directly with the all-electron valence wave function and all-electron valence potentials. Its accuracy approaches the computationally more demanding all-electrons methods.

In closing, forces and stress can be easily calculated with VASP and used to relax atoms into their instantaneous ground state. In the present calculations the geometry was optimised until all forces were smaller than 0.01 eV/Å.

1.3 Scanning tunnelling Microscopy

Scanning tunnelling microscopy (STM) is a technique developed in the Eighties [17, 18] that allows direct, real space determination of surface structures. On conducting samples it allows imaging of features ranging from atomic dimensions up to the micrometer range [19]. The operation of scanning tunnelling microscopy is based on the so-called tunnelling current, which flows, by applying a small bias voltage (~ 1 mV), when a sharp tip is brought in close vicinity (5-10 Å) to a metal or semiconductor surface. The tunnelling current depends exponentially on the tip-sample distance. The strong dependence of the tunnelling current on the tip-sample distance implies

that virtually the whole tunnelling current flows through the single atom or a group of atoms located at the apex of the tip. Hence, atomic resolution can be in principle achieved.

As a first approximation, an image of the tunnelling current maps the topography of the sample. More accurately, the tunnelling current corresponds to the local electronic density of states at the surface. For small bias voltage, STMs actually sense the number of filled or unfilled electron states near the Fermi surface, within an energy range determined by the bias voltage. Rather than measuring physical topography, it measures the tunnelling probability on the surface. This fact can on one side constitute an experimental limit to the determination of the geometrical characteristics of a surface, on the other hand, it can allow to distinguish atomic species with different electronic properties at approximately the same height on a surface.

Due to its importance in the research of surface phenomena, the STM soon has attracted considerable theoretical efforts to calculate the tunnelling current and to simulate STM topographical images from simplified models of the STM system [19, 20]. Throughout this thesis the Tersoff-Hamann approach [21, 22] to simulate STM images is used, which will be briefly summarise in the following.

The Tersoff-Hamann approach

While it is easy to write down a formal expression for the tunnelling current, many approximations are needed to derive an expression useful for practical computation. The tunnelling current is given to first order in Bardeen's [23] formalism by summing over the relevant states:

$$I = \frac{2\pi e}{\hbar} \sum_{\mu, \nu} f(E_\mu) [1 - f(E_\nu + eV)] |M_{\mu\nu}|^2 \delta(E_\mu - E_\nu) \quad (1.28)$$

where $f(E)$ is the Fermi function, V is the applied voltage, $M_{\mu\nu}$ is the tunnelling matrix element between states ψ_μ of the probe and ψ_ν of the surface (i.e. the amplitude of electron transfer):

$$M_{\mu\nu} = \langle \psi_\nu | U | \psi_\mu \rangle \Rightarrow \begin{cases} H\psi_\mu = \varepsilon_\mu \psi_\mu \\ (H + U)\psi_\nu = \varepsilon_\nu \psi_\nu \quad U = \text{perturbation} \end{cases} . \quad (1.29)$$

and E_μ is the energy of state ψ_μ in the absence of tunnelling. Taking the limits of small voltage and temperature [24]:

$$I = \frac{2\pi e^2 V}{\hbar} \sum_{\mu, \nu} |M_{\mu\nu}|^2 \delta(E_\nu - E_F) \delta(E_\mu - E_F) \quad (1.30)$$

Bardeen [23] has shown that:

$$M_{\mu\nu} = \frac{\hbar^2}{2m} \int_S d\mathbf{S} (\psi_\mu^* \nabla \psi_\nu - \psi_\nu \nabla \psi_\mu) \quad (1.31)$$

where the integral is over any surface laying entirely within the vacuum region separating tip and sample. In order to evaluate $M_{\mu\nu}$ it is useful to expand the surface wave function in the general form

$$\psi_\nu = \Omega_s^{-\frac{1}{2}} \sum_{\mathbf{k}_n} a_{\mathbf{k}_n} e^{-\sqrt{\kappa^2 + |\mathbf{k}_n^\parallel|^2} z} e^{i\mathbf{k}_n^\parallel \mathbf{r}} . \quad (1.32)$$

Here Ω_s is the sample volume, $\kappa = \hbar^{-1} \sqrt{2m\phi}$ is the minimum inverse decay length for the wave functions in vacuum, ϕ the work function and $\mathbf{k}_n^\parallel = \mathbf{k}^\parallel + \mathbf{G}_n^\parallel$, where \mathbf{k}^\parallel is the surface Bloch wave vector and \mathbf{G}_n^\parallel is the surface reciprocal lattice vector. In the Tersoff-Hamann approximation, the tip is modelled as a locally spherical potential well, as illustrated in Fig.1.1. Thus, the local tip wave functions have the asymptotic spherical form:

$$\psi_\mu = \Omega_t^{-\frac{1}{2}} c_t \kappa R e^{\kappa R} (\kappa |\mathbf{r} - \mathbf{r}_0|)^{-1} e^{-\kappa |\mathbf{r} - \mathbf{r}_0|} \quad (1.33)$$

where Ω_t is the probe volume. Expanding the tip wave function 1.33 in the same form as the surface 1.32 and substituting the two expressions in 1.31 one finds:

$$M_{\mu\nu} = -\frac{\hbar^2}{2m} \frac{4\pi}{\kappa \sqrt{\Omega_t}} \kappa R e^{\kappa R} \psi_n u(\mathbf{r}_o) \quad (1.34)$$

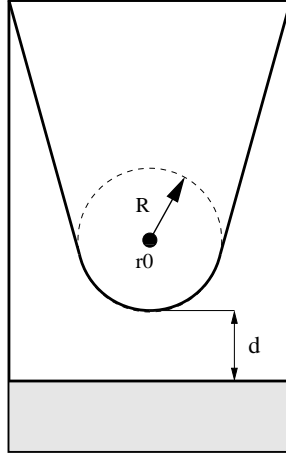


Figure 1.1: Schematic picture of tunnelling geometry. The probe tip has an arbitrary shape but is assumed locally spherical with radius of curvature R , where it comes close to the surface (grey area) at a distance d . The centre of curvature of the tip is \mathbf{r}_0

Plugging this expression in 1.28 one obtains the desired result:

$$I = \frac{32\pi^3 2^2}{\hbar} V \phi^2 D_t(E_F) R^2 \kappa^{-4} e^{2\kappa R} \sum_{\nu} |\psi_{\nu}(\mathbf{r}_o)|^2 \delta(E_{\nu} - E_F) \quad (1.35)$$

where $D_t(E_F)$ is the density of states per unit volume of the probe tip. We note that $\sum_{\nu} |\psi_{\nu}(\mathbf{r}_o)|^2 \delta(E_{\nu} - E_F)$ is nothing but the surface local density of states (LDOS) at E_F at the point \mathbf{r}_o ($\rho(\mathbf{r}, E_F)$), or, equivalently, the number of electrons per unit volume per unit energy. According to 1.35, at constant current regime, the tip follows a contour of constant $\rho(\mathbf{r}, E_F)$. Due to its simplicity and its generality this approach has gained a reputation as the *workhorse* (Lucas [25]) of STM theory and is surprisingly successful in describing subtle effects.

1.4 Low Energy Electron Diffraction

Low Energy Electron Diffraction (LEED) is the standard technique to determine not only the periodicity of a surface but also its atomic geometry and chemical composition. The fundamentals of this method are described in every surface science book (e.g. [26, 27]).

The application of quantitative I vs. V LEED as a method to determine the structure of a surface is discussed in detail in [28], where this technique is used assisted by a numerical algorithm to determine the (3×1) and $c(2 \times 2)$ structures of Br on Pt(110) with an unprecedented precision. Experiments performed with another LEED-based method are cited in the present work, namely the analysis of the spot profiles as a function of temperature (I vs. T LEED in the following). This technique is based on the fact that near a critical temperature the structure factor can be decomposed into three components [29]:

$$S(q_{\parallel}, t) = \underbrace{I_0(t)\delta(q - q_0)_{\parallel}}_{(i)} + \underbrace{\frac{\chi_0(t)}{1 + (q - q_0)_{\parallel}^2 \xi^2(t)}}_{(ii)} + \text{background} \quad (1.36)$$

where the first term describes the contribution from long range order. For a continuous phase transitions and for $T < T_c$, I_0 is proportional to $|t|^{2\beta}$, while for $T > T_c$, $I_0 = 0$. As usual, q_0 is a reciprocal lattice vector and $t = \frac{T - T_c}{T_c}$. The second term describes the contribution of short range fluctuations of the order parameter: χ_0 denotes the electronic susceptibility and ξ the correlation length. For a second order phase transition they behave like $\chi_0 \propto |t|^{-\gamma}$ and $\xi \propto |t|^{-\nu}$.

The delta function in (i) is actually broadened into a Gaussian function in any real measurement and its height describes the temperature dependence of the long range order. The term in (ii) is a Lorentzian function characterising the fluctuations

of the system. By fitting the experimental LEED spots by means of a function like:

$$\frac{f}{d}e^{-\frac{(x-a)^2}{2d^2}} + \frac{c}{b^2 + (x-a)^2} + \text{background} \quad (1.37)$$

information about the nature of the phase transition can thus be deduced.

1.5 Computational Details

First-principles density-functional theory calculations have been performed with the projector augmented wave Vienna ab-initio simulation package (PAW-VASP) [13, 12]. Where not otherwise specified, exchange-correlation was treated within the generalised gradient approximation (GGA) [11], yielding a Pt bulk lattice constant of 3.986 Å. Repeated slabs of 9 Pt layers with an ad-layer on one side and a p(1×1) Pt termination on the other side were separated by a 10 Å thick vacuum layer. The adsorption on the missing row reconstructed surface A missing-row reconstructed surface is simulated with 8 full and one half Pt layers. All layers were relaxed except three layers on the far side of the Pt substrate frozen to the relaxed geometry of a p(1×1)-Pt(110) surface. The reference energies of the clean surfaces can be found in section 2.1. An energy cut-off of 400 eV was considered sufficiently accurate for the present purposes. A Monkhorst-Pack type k -point mesh was used, the dimensions of which depend on the periodicity of the modelled cell. The values of the adsorption energies are given with respect to the binding energy in the isolated X₂ (where X is a halogen atom, Br, Cl or I) and CO (NO) molecules. The calculated binding energies are

- $E_{Cl_2} = 3.490$ eV
- $E_{Br_2} = 2.959$ eV
- $E_{I_2} = 2.629$ eV

- $E_{CO} = 14.817 \text{ eV}$
- $E_{NO} = 12.270 \text{ eV}$

Chapter 2

Halogen adsorption on Pt(110), low coverages

The adsorbate system Br/Pt(110) exhibits a rich and very interesting phase diagram [30]. A phase transition occurring close to half monolayer coverage (here the monolayer is defined by the atom density of the bulk-terminated Pt(110) surface) from a $c(2\times 2)$ to a (3×1) structure has been argued to be linked with the formation of a charge density wave (CDW) [31]. The $c(2\times 2)$ parent phase of the CDW was investigated more closely by spot-profile analysis LEED (low energy electron diffraction) and variable-temperature STM. The surprising result was the presence of one-dimensional fluctuations in the long-range ordered $c(2\times 2)$ phase over a wide range of temperatures from the disordering temperature (375 K) down to 250 K. Below 250 K a (2×1) structure appears locally and at 50 K a third structure coexists with the previous ones, resulting in a disordered, striped pattern of $c(2\times 2)$, (2×1) and (3×2) domains [32].

Disordering upon cooling seems a counter-intuitive phenomenon, but it is found to be generic for systems with competing order parameters close to a quantum phase transition [33, 34]. Notable examples are the high-temperature superconductors (HTSCs), where magnetic order and, depending on the doping level, charge order

compete with superconductivity. This competition results in the loss of long-range order and a phase separation [28]. Br/Pt(110) is a surface system, where the competition of (at least) two order parameters leads to a strikingly similar behaviour. Lowering the temperature yields a transition from a long-range ordered phase into a strongly fluctuating and finally into an inhomogeneous state. As these transitions occur in a surface system they can be investigated also experimentally by surface sensitive methods and in particular by direct imaging in scanning tunnelling microscopy (STM).

2.1 The Clean Pt(110) Surface

Adsorbate systems on (110) face of Pt are the object of the present work. The clean surface is known to be characterised by the so called “missing row” (MR) reconstruction, i. e. a doubling of the periodicity along the [001] direction with respect to the bulk due to the absence of every second close-packed row in the first surface layer. This reconstruction can be attributed to the interplay between the surface stress and surface free energy [35]. A sketch of both, the ideal unreconstructed and the MR-reconstructed Pt(110) surface is given in figure 2.1

Both surfaces are characterised by a contraction in the first interlayer spacing. The MR-reconstructed surface, shows a larger contraction of the first interlayer spacing with respect to the unreconstructed one, and also a slight row-pairing (displacement of the Pt atoms from their ideal positions parallel to the surface) in the even and a significant buckling (displacement of the Pt atoms relative to one another normal to the surface) in the odd layers except the first one. These relaxations are caused by the tendency to smooth the large corrugation of the MR surface.

The fcc Pt lattice constant was obtained from bulk calculations. Its value, 3.986 Å, overestimates slightly the experimental lattice constant of 3.92 Å. In fig-

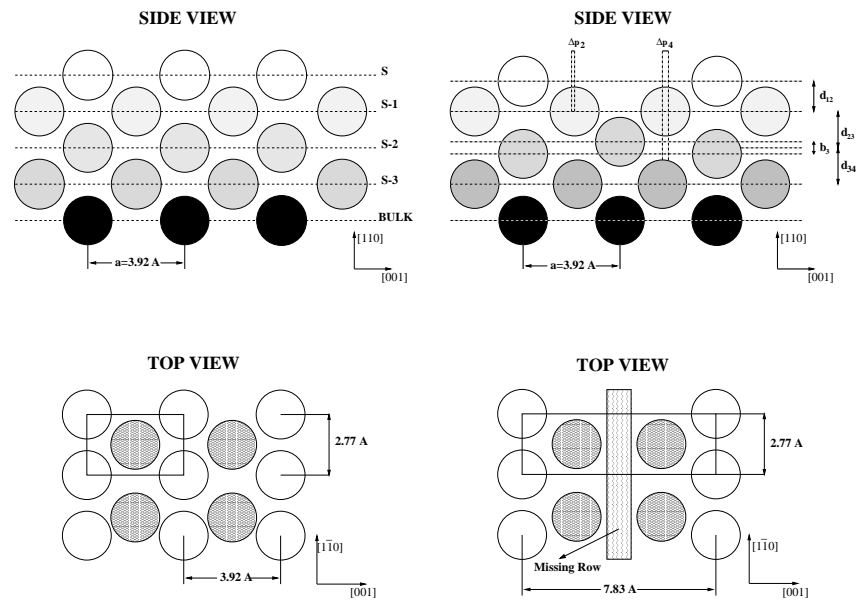


Figure 2.1: Representation of the ideal Pt(110) surface unit cell (left) and of the Pt(110)-(1 \times 2) missing-row reconstructed surface unit cell (right), side view (top) and top view (bottom). Geometrical parameters of the missing-row model with multi-layer relaxations are indicated. In the top-views grey circles represent sub-surface atoms. Experimental lattice constant indicated [36].

ure 2.2 the relaxation parameters of the unreconstructed surface are shown, simulated with slabs of different thickness. Typical properties of the surface can be observed, like the strong compression of the first interlayer spacing, partially compensated by the dilatation of the second one. The deformations are confined to the first few Pt monolayers and not very dependent on the thickness of the slab.

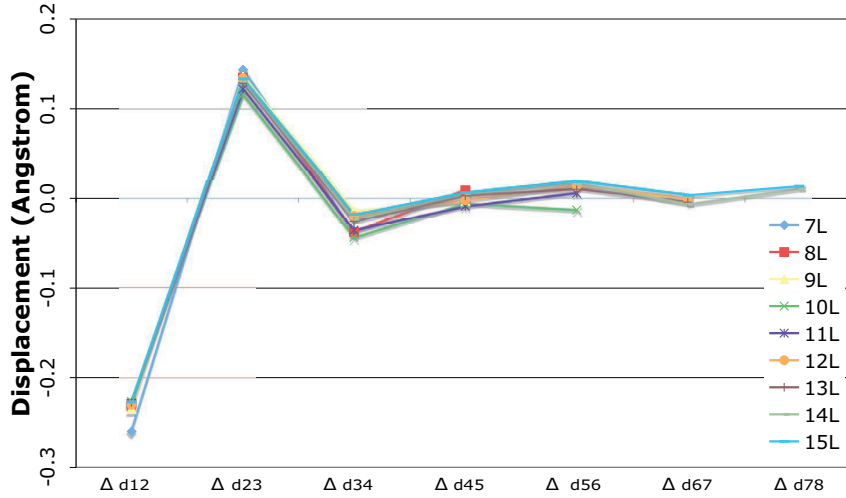


Figure 2.2: Relaxation parameters of the unreconstructed Pt surface. Typical properties can be observed, like the strong compression of the first interlayer spacing, partially compensated by the dilatation of the second one. The deformations are confined to the first few Pt monolayers and not very dependent on the thickness of the slab

In table 2.1 the calculated changes in interlayer spacings of the metastable unreconstructed Pt(110)-(1×1) surface are compared with the results of precedent simulations. Since the clean unreconstructed surface is not stable, no experimental results are available. All results are qualitatively in good agreement. The agreement with the most recent simulations (flair) is also quantitative.

Figures 2.3 to 2.5 show respectively the pairings, the bucklings and the variations of the first interlayer spacings for the MR surface.

In table 2.2 a compilation of experimental and theoretical results for the 1×2

Method	Δd_{12}	Δd_{23}	Δd_{34}	Δd_{45}	Δd_{56}	d
present-9L	-0.23	0.13	-0.04	-0.01	—	1.409
present-15L	-0.23	0.13	-0.02	-0.01	-0.02	1.409
flair-LDA-9L[36]	-0.21	0.13	-0.04	—	—	1.378
flair-GGA-9L[36]	-0.21	0.13	-0.05	—	—	1.407
LCAO[37]	-0.16	0.07	-0.02	—	—	1.377
Tight Binding[38]	-0.06	0.01	0.00	—	—	1.415
Emb. Atom[39]	-0.24	0.04	—	—	—	1.385

Table 2.1: Comparison of calculated changes in interlayer spacings of the metastable unreconstructed Pt(110)-(1×1) surface. $\Delta d_{i,i+1}$ denote the changes in the interlayer spacing with respect to the ideal bulk interlayer spacing d in Å. (L: number of layers considered)

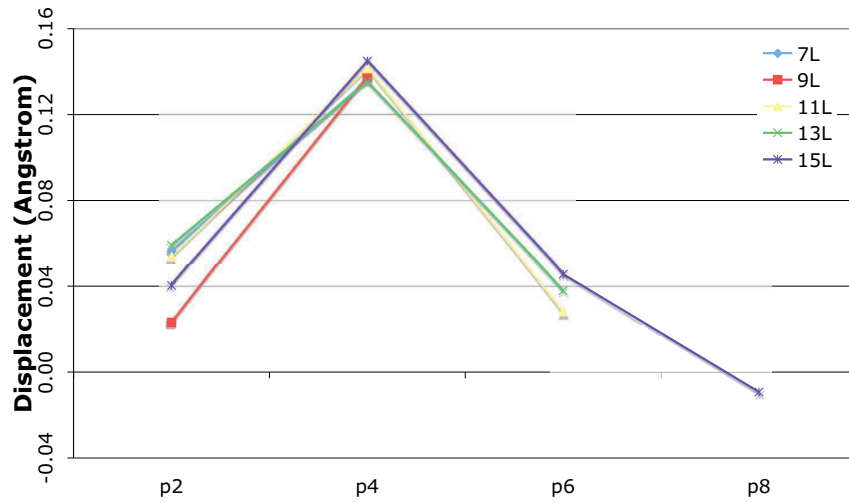


Figure 2.3: Pairings of the MR-Pt-(1×2) surface calculated with slabs of different thickness. The pairing is defined here as the *relative* displacement of Pt atoms, and is therefore the double of the displacement of the single atom.

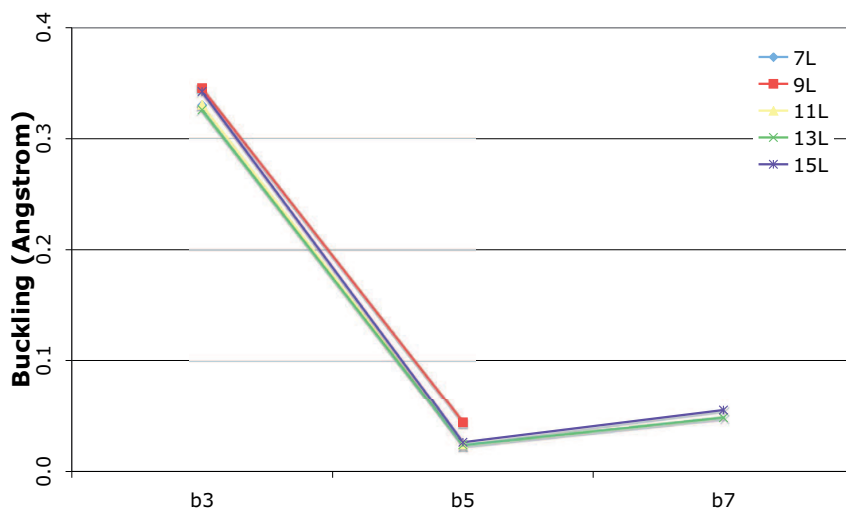


Figure 2.4: Bucklings of the MR-Pt-(1×2) surface

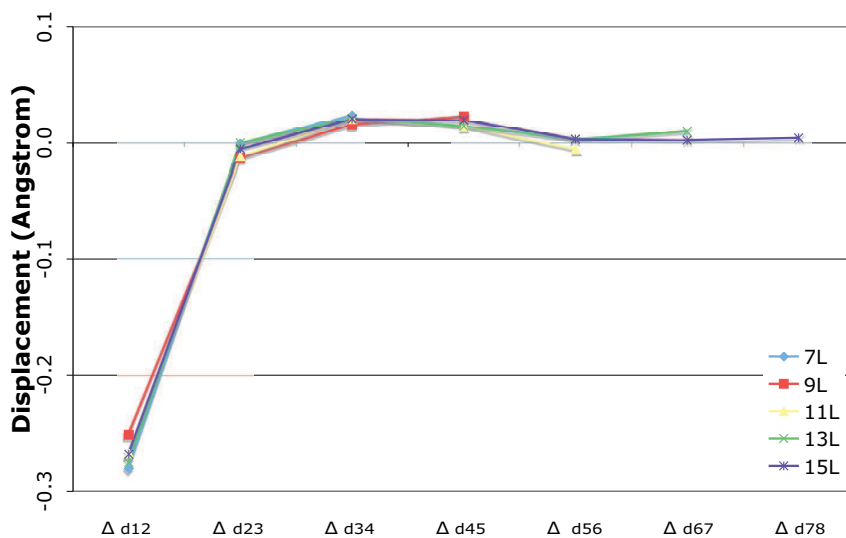


Figure 2.5: Relaxation parameters of the Mr-reconstructed Pt-(2×1) surface. The compression of the first interlayer spacing is even stronger than in the unreconstructed surface. Also in this case, the deformations are confined to the first few Pt monolayers and not very dependent on the thickness of the slab.

missing-row structure of clean Pt(110) is given. The interlayer spacings are accurately predicted, while the pairings (particularly the pairing in the second Pt layer) are underestimated.

Method	Δd_{12}	Δd_{23}	Δd_{34}	Δd_{45}	Δd_{56}	b_3	b_5	p_2	p_4	p_6	d
present-9L	-0.24	-0.01	0.02	0.02	-0.01	0.35	0.04	0.02	0.14	—	1.409
present-15L	-0.27	-0.01	0.02	0.02	0.00	0.34	0.03	0.04	0.14	0.05	1.409
flair-GGA-9L[36]	-0.23	0.00	0.03	0.03	—	0.37	—	0.00	0.19	—	1.407
flair-LDA-9L[36]	-0.22	0.00	0.03	0.03	—	0.34	—	0.01	0.16	—	1.378
LEED[40]	-0.24	-0.01	0.02	0.02	-0.01	0.26	0.03	0.07	0.13	—	1.385
LEED[41]	-0.28	-0.01	0.02	0.01	0.01	0.17	0.03	0.08	0.10	—	1.385
LEED[42]	-0.26	-0.18	-0.12	-0.01	—	0.32	—	0.13	0.24	—	1.385
MEIS[43]	-0.22	0.06	—	—	—	0.10	—	—	—	—	1.385
XRD[44]	-0.27	-0.11	—	—	—	—	—	0.10	0.08	—	1.385
RHEED[45]	-0.37	0.07	—	—	—	0.18	—	0.08	—	—	1.385
RHEED[46]	-0.34	-0.01	—	—	—	0.12	—	0.09	—	—	1.385

Table 2.2: Compilation of experimental and theoretical results for the 1×2 missing-row structure of clean Pt(110). $\Delta d_{i,i+1}$ denotes the changes in the (average) inter-layer spacing with respect to the ideal bulk inter-layer spacing d , while p_i and b_i denote the lateral pairing and buckling in layer i , respectively (all values in Å). Error bars for the parameters derived by the LEED analysis of Ref. [40] are ± 0.02 Å for $\Delta d_{i,i+1}$, ± 0.05 Å for b_i and ± 0.07 Å for p_i . (L: number of layers considered in calculations.)

An important convergence test requires the binding energy per atom to be independent of the periodicity of the repeated cell. A 9-layers thick slab was simulated with different unit cells (see Tab. 2.3), the maximum change in the energy per atom due to the change of symmetry is 3 meV.

	(1×1)	(3×1)	(4×1)	(2×2)	(3×2)	(4×2)	(6×2)	(7×2)
E_{ads}	51.82	155.47	207.40	207.30	310.94	414.79	621.89	725.76
N_{atoms}	9	27	36	36	54	72	108	126
E_{ads}/N_{atoms}	5.758	5.758	5.761	5.758	5.758	5.761	5.758	5.760

Table 2.3: Total binding energy and energy per atom of a 9-layer slab calculated with different cells.

2.2 Halogens on the unreconstructed Pt(110) surface

Halogens adsorbed on the strongly anisotropic Pt(110) surface form a sequence of different structures depending on the coverage and on the temperature. In the present section general trends of the halogen adsorption at coverages up to $1/2$ ML are investigated, with particular attention paid to the complex Br phase diagram.

2.2.1 $1/4$ ML Coverage: The Single Halogen Approximation

The MR reconstruction is lifted by Halogens adsorption above the coverage of $\sim 1/4$ ML, The substrate for further adsorption is therefore the unreconstructed (1×1) surface. The Pt- (1×1) surface presents 4 high symmetry sites: on top of a Pt atom (top, T), in the hollow (H) between 4 atoms of the first Pt layer, and two non equivalent bridge sites: a short bridge (SB) above a pair of atoms of a close-packed Pt row, and a long bridge (LB) site above a pair of Pt atoms residing in two neighbouring rows (s Fig. 2.6).

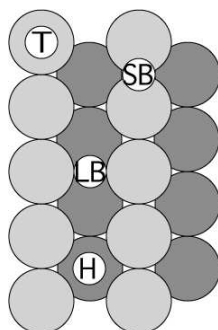


Figure 2.6: High symmetry potential adsorption sites on the unreconstructed (1×1) -Pt(110) surface.

The adsorbate-adsorbate interaction at distances equal or larger than twice the lattice constant is negligible. Therefore, the interaction of a single halogen atom with the Pt surface can be simulated as the adsorption of a single atom on a (2×2) cell,

which corresponds to a coverage of $1/4$ ML. It must be noted that such a simulation, although giving important clues about the geometry and energetics of the bonding at higher coverages, does not correspond to a physically observable phase, since the MR reconstruction is globally lifted for coverages above $1/4$ ML. The halogen adsorption on Pt-MR was thoroughly investigated by Franchini [36].

The results of the simulations are displayed in figure 2.7. Cl and Br show a straightforward similarity: SB is slightly preferred over LB, while T and H sites are much less stable. I, instead, prefers LB over SB and H over T sites, which can be attributed to its larger size.

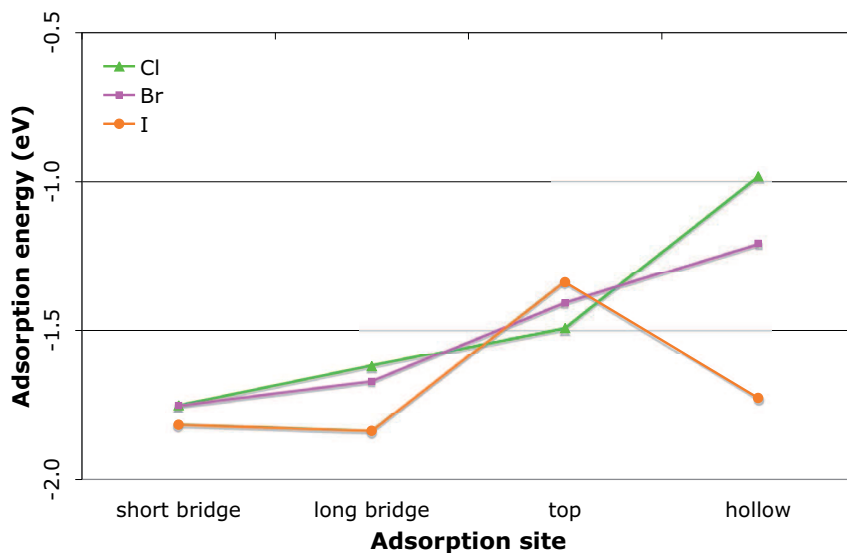


Figure 2.7: Single-adsorbate approximation. Adsorption energies on the (1×1) -Pt(110) surface.

The Role of Relaxation

In the single adsorbate approximation, the substrate is free to relax to the highest degree: No constraint is acted on the six outmost Pt layers and the relaxations caused by neighbouring adatoms interfere to a negligible degree. At higher coverages, the

relaxations caused by neighbouring adatoms do interfere, and in some cases the Pt atoms can just relax in z direction (normal to the surface) due to symmetry reasons.

In table 2.4 the adsorption energies and bondlength relative to both bridge sites on the relaxed metal surface are compared to the corresponding values on a xy -frozen surface, where no pairing is allowed.

Relaxed					
	E_{SB}	L_{SB}	E_{LB}	L_{LB}	$E_{SB} - E_{LB}$
Cl	-1.752	2.385	-1.619	2.422	-0.133
Br	-1.754	2.504	-1.671	2.534	-0.081
I	-1.817	2.603	-1.836	2.632	0.020
xy -frozen					
	E_{SB}	L_{SB}	E_{LB}	L_{LB}	$E_{SB} - E_{LB}$
Cl	-1.701	2.397	-1.402	2.496	-0.300
Br	-1.386	2.509	-1.191	2.582	-0.196
I	-1.465	2.628	-1.411	2.674	-0.054

Table 2.4: Comparison of calculated adsorption energies (E) and bondlength (l) on a fully relaxed vs. xy -frozen surface. Energies are expressed in eV and lengths in Å.

The effect of relaxation is much larger for adsorption on long bridge than on short bridge. If pairing is not allowed also I prefers SB over LB sites.

2.2.2 1/2 ML Coverage, General Trends

As one halogen atom per (2×2) cell corresponds to a coverage of 1/4 ML, a coverage of 1/2 ML is obtained if a second site per cell is occupied. In a (2×2) cell, the occupation of non equivalent adsorption sites is ruled out by geometrical reasons [36]. A (2×2) unit cell has four equivalent sites of each high symmetry type. Once one is filled up, there are three ways to occupy a second one. Just bridge sites (SB, LB) are to be considered, T and H sites are too unfavourable and can be ignored. The six resulting possibilities are shown in figure 2.8.

A comparison between the different adsorption arrangements shows some gen-

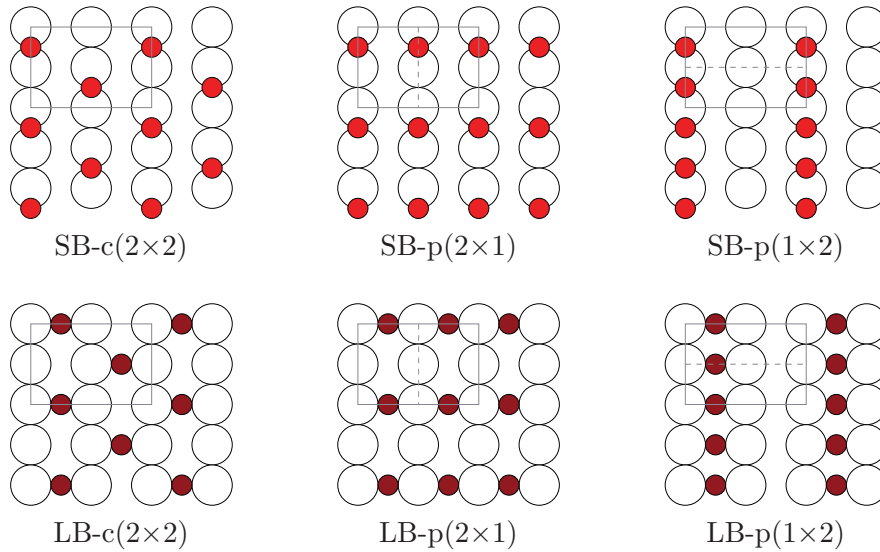


Figure 2.8: Adsorption arrangements with 1/2 ML halogen coverage

eral trends: the SB-p(2×1) arrangement is slightly stabilised with respect to the corresponding c(2×2) phase. This is particularly evident in the case of Cl and causes Cl-p(2×1) to be more stable than Cl-c(2×2). Besides, two repulsions can be recognised, a direct and a substrate-mediated one. The adsorbate-adsorbate direct repulsion depends only on the distance between the adatoms as compared with their covalent radii. It is particularly evident in the $[1\bar{1}0]$ direction where the adatoms are nearer, but it can be observed even in the $[001]$ direction for I and Br. For Br, this leads to an interesting energetic trade-off with the already mentioned p(2×1) stabilisation, which will be analysed in the next section. In addition, a substrate mediated repulsion can be recognised, where adatoms with bonds to the same Pt atom compete for the same substrate orbitals. This second repulsion is quite anisotropic, acting in the direction of the bonding ($[1\bar{1}0]$ for nearest neighbouring adatoms on SB and $[001]$ for adatoms on LB), less dependent on the radius of the adsorbate and in general less strong than the direct repulsion. The substrate mediated re-

pulsion is, at least in part, also due to geometrical effects: If a surface Pt atom is symmetrically bound to 2 halogen adatoms, it can not relax in order to optimise the bondlength (see Tab. 2.5). One can observe that for Br the SB-p(2×1) and the

		SB			LB		
		p(1×2)	p(2×1)	c(2×2)	p(1×2)	p(2×1)	c(2×2)
Cl	E_{abs}	-0.898	-1.740	-1.724	-1.357	-1.400	-1.567
	E_{rel}	0.842	—	0.015	0.210	0.167	—
	L_b	2.447	2.385	2.391	2.421	2.499	2.450
Br	E_{abs}	-0.831	-1.727	-1.725	-1.147	-1.395	-1.560
	E_{rel}	0.896	—	0.002	0.413	0.165	—
	L_b	2.623	2.507	2.509	2.555	2.577	2.546
I	E_{abs}	-0.597	-1.753	-1.785	-0.921	-1.518	-1.722
	E_{rel}	1.189	0.032	—	0.801	0.205	—
	L_b	2.763	2.616	2.617	2.682	2.655	2.652

Table 2.5: Absolute (E_{abs} and relative E_{rel} adsorption energies (in eV) and bondlengths (in Å) of the 1/2 ML arrangements with (2×2) periodicity. Energies are given per adatom referred to the halogen molecule and the clean Pt surface.

SB-c(2×2) adsorbate phases are almost degenerate in energy.

Another phase with 1/2 ML coverage is obtained by occupying two SB and one LB position in a (3×2) unit cell as shown in figure 2.9. In this arrangement, adatoms adsorbed on LB have no first neighbours thus minimising the repulsion. In the case of Br this arrangement is almost as stable as the most favoured (2×2) structures.

2.3 Br/Pt(110): Fluctuations and Phase Separation

As already mentioned, due to the energetic trade-off between stabilisation of the p(2×1) phase and the direct next-neighbour repulsion, three different Br-phases are almost degenerate at 1/2 ML: the c(2×2), the p(2×1) and the (3×2) phases. In apparent contrast to this DFT result at temperatures between 250 K and 375 K, the

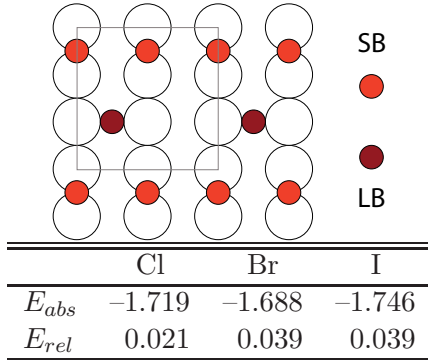


Figure 2.9: Schematic representation of the (3×2) $1/2$ ML halogen phase. In the table the adsorption energies (in eV) per atom referred to the halogen molecules are also given. The relative adsorption energies E_{rel} are referred to the most stable (2×2) arrangement with the same halogen (For Cl and Br to the $p(2 \times 1)$, for I to the $c(2 \times 2)$ phase).

$1/2$ ML Br/Pt(110) surface is experimentally observed in a perfect, global $c(2 \times 2)$ phase, whereas a coexistence of the three degenerate phases would be expected. A deeper understanding of this matter was obtained by the analysis of temperature dependent experiments of the surface structure [47, 48].

2.3.1 Geometry

The Br- $c(2 \times 2)$ phase is already well known both theoretically and experimentally [40, 36, 28]. The calculated geometry for the $c(2 \times 2)$ structure is given in table 2.6 together with the corresponding experimental data and the results of different calculations (see [40]). It is interesting to notice that most of the relaxations take place near the surface in contrast to the clean (MR-reconstructed) surface where relaxations involve atoms down to the fourth layer. Therefore a 9 layers thick slab is suitable for the present calculation. Similar to the clean surfaces calculated results are well within the experimental error limits.

2.3.2 Electronic Properties

In figure 2.10, the p states of Br are compared with the d states of the first Pt layer atoms. The couples Br- p_x , Pt- d_{x^2} and Br- p_z , Pt- d_{xz} show the best overlap and a bonding–antibonding trend, typical of binding states. The states Br- p_y , Pt- d_{yz} , on

	d_0	Δd_{12}	Δd_{23}	Δd_{34}	Δd_{45}
Present	2.075	-0.105	0.025	0.011	0.000
LEED[40]	2.04	-0.10	0.03	0.01	0.00
FLAIR-LDA[36]	2.02	-0.11	0.03	0.01	0.00
FLAIR-GGA[36]	2.07	-0.13	0.02	0.01	0.01
	p_1	p_2	p_3	p_4	d
Present	0.002	0.015	0.004	0.009	1.409
LEED[40]	0.04	0.02	—	—	1.385
FLAIR-LDA[36]	0.01	0.00	0.00	0.00	1.378
FLAIR-GGA[36]	0.01	0.02	0.01	0.00	1.407

Table 2.6: DFT and LEED results for the Br/Pt(110)-c(2×2) phase. d_0 denotes the distance between the Br- and the first substrate layer, $\Delta d_{i,i+1}$ the changes in the interlayer spacing with respect to the ideal bulk spacing d , and p_i the lateral pairing in layer i , all values given in Å. Signs of the lateral pairing parameters p_i are given with respect to the position of the Br atoms. Error limits for the parameters derived by LEED are ± 0.03 Å for d_0 and $\Delta d_{i,i+1}$, ± 0.08 Å for p_1 and ± 0.10 Å for p_2 . In all simulations a 9 layers thick slab was used.

the other hand, are quite uncorrelated.

The c(2×2) and the p(2×1) phases can be obtained from each other by a simple phase slip, without a significant change of the Br–Pt interaction, therefore the binding Br states p_x and p_z are quite unaffected by the phase change.

The bonding is formed by the Br- p_x state, which elongates parallel to the close-packed rows, with the Pt- d_{z2} state (upper left image in figure 2.12) and by the Br- p_z state, pointing inside the surface, with the Pt- d_{xz} state (upper right image in figure 2.12). These couples of states have the best overlap, while the Br- p_y state is less affected by the bonding.

2.3.3 Fluctuations and phase separations: Experimental Evidence

The analysis of LEED spot profiles was adopted as a technique to extract the temperature dependence of the long range order parameter and of the correlation length of fluctuations, as explained in section 1.4. The experimental results are summarised

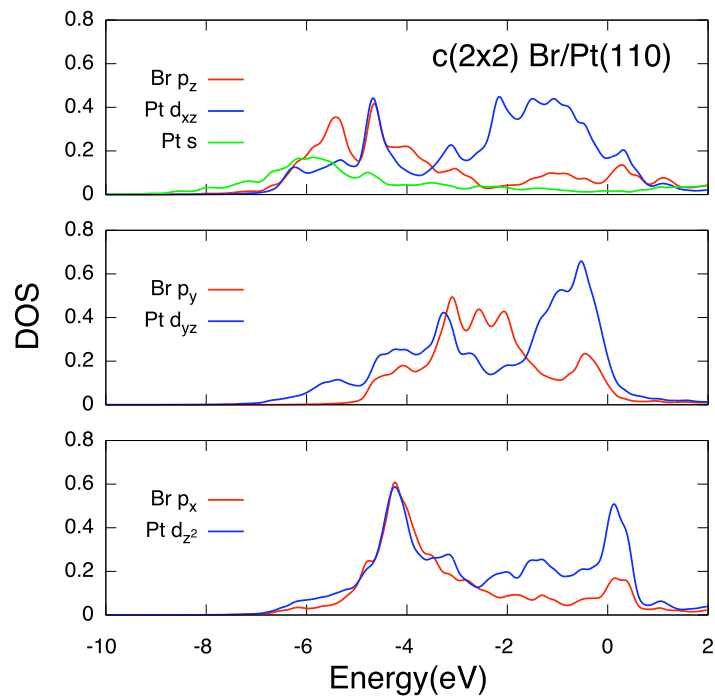


Figure 2.10: Comparison between the p states of Br and the d states of the underlying Pt atoms. The p_z and p_x Br states have a typical bonding–anti bonding correlation with the d_{xz} respectively d_{z^2} Pt states.

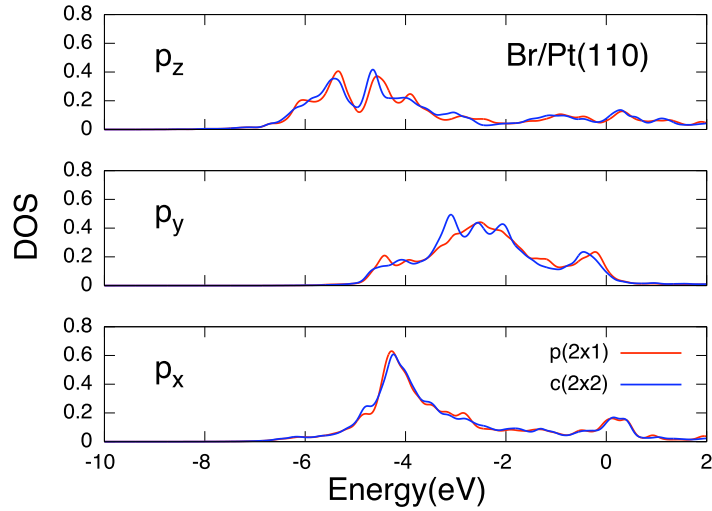
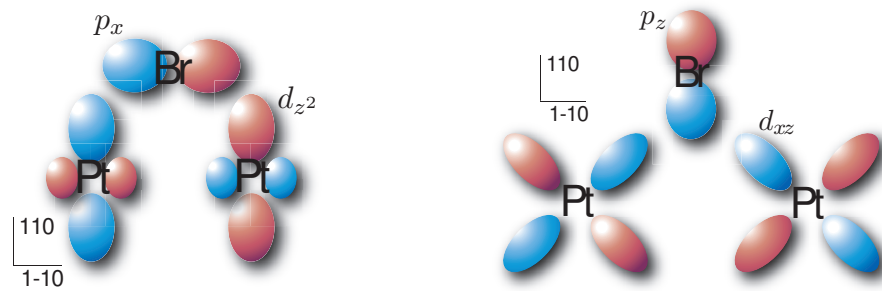


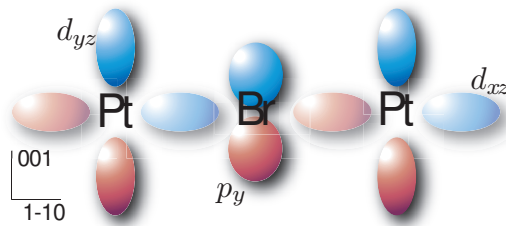
Figure 2.11: Calculated density of states of the p states of Br in the SB- $c(2 \times 2)$ phase (left). A comparison between the states in the $c(2 \times 2)$ and in the $p(2 \times 1)$ phase (right) shows that the states are only slightly affected by a registry shift of adatoms on neighbouring close-packed rows

in figure 2.13. At 375 K the $c(2 \times 2)$ structure exhibits a regular order-disorder transition featuring a sudden drop of the order parameter, the simultaneous appearance of fluctuations with a correlation length of approximately 150 \AA and a drop of both, the fluctuations and the correlation length towards higher temperatures. Below 375 K, LEED as well as STM show a well developed $c(2 \times 2)$ phase, but the spot profile analysis reveals a hidden dynamics: the structure is perfectly long-range ordered perpendicular to the close-packed rows, however it fluctuates along the close-packed rows throughout the temperature range from $375 \text{ K} > T > 250 \text{ K}$ with a correlation length increasing up to $\sim 140 \text{ \AA}$ at $T = 250 \text{ K}$. Notice that the fluctuations do not affect the long range order of the $c(2 \times 2)$ phase in the $[001]$ direction, therefore they must be coherent from row to row.

The order-disorder transition at 375 K takes place in the adlayer only and does not involve the substrate, this can be evinced from the fact that it is reflected only



Lateral view. Br- p_x and Pt- d_{z^2} states. Lateral view. Br- p_z and Pt- d_{xz} states.



Top view. Br- p_y and Pt- d_{yz} states. In lighter colour, the Pt- d_{xz} are also drawn.

Figure 2.12: Reconstruction of the electrical structure of the bonding, showing the best overlapping states.

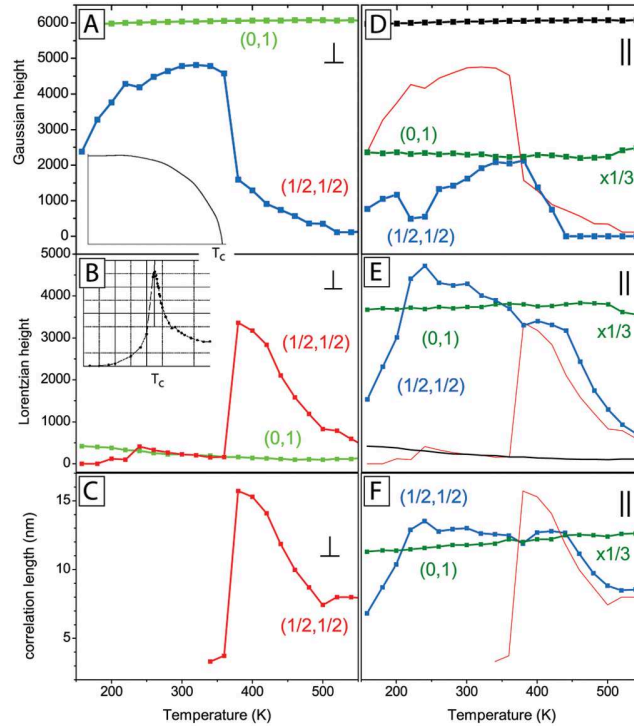


Figure 2.13: LEED spot-profile analysis. (a) Height of the Gaussian component in the peak profile measured perpendicular to the close-packed row direction for the $(1/2, 1/2)$ and the $(0,1)$ spot. Inset: Theoretical power-law dependence of the order parameter in the Ising model, which is isomorphous to the $c(2 \times 2)$ structure. (b) Height of the Lorentzian component in the peak profile measured perpendicular to the close-packed row direction for the $(1/2, 1/2)$ and the $(0,1)$ spot. Inset: Monte Carlo calculation of critical fluctuations in the Ising model. (c) Correlation length of the critical fluctuations in the adsorbate system perpendicular to the close-packed row direction. (d) Height of the Gaussian component in the peak profile measured parallel to the close-packed row direction for the $(1/2, 1/2)$ and the $(0,1)$ spot. For comparison, the behaviour in the orthogonal direction is displayed as the thin red curve. (e) Height of the Lorentzian component in the peak profile measured parallel to the close-packed row direction for the $(1/2, 1/2)$ and the $(0,1)$ spot. (f) Correlation length of the critical fluctuations parallel to the close-packed row direction

in the fractional order LEED spots, while the integer order ones are not affected. In contrast, the fluctuations along the rows appear also in the integer order spots indicating that the substrate is involved in the fluctuations. The observation of a strong substrate buckling in the (3×2) phase is consistent with the assumption that the fluctuations involve the local formation of a threefold periodicity. The assumption of fluctuations into a $3 \times n$ structure yields also a straightforward explanation for the appearance of apparent (3×1) domains as in Fig. 3.1 (see chapter 3). The defects pin the fluctuations locally, making them observable in the time averaged STM image. Surprisingly, below 250 K the propensity to form a structure with threefold periodicity does not increase. Rather, the intensity of all LEED spots drops off rather quickly indicating a loss of long-range order and making the spot-profile analysis unreliable. STM images taken at 110 K show a strongly disturbed $c(2 \times 2)$ structure and the appearance of $p(2 \times 1)$ domains (Fig. 2.14).

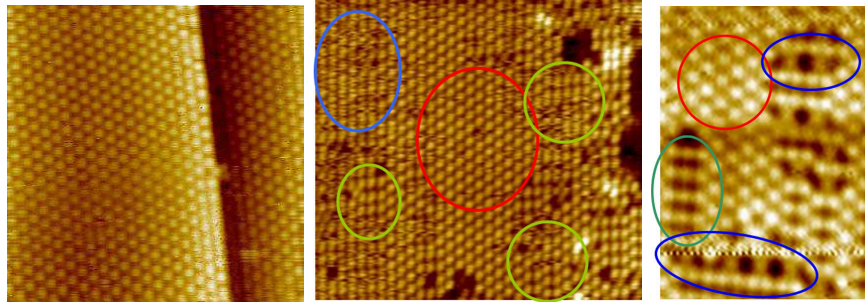


Figure 2.14: STM images of $1/2$ ML Br on Pt upon cooling. Left: global $c(2 \times 2)$ phase at room temperature ($140 \times 140 \text{ \AA}^2$, 0.3 V, 1.2 nA). Centre: $c(2 \times 2)$ -Br/Pt(110) (RT phase) cooled to 110 K. $p(2 \times 1)$ domains (green) are also present at this temperature, besides regions with apparent (1×1) symmetry due to fluctuations (blue) (STM image 0.55 V, 0.88 nA). Right: same phase at 50 K, characterised by the coexistence of $c(2 \times 2)$ (red), $p(2 \times 1)$ (green) and (3×2) (blue) domains. Stripes with different pattern are formed along the $[1\bar{1}0]$ direction (0.51 V, 0.33 nA).

However, after further cooling to ~ 50 K, STM shows the coexistence of $c(2 \times 2)$, (2×1) and (3×2) structure. Furthermore stripes characterised by the three different

patterns are formed along the $[1\bar{1}0]$ direction. The described transition is completely reversible and a perfect $c(2\times 2)$ is recovered when the sample is heated up back to room temperature.

2.3.4 Discussion

Two complementary questions must be answered to: why just one phase is observed at room temperature if two or three phases are almost degenerate, it is counterintuitive, that the rise of temperature increases order and its lowering produces disorder. And on the other hand, if the $c(2\times 2)$ phase is more stable than the $p(2\times 1)$ and (3×1) , why do these two phases appear at low temperature?

Dilatation

A simple explanation in terms of a phase transition in the Br-overlayer due to the thermal contraction/expansion of the Pt substrate can not be in principle ruled out. Decreasing the lattice constant in the simulations (e.g. performing a LDA calculation, or using the experimental lattice constant instead of the calculated one, in both cases this represents a shrinking of the substrate compared with GGA) enhances the attractive interaction between the atoms in the $[001]$ -lines. On the other side, the order of magnitude of this phenomenon appears much too small to drive a phase transition of such proportion.

Thermodynamics

The stabilisation of one single phase at high temperature at the expense of the other two degenerate phases could be in principle driven by the entropy (S). The internal energy of the three phases, as calculated by means of DFT, is in fact nearly the same ($U_{c(2\times 2)} \sim U_{p(2\times 1)} \sim U_{(3\times 2)}$) at 0 K, but the free energy ($F = U - TS$) can be lowered in one phase at higher temperatures if the loss in configurational entropy

is compensated by a gain in the vibrational entropy. This scenario is realised by two very different vibrational potentials, as sketched in figure 2.15. This mechanism could explain to some degree the dominance of the $c(2\times 2)$ phase at room temperature, and the coexistence of the $c(2\times 2)$ and the $p(2\times 1)$ phases at low temperature. But DFT predicts a difference in adsorption energy in the order of 40 meV between the (3×2) and the other phases, which is not negligible at 50 K. Purely statistical considerations can therefore not completely explain the phase transition, nor help to characterise the fluctuations observed at 50 K.

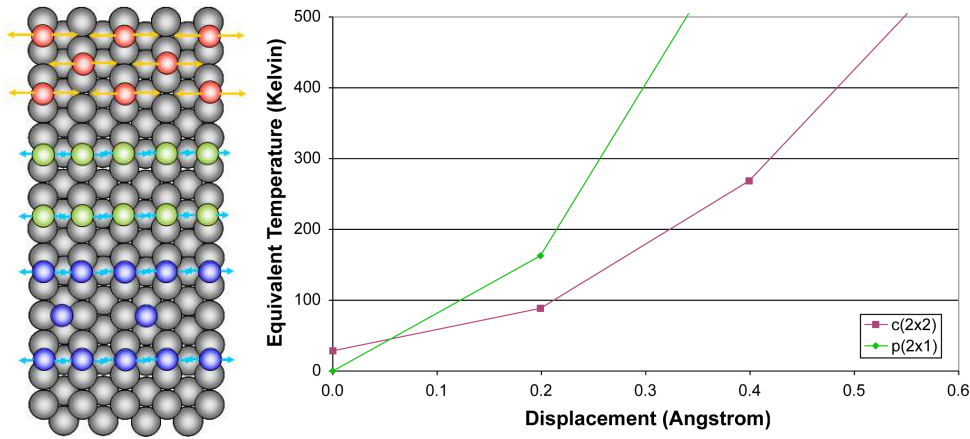


Figure 2.15: Due to the geometry of the three phases, a different vibrational potential could be expected for the $c(2\times 2)$ with respect to the $p(2\times 1)$ and (3×2) phases. The graph on the right shows the variation of the adsorption potential caused by the displacement of the Br atoms in the (2×2) unit cell with respect to one another as shown in the figure on the left. The (3×2) -phase potential is not given because it is not directly comparable to the others due to the different magnitude of the unit cell. The equivalent temperature is calculated as $\Delta E/k_B$, where ΔE is $E_{displaced} - E_0$, with E_0 representing the energy of the undistorted $p(2\times 1)$ phase.

Charge Density Waves (CDW)

In view of the shortcomings of the above interpretations, an improved long range ordering at higher temperatures can only be explained if one assumes temperature de-

pendent interactions to prevail into the system. A natural candidate is a Peierls-type $2k_F$ interaction in the electronic system. At low temperature, such an interaction drives the system into a CDW phase, while with rising T the corresponding order parameter drops off due to thermal excitation of electrons across the Peierls gap. Thus the CDW dies out and the local adsorbate-adsorbate interactions, which are much less temperature-dependent, favour the global formation of the $c(2\times 2)$ phase. However it is important to notice that the CDW is apparently not commensurate. For an incommensurate CDW it has been predicted that a well-defined transition temperature is replaced by fluctuations over a wide temperature range and at low T phase separation into domains with different periodicities takes place [49, 50]. The incommensurability is also supported by angle-resolved photoemission experiments, which yield $1/4 G < k_F < 1/3 G$ for the relevant surface state (G is a reciprocal surface lattice vector) [31].

The following model for the observed phase transition can thus be conceived: at 50 K the $c(2\times 2)$, $p(2\times 1)$ and (3×2) structure are degenerate, with the last phase being locally stabilised by the incommensurate Peierls interaction. As the temperature is increased, the Peierls interaction is weakened, which destabilises the other two phases relative to the $c(2\times 2)$ structure. Fluctuations are thermally excited, but with increasing preponderance of the $c(2\times 2)$ phase they drop off and an even better $c(2\times 2)$ order develops. Finally at 375 K the $c(2\times 2)$ structure is destroyed as well in a sharp order-disorder transition. The results can be related to the generic phase diagram of low-dimensional systems, which is shown in figure 2.16. The phase diagram is sketched for an array of one-dimensional systems where the coherence between these sub-units depends on the strength of a coupling parameter t_{\perp} .

For low values of t_{\perp} (left side of the phase diagram) the one-dimensional units are almost independent and undergo a Peierls transition below the mean field temperature T_{MF} . If the temperature is decreased below the coherence temperature

T_{coh} the residual coupling is still enough to induce coherent order between the rows and thus a two-dimensional CDW. On the opposite side of the phase diagram (that is for strong coupling between the sub-units) the coherence temperature T_{coh} is higher than T_{MF} . The case of the $c(2 \times 2)$ -Br/Pt(110) is represented by the high t_{\perp} region but is complicated by the strong Br-Br repulsion. Rising the temperature above T_{coh} causes a loss of coherence from row to row (the order-disorder transition occurring at 375 K). Below T_{coh} a long-range ordered phase (the $c(2 \times 2)$ phase) is stabilised by the next neighbour repulsion, but as the mean-field Peierls transition temperature is approached, fluctuations increase and finally lead below T_{MF} to the evolution of an inhomogeneous ground state with stripes of $c(2 \times 2)$, $p(2 \times 1)$ and (3×2) patterns.

It is believed that in high- T_{coh} 's a similar phase diagram applies [1]. In that case t is the hopping matrix element and the inhomogeneous ground state is the so-called striped phase [51]. Therefore the present observations are of general relevance for the understanding of correlated systems and particularly high- T_{coh} 's.

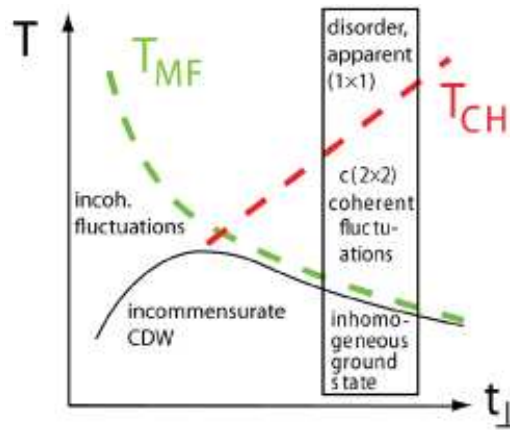


Figure 2.16: Generic phase diagram of quasi-1D systems.

Local Interactions and Energy Tradeoff

It must be noticed that both, the phase transitions and fluctuations can also be explained by simply considering next neighbours interactions. In both, the $p(2\times 1)$ and (3×2) phases the $[001]$ lines are stabilised respect to the “zigzag”- $c(2\times 2)$ arrangement due to a delicate energetic trade-off: Br-atoms seem to be exactly small enough, to avoid direct repulsion between adatoms in neighbouring close packed rows. As can be observed in figure 2.15, though, even a small displacement of the atoms along $[001]$ towards each other makes them interact. The coherence parameter t_{\perp} is therefore dependent on temperature.

Therefore, at room temperature the adsorption potential at a SB site where next neighbouring sites in the $[001]$ direction are occupied by vibrating Br atoms ($p(2\times 1)$ arrangement) is lower than in the $c(2\times 2)$ phase; registry shifts between neighbouring 1-D units are less likely and a global $c(2\times 2)$ phase is observed. Decreasing the temperature, the correlation is decreased as well, at 110 K the $c(2\times 2)$ phase is strongly disturbed because $p(2\times 1)$ -SB sites can be statistically occupied for a significant portion of time. Still decreasing the temperature, the atomic mobility falls off, until the adatoms are frozen in their adsorption sites, either in $[001]$ lines ($p(2\times 1)$ arrangement) or not (“zigzag”- $c(2\times 2)$ arr.).

As it can be observed in figure 2.17, the spacing between the $[001]$ lines can be either two or three times a next-neighbour distance in the $[1\bar{1}0]$ direction. In the first case, a regular $p(2\times 1)$ phase is obtained, otherwise a phase slip is produced. Here, every second LB adsorption site between the lines is occupied in order to keep the coverage of $1/2$ ML, forming a (3×2) structure.

Summarising, four mechanisms are proposed to describe the observed phase transitions and fluctuations, the last two of them can explain the details of the observed transformations. Spots of the (3×2) phase can be observed even at higher

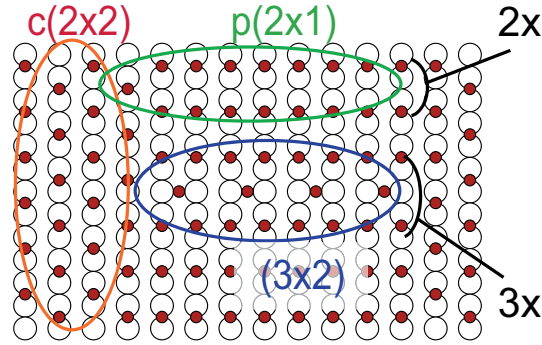


Figure 2.17: Schematic representation of the three Br phases, which coexist at low temperature: The $c(2\times 2)$ phase in red, the $p(2\times 1)$ phase in green and the (3×2) phase in blue.

temperatures in correspondence of defects. This observation could again be explained in terms of an electronic effect, which stabilises a CDW with the proper periodicity. It can be also interpreted as a direct interaction: the defect pins a phase slip, which must be compensated by the occupation of some LB sites, with a small energy cost.

Since the CDW is not commensurate, the (3×2) stabilisation is **local**. DFT can only simulate **global** effects, because the modelling of local effects would require huge cells. By means of DFT, one can therefore not exclude, that a CDW plays a role in the process, but it is not possible to prove its presence or even that it is the mechanism, which drives the transformation.

2.4 Cl/Pt(110): A Global $p(2\times 1)$ Phase

For a coverage of $1/2$ ML of Cl on Pt(110) every second SB-site is occupied, just as for $c(2\times 2)$ -Br/Pt(110), but without phase slip from row to row [28]. Therefore, a stable $p(2\times 1)$ structure is formed. This observation is confirmed by the present DFT calculations. This property marks a difference between Cl/Pt(110) and Br/Pt(110):

for the latter $p(2\times 1)$ and $c(2\times 2)$ geometries are almost degenerate and have been in fact observed to coexist at low temperature. The difference in behaviour between Cl and Br can be traced back to the difference in atomic radius: Cl is smaller than Br, so there is less repulsion between next-neighbouring Cl atoms in the $p(2\times 1)$ phase.

2.4.1 Geometry

The compilation of the experimental and calculated optimum geometry is given in Tab.2.7. In contrast to the $c(2\times 2)$ -Br/Pt(110) structure, the adsorption of Cl in a $p(2\times 1)$ geometry induces not only pairings and changes in the interlayer distances, but even bucklings involving atoms in the third and fifth layer.

		d_0	Δd_{12}	Δd_{23}	Δd_{34}	Δd_{45}
Cl	present	1.920	-0.104	0.028	0.010	0.000
	LEED	1.93	-0.10	0.03	0.04	-0.02
	FLAIR-LDA-9L	1.87	-0.12	0.03	0.01	0.00
	FLAIR-GGA-9L	1.93	-0.13	0.03	0.01	-0.01
Br	present	2.067	-0.110	0.029	0.009	-0.001
		p_1	p_3	b_2	b_4	d
Cl	present	0.006	0.008	0.075	0.031	1.409
	LEED	0.00	0.00	0.08	0.02	1.385
	FLAIR-LDA-9L	0.01	0.01	0.05	0.01	1.378
	FLAIR-GGA-9L	0.00	0.01	0.07	0.02	1.407
Br	present	0.010	0.007	0.062	0.027	1.409

Table 2.7: DFT calculated and experimental structural parameters of the Cl/Pt(110)- $p(2\times 1)$ phase. d_0 denotes the adlayer-substrate distance, $\Delta d_{i,i+1}$ the changes in the interlayer spacing with respect to the ideal bulk spacing d , and p_i the lateral pairing in layer i . Signs of the lateral pairing parameters p_i are given with respect to the position of the Cl atoms. Calculated parameters of the (2×1) -Br surface are given for comparison. All given values are expressed in Å. LEED data are found in [28] and FLAIR results in [36]

2.4.2 Electronic Properties

In figure 2.18 the p states of Cl are compared with the d states of the first Pt layer atoms. As for Br, the p_z and p_x Cl states, most involved in the bonding, have a typical bonding–anti bonding correlation with the d_{xz} respectively d_{z^2} Pt states. In

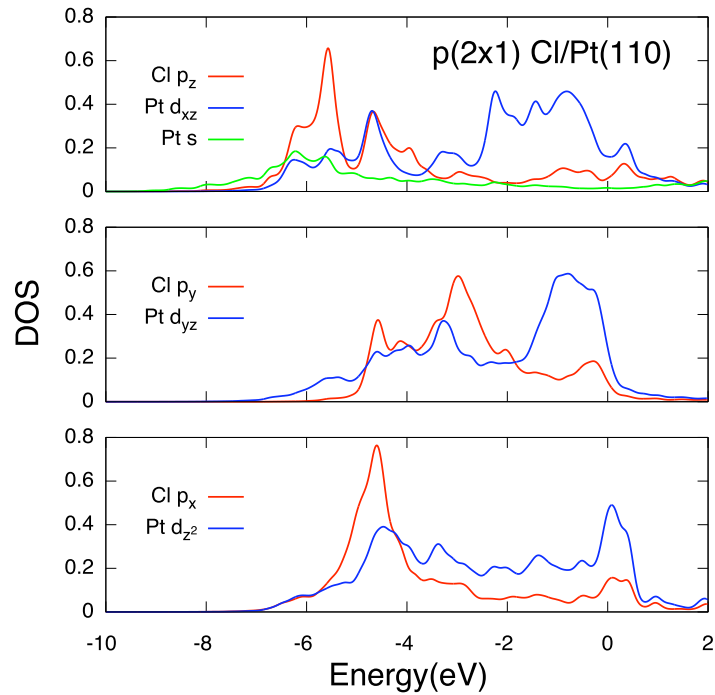


Figure 2.18: Comparison between the p states of Cl and the d states of the underlying Pt atoms. As for Br, the p_z and p_x Cl states have a typical bonding–anti bonding correlation with the d_{xz} respectively d_{z^2} Pt states, while the Cl p_y and Pt d_{yz} are quite uncorrelated.

figure 2.19 the density of states (DOS) of the p states of Cl adatoms in the SB-p(2×1) phase are compared with the DOS in the SB-c(2×2). As noticed for Br, the binding states are not affected by the phase slip, the only change being in the p_y state. A RT-STM picture of the p(2×1) structure is shown in Fig.2.20. The star-shaped protrusions, already reported in [28], are due to Pt-Cl complexes, as discussed in

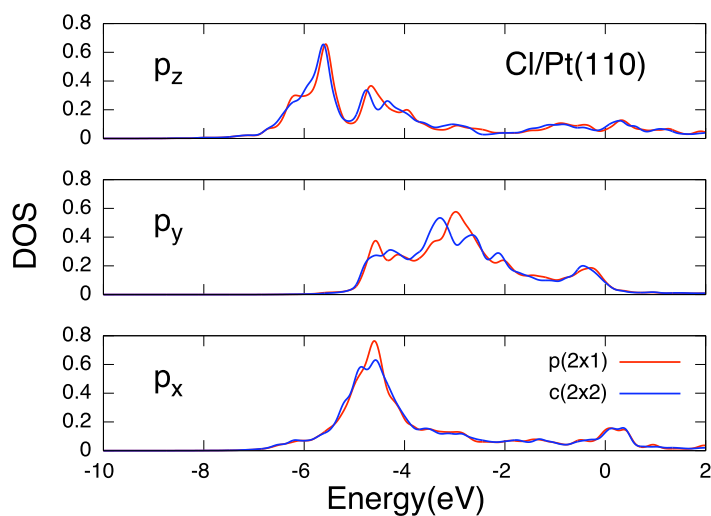


Figure 2.19: A comparison between the states in the $p(2\times 1)$ and in the $c(2\times 2)$ phase (right) shows that the states are only slightly affected by a registry shift of adatoms on neighbouring close-packed rows. As for Br, least affected are the P_x and p_z states most involved in the bonding.

the next section. At variance with the $c(2\times 2)$ -Br/Pt(110), neither phase transition nor “liquid” phase are observed upon cooling, while a well ordered $p(2\times 1)$ structure survives down to 110 K.

In figure 2.21 a the charge densities of the Cl- and Br- $p(2\times 1)$ structures across a plane normal to the Pt surface and parallel to the $[1\bar{1}0]$ direction is plotted. The comparison of the two structures allows to appreciate their striking similarity, the only difference being the halogen covalent radius.

2.5 I/Pt(110): A Global SB- $c(2\times 2)$ Phase

Even if I prefers long bridge sites in the single-adatom approximation, the SB- $c(2\times 2)$ is more stable than a LB- $c(2\times 2)$ arrangement. In the $c(2\times 2)$ structure, in fact, paired neighbouring Pt atoms in the first metal layer move in opposite directions,

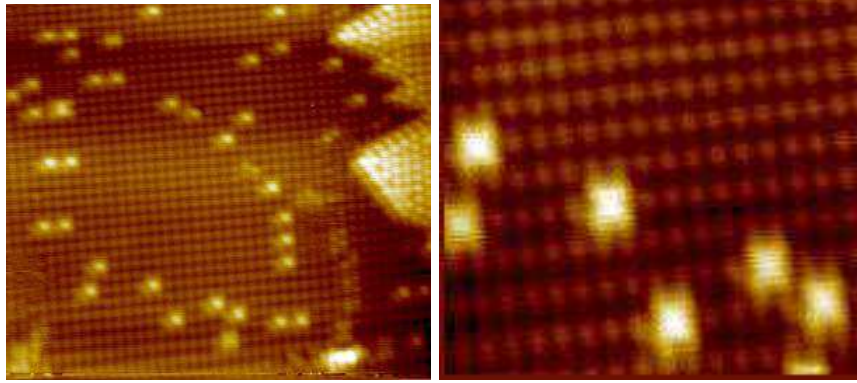


Figure 2.20: LT-STM ($T \simeq 110$ K) images of p(2×1)-Cl/Pt(110). Left: -0.13 V, 0.13 nA. Right: 0.3 V, 0.1 nA.

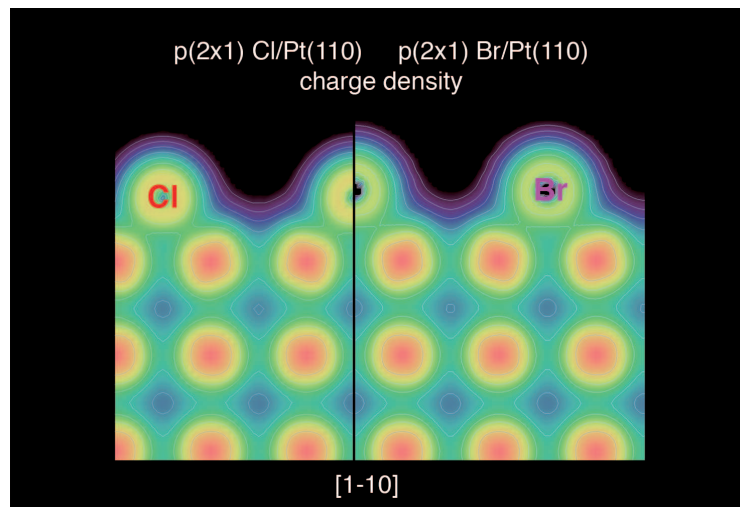


Figure 2.21: Charge densities of the Cl- and Br-p(2×1) structures. They are quite similar, the only major difference being the halogen covalent radius.

which causes a substantial strain in the substrate.

	d_0	Δd_{12}	Δd_{23}	Δd_{34}	Δd_{45}	p_1	p_2	p_3	p_4
I	2.194	-0.110	0.025	0.002	-0.002	0.018	-0.003	0.006	0.008
Br	2.075	-0.105	0.025	0.011	0.000	0.002	-0.015	0.004	0.009

Table 2.8: Structural parameters of the I/Pt(110)-c(2×2) phase compared with the (experimentally better known) correspondent Br phase. d_0 denotes the adlayer-substrate distance, $\Delta d_{i,i+1}$ the changes in the interlayer spacing with respect to the ideal bulk spacing, and p_i the lateral pairing in layer i , all values given in Å.

Both, the deformation and the induced strain are bigger for adsorption on LB, the strain more than compensates the preference of I for long bridge sites.

Chapter 3

Halogens on Pt(110), high coverages

In the previous chapter halogen structures with a coverage up to $1/2$ ML on a Pt(110) surface were discussed. In the present chapter the pure Br, pure Cl and mixed Br-Cl phases observed above $1/2$ ML coverage are analysed.

3.1 Bromine on Platinum

Just above $1/2$ ML coverage the $c(2\times 2)$ order is destroyed, with increasing coverage the surface undergoes two phase transitions: $c(2\times 2) \Rightarrow (3\times 1) \Rightarrow (4\times 1)$. Experimental observations on the mentioned coverage regime can be found in [31] and [52].

3.1.1 Experimental Evidence

In the coverage range $1/2 \text{ ML} < \Theta \leq 2/3 \text{ ML}$ a phase transition takes place from the already described $c(2\times 2)$ to a new (3×1) phase. There is no continuous transition pathway leading to the (3×1) phase. Rather, the global $c(2\times 2)$ order is destroyed as the Br coverage is increased above $1/2$ ML. For a coverage slightly higher than $1/2$ ML, the $c(2\times 2)$ arrangement is only observed at steps or close to defects, while the main phase is an apparent (1×1) , as shown in figure 3.1 [52].

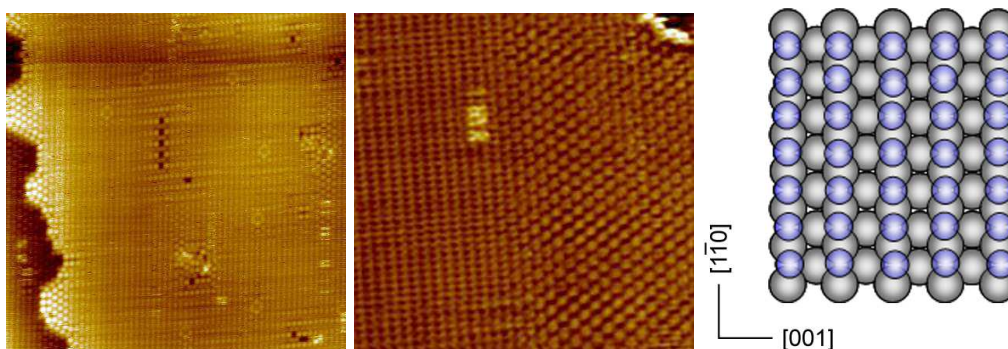


Figure 3.1: a), b) STM pictures for a coverage slightly above $1/2$ ML. On the left ($300 \times 300 \text{ \AA}^2$, 0.45 V , 0.21 nA) the $c(2 \times 2)$ is restricted to terrace edges or to certain defects, while the surface is dominated by the (1×1) structure. Around some kind of defect (black spots) even (3×1) domains are recognised. On the right ($150 \times 150 \text{ \AA}^2$, 0.16 V , 0.36 nA) the boundary between a $c(2 \times 2)$ and an apparent (1×1) domain is seen [52]. c) Sketch of the apparent (1×1) structure observed by STM. Due to Br–Br repulsion, the occupation of neighbouring SB-sites is energetically forbidden.

Such a phase would imply a coverage of 1 ML, which is not compatible with the nominal one. Furthermore, the extremely high ($\sim 0.9 \text{ eV}$) repulsion energy between neighbouring SB-sites would forbid a (1×1) structure at room temperature even assuming a local coverage of 1 ML. The STM image can be interpreted in terms of a time averaged picture of fast fluctuations: Br atoms hop from short-bridge to short-bridge site sampling in average every site with the same probability. This is the same behaviour observed at $\Theta = 1/2 \text{ ML}$ for temperatures above the coherence temperature T_{coh} (s. chapter 2) [48].

At small additional coverages, antiphase (3×1) domains surrounded by the (1×1) phase are observed. These domains increase with coverage, their boundaries disappear for Θ between 0.55 ML [31] and 0.58 ML [52] and a globally developed (3×1) phase results (see fig 3.7). The (3×1) phase appears characterised by alternating bright and dark parallel lines extending along the $[001]$ direction, which suggests that the Br atoms occupy two different adsorption sites.

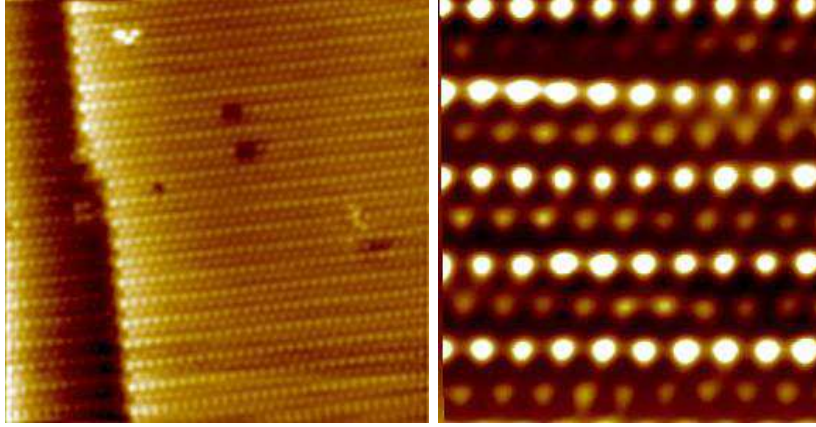


Figure 3.2: STM pictures of global (3×1) -Br/Pt(110) phase (0.6 V, 0.1 nA [52])

Further increasing the Br coverage, an arrangement with (4×1) periodicity is observed [53, 52]. STM images are shown in fig 3.3. Bright lines extending along

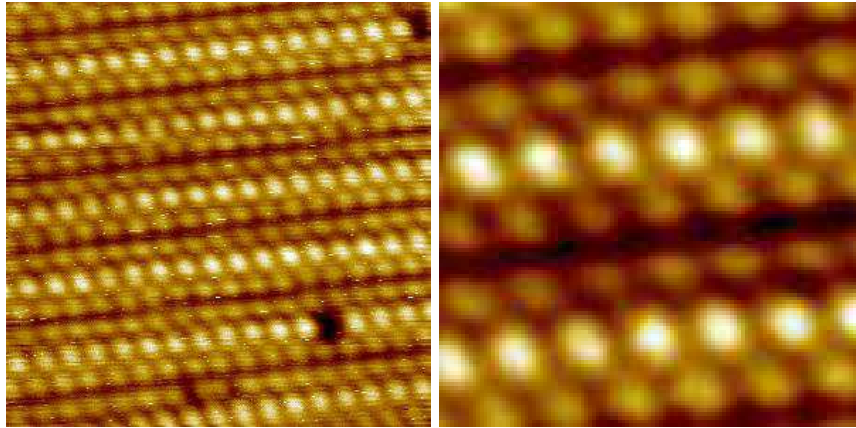


Figure 3.3: STM picture of (4×1) -Br/Pt(110) (Left: $80\times 80 \text{ \AA}^2$, 0.45 V, 0.4 nA. Right: $30\times 30 \text{ \AA}^2$, 0.45 V, 0.44 nA [52].

the $[001]$ direction with a periodicity of 11 \AA ($\sim 4\times 2.77 \text{ \AA}$) in $[1\bar{1}0]$ direction are separated by dark double spots oriented in $[1\bar{1}0]$ direction with a spacing of 3.92 \AA in $[001]$ direction. The long-range order is perturbed by characteristic anti-phase domain boundaries in $[1\bar{1}0]$ direction. The displacement vector between neighbouring

domains amounts to two nearest neighbour distances (5.54 \AA) in the $[1\bar{1}0]$ direction.

3.1.2 Interpretation: The Global Br-(3×1) Phase

In the global Br $c(2\times 2)$ phase, each second SB adsorption site is occupied, which corresponds to a coverage of $1/2 \text{ ML}$. Because of the substrate-mediated repulsion in the $[1\bar{1}0]$ direction (s. par. 2.2.2), the occupation of further SB sites costs $\sim 0.9 \text{ eV}$ per adatom. The occupation of next neighbouring LB sites, instead, acts a repulsion of less than $\sim 0.2 \text{ eV}$. This causes the formation of domains of (3×2) phase on the surface with above stoichiometry statistical occupation of LB sites. The adatoms on LB have a great mobility along the $[001]$ direction at room temperature (see Fig.3.4), thus STM can only show a time averaged image where all LB sites appear occupied. The surface assumes thus a periodicity of (3×1) with one adatom on SB and one on LB per unit cell. The stoichiometric coverage of such an arrangement is $2/3 \text{ ML}$. The phase transition is described in [28].

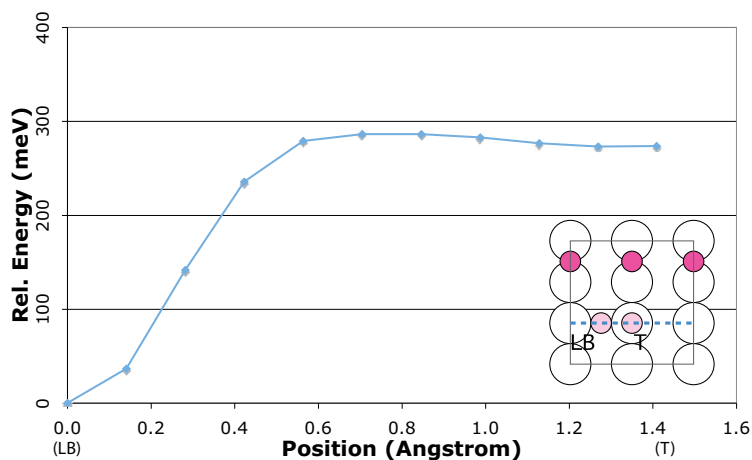


Figure 3.4: Adsorption energy calculated at different points along the line (light blue dashed line in the inset) connecting a LB and a neighbouring T position in the $[001]$ direction.

As the coverage is raised, the (3×1) domains increase until the whole surface

shows a global (3×1) phase. It must be noticed that this happens for a coverage (between 0.55 and 0.58 ML), which is much lower than the stoichiometric one. It has been suggested that a CDW stabilises the surface in this regime [31]. This could also explain the observation of (3×1) and (3×2) domains in the proximity of defects at $\Theta = 1/2$ ML. As the coverage is further increased, more and more next neighbouring LB sites are occupied. A global stoichiometric (3×1) phase is observed at $2/3$ ML coverage.

Geometry

The global (3×1) phase was characterised by C. Franchini and C. Deisl [31, 36, 28]. In figure 3.5 a ball model for the ideal coverage of $2/3$ ML is reported. With Br occupying both a short bridge and a long bridge site per (3×1) unit cell, not all adsorption sites are equivalent, which causes a buckling of 0.2 \AA in the Pt substrate. This buckling can be interpreted as a soft Raleigh phonon of threefold periodicity. The resulting average adsorption energy per atom, 1.55 eV , is $\sim 0.18 \text{ eV}$ lower than those calculated for the three degenerate phases at $1/2$ ML, the difference between the (3×1) and the (3×2) is due to the repulsion of neighbouring LB sites in the $[001]$ direction. For comparison: The energy difference between the LB-c(2×2) (no NN sites occupied) and the LB-p(2×1) phase (NN sites in the $[001]$ direction) is $\sim 0.17 \text{ eV}$ (see table 2.5).

In Tab. 3.1 a compilation of experimental and theoretical results for the p(3×1) phase is presented. The calculation have been performed with the same setup described before, but in this case a Monkhorst-Pack k -mesh of $4 \times 6 \times 1$ points was adopted. Atomic relaxations occur not only near the surface but also in deeper layers. In fact, although Br resides in different sites (short and long bridges) the Br–Pt bond lengths $L_{SB} = 2.51 \text{ \AA}$ and $L_{LB} = 2.58 \text{ \AA}$ are very similar, which leads to a strong buckling for the Br adlayer and, consequently, for the top two Pt layers.

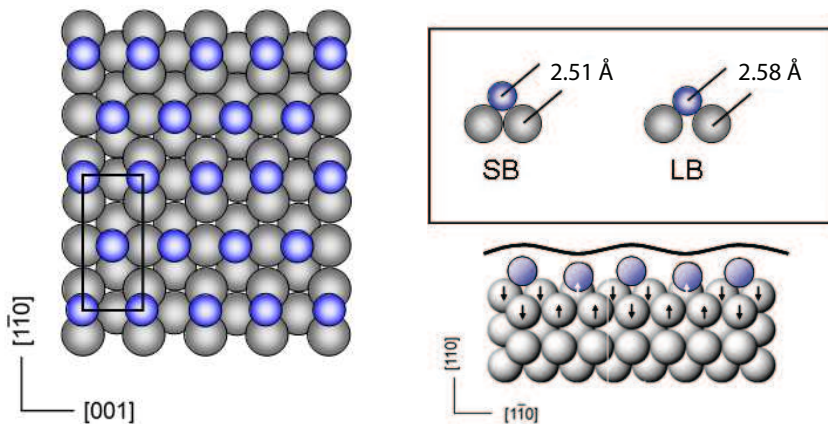


Figure 3.5: Ball scheme of the (3×1) -Br/Pt(110). A buckling of 0.2 \AA arises in the Pt-substrate.

Comparing L_{SB} and L_{LB} to the bond length calculated at $1/2\text{ ML}$ ($L_{SB} = 2.51\text{ \AA}$ and $L_{LB} = 2.55\text{ \AA}$) we can conclude that the covalent character of the halogen–metal bond is confirmed for this coverage range.

Electronic Properties

The main difference between the (3×1) and the $c(2\times 2)$ phases is that the two adatoms in the (3×1) unit cell are nonequivalent. On SB the p_x state of Br binds to the d_{xz} state of the underlying Pt atoms as in the $c(2\times 2)$ phase, while on LB the p_y state of Br is bound to the d_{yz} Pt-state. This difference is due to the better overlap of p_x - d_{xz} for SB, while due to the larger Pt–Pt separation p_y overlaps better with d_{yz} than d_{xz} . The density of states calculated for the Br- (3×1) structure is shown in figure 3.6. As in the $c(2\times 2)$ phase, the nature of the bonding is essentially covalent.

To conclude the discussion of the electronic properties of the (3×1) -Br/Pt(110) structure a comparison between the experimental and the calculated constant cur-

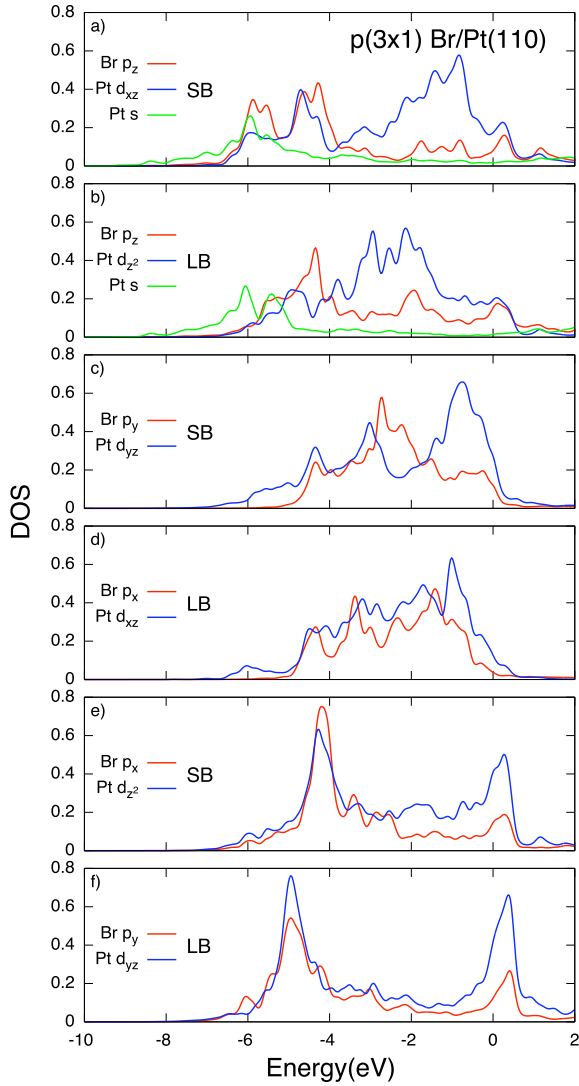


Figure 3.6: Calculated density of states of the Br-(3×1) phase. On SB the p_x state of Br binds to the d_{z^2} state of the underlying Pt atoms as in the $c(2\times 2)$ phase, while on LB the p_y state of Br is bound to the d_{yz} Pt-state, due to the increased overlap for d_{xy} as compared to d_{z^2} at LB sites, the comparison of the two pairs of states shows the a bonding–antibonding scheme, while the p_x state at SB and the . As in the $c(2\times 2)$ phase, the nature of the bonding is essentially covalent.

	d_{Br}	L_{SB}	L_{LB}	d	Δd_{12}	Δd_{23}	Δd_{34}	Δd_{45}
present	1.89	2.51	2.58	1.409	-0.045	0.013	0.013	-0.006
FLAIR-LDA	1.83	2.45	2.52	1.378	-0.06	0.00	+0.01	-0.01
LEED	1.91	2.53	2.54	1.387	-0.09	+0.01	+0.04	-0.01
	b_{Br}	b_1	p_1	b_2	p_2	b_3	p_3	b_4
present	0.25	0.20	0.01	0.08	0.02	0.00	0.02	0.02
FLAIR-LDA	0.25	0.21	0.01	0.10	0.02	0.02	0.02	0.03
LEED	0.26	0.25	—	0.10	—	0.01	—	0.04

Table 3.1: Structural characterisation of the (3×1) structure d_{Br} is the distance of the Br layer from the first Pt layer, L_{SB} , L_{LB} the bondlengths on short and long bridge respectively, d the bulk interlayer spacing, the Δd_{mn} 's are the deviations of the surface interlayer spacings from the bulk value, the b 's and the p 's are respectively the bucklings the pairings of the Br and substrate layers. FLAIR-LDA and LEED values are given in [36, 28, 31]

rent STM image is shown in figure 3.7. As for the $c(2 \times 2)$ phase the agreement between theory and experiment is very good not only in a qualitative way (the global (3×1) structure is well displayed) but even quantitatively. In fact, considering states satisfying resonant tunnelling condition for the applied bias voltage (12 meV) the resulting corrugation is identical to the experimental value, i.e. 0.25 \AA .

3.1.3 The Br- (4×1) Phase

It is difficult to determine the accurate coverage experimentally from temperature programmed desorption (TPD) spectrum, because desorption from Br layers with $\text{Br} > 1/2 \text{ ML}$ occurs partially as molecular Br_2 . However, from the excess exposures needed to prepare the (4×1) starting from the $c(2 \times 2)$ structure a total coverage of less than 1 ML can be estimated [53]. It is then natural to assume three Br atoms per unit cell, which results in an ideal coverage of $\Theta_{Br} = 3/4 \text{ ML}$. Guided by STM images, which show two classes of adsorbates (one per unit cell in the bright line and two in the dark stripe) and the previously solved (3×1) structure [31] structural models exhibiting two Br atoms in SB sites and one Br atom in the LB position or

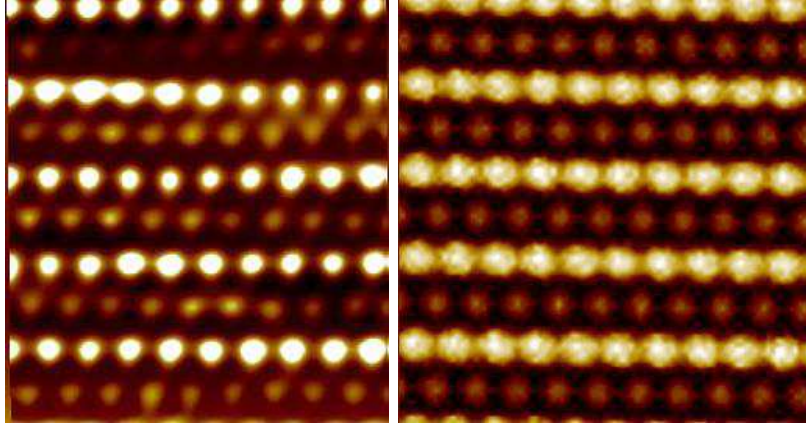


Figure 3.7: Comparison between experimental (left) and VASP-calculated (right) STM images of the Br/Pt(110)-p(3×1) surface.

vice versa were tried out.

Although the SB site yields the higher binding energy per Br atom, the arrangement with 2 atoms on SB and one on LB results less stable than the one with two atoms on LB and one on SB. This is due to an energy trade-off between adsorption energy ($E_{SB} - E_{LB} = 83 \text{ meV}$) and repulsion between next neighbours in the $[1\bar{1}0]$ direction ($E_{LB-LB} - E_{SB-SB} = \sim 0.36 \text{ eV}$, see table 2.5.). The repulsion is much stronger than the preference for SB over LB. This result is summarised in figure 3.8

This result is confirmed by means of the IV-LEED data, assuming 2 Br on SB a reasonable Pendry R-factor could not be achieved. RP remained above 0.55 for this input model. In contrast, a TensErLEED simulation using the model with two Br atoms in LB sites converged to $RP = 0.25$ (0.23 for integral and 0.26 for fractional order spots). This accuracy is comparable to the phases described thus far [53].

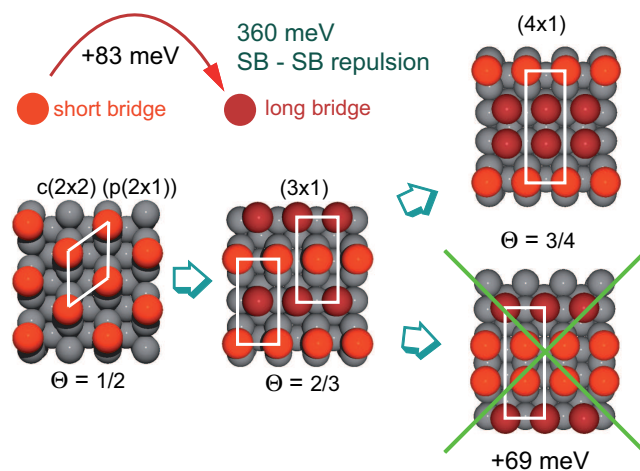


Figure 3.8: The Br- (4×1) arrangement with 2 adatoms on LB is more stable than the one with 2 adatoms on SB. The value of the repulsion is the difference between next neighbour SB-SB and next neighbour LB-LB interactions.

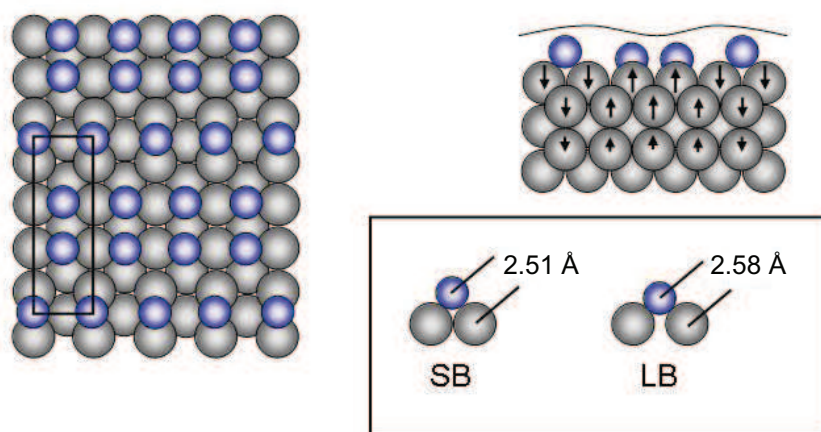


Figure 3.9: Geometry of the (4×1) -Br/Pt(110) surface resulting from DFT calculations and IV-LEED. [53]

d_{Br}	Δd_{12}	Δd_{23}	Δd_{34}	Δd_{45}	z_{Br1}	z_{Br2}	x_{Br2}
1.82	-0.02	-0.01	0.02	0.00	0.15	-0.08	-0.37
1.79	-0.02	0.03	0.01	0.00	0.17	-0.08	-0.38
z_{11}	z_{12}	z_{13}	z_{14}	x_{11}	x_{12}	x_{13}	x_{14}
-0.13	-0.13	0.13	0.13	0.04	-0.04	-0.09	0.09
-0.09	-0.09	0.09	0.09	0.09	-0.09	-0.10	0.10
z_{21}	z_{22}	z_{23}	z_{24}	x_{21}	x_{22}	x_{23}	x_{24}
-0.11	-0.01	0.13	-0.01	—	0.03	—	-0.03
-0.07	-0.01	0.10	-0.01	—	0.06	—	-0.06
z_{31}	z_{32}	z_{33}	z_{34}	z_{41}	z_{42}	z_{43}	z_{44}
-0.03	0.03	0.03	-0.03	0.00	0.04	0.00	-0.04
-0.02	0.02	0.02	-0.02	-0.01	0.04	-0.01	-0.03

Table 3.2: Geometrical characterisation of the (4×1) phase. d_{Br} is the distance between the Br-layer and the first Pt-layer Δd_{mn} is the change in the interlayer space between the m -th and the n -th layers, the z 's are the vertical distances from the layer average and the x 's the horizontal displacement from the positions in the clean surface. For each quantity the present DFT result a LEED experimental one [53] are given. All values are expressed in Å

Geometry

The geometry 4x1 phase was completely characterised by means of GGA-DFT. The results are shown in Tab 3.2

As already observed for the (3×1) structure, the Br-Pt bonding distance is nearly the same for the SB (2.51 Å) and the LB site (2.58 Å). The values are very close to the ideal covalent bond length of 2.50 Å. The displacement pattern of the top-layer Pt atoms is to some extent similar to the one observed for the (3×1) structure: The LB atoms are outward displaced. As there are two neighbouring LB sites involved, the buckling is consistent with a soft Raleigh phonon of fourfold periodicity. A concomitant charge density modulation can be anticipated from the alternating pairing - anti-pairing pattern along the close-packed Pt rows. Thus the structure seems compatible with a Peierls mechanism. The sequence of Br induced (n×1)

structures in this interpretation would then constitute another case of a tunable CDW as proposed for the Br/CO and the Br/NO co-adsorption systems [54, 55]. Further examination of such a model requires a precise mapping of the Fermi surface shifts occurring upon an increase of the Br coverage to $3/4$ ML.

In concluding the presentation of the geometrical results, it should be remarked that substitutional adsorption models can be ruled out for the (4×1) as well as for the (3×1) [31] and the $c(2\times 2)$ structure [40], both by theoretical considerations and by LEED. A comparison of selected calculated and measured IV-LEED curves is shown in Fig. 3.10 [53].

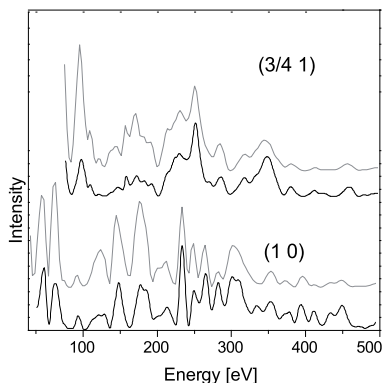


Figure 3.10: LEED intensity versus energy for a fractional and an integer order spot, respectively. Black: Measured IV-LEED curve, grey: calculated IV-LEED curve as obtained for the structural model shown in Fig. 3.9

Electronical Properties

The density of states calculated for the Br- (4×1) structure is shown in figure 3.11. As in the (3×1) phase, two nonequivalent sites are occupied.

Typical STM images of the (4×1) -Br/Pt(110) surface together with the corresponding LEED pattern and a simulated STM image on the basis of the Tersoff-Hamann model [21, 22] are shown in Fig. 3.12. The experimental STM image shown in Fig. 3.12a exhibits a striking agreement with the calculated image displayed as an inset in Fig. 3.12a and 3.12c. Fig. 3.12c shows an STM image, as it was also occasionally measured on the (4×1) structure.

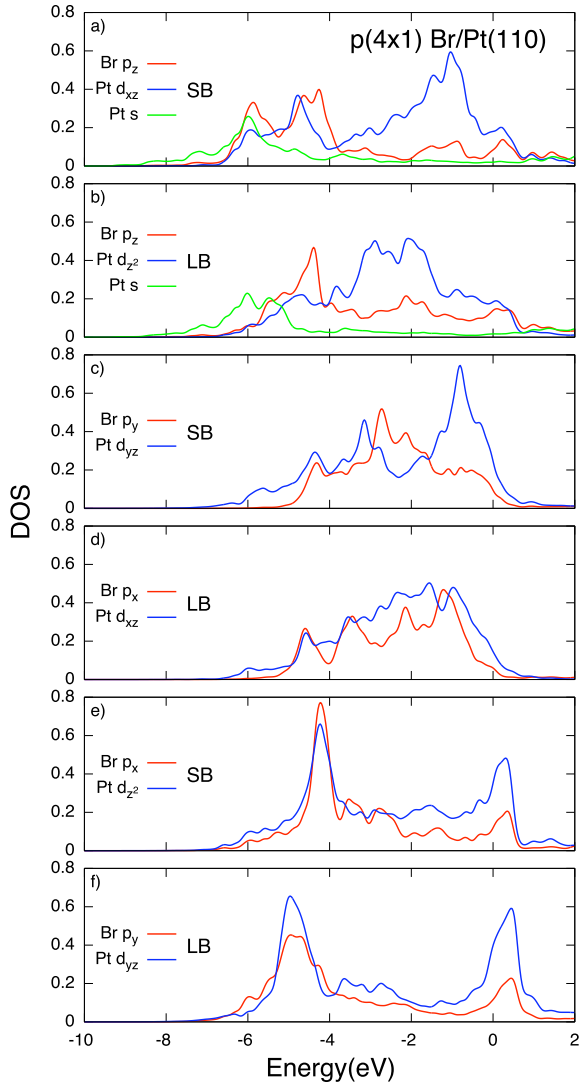


Figure 3.11: Calculated density of states of the Br-(4 \times 1) phase. On SB the p_x state of Br binds to the d_{z^2} state of the underlying Pt atoms as in the c(2 \times 2) phase, while on LB the p_y state of Br is bound to the d_{yz} Pt-state, due to the increased overlap for d_{xy} as compared to d_{z^2} at LB sites, the comparison of the two pairs of states shows the a bonding–antibonding scheme, while the p_x state at SB and the . As in the c(2 \times 2) phase, the nature of the bonding is essentially covalent. All states are strikingly similar to the corresponding states in the (3 \times 1) phase (see Fig. 3.6).

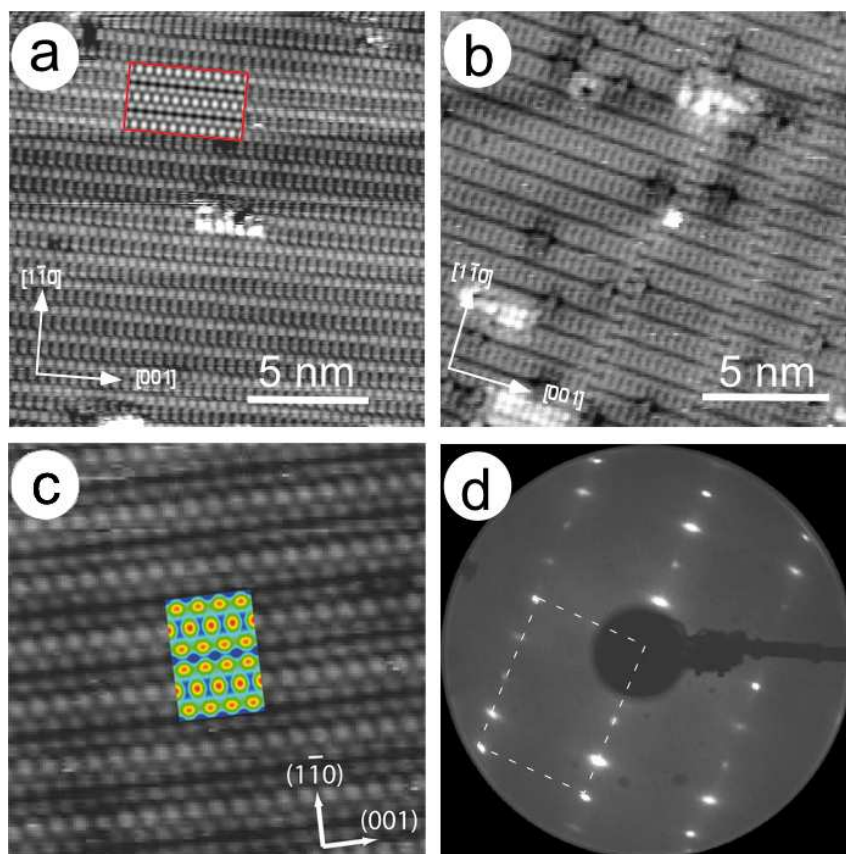


Figure 3.12: a): Large-scale STM scan of a Br induced (4×1) structure on Pt(110) (308 mV; 0.1 nA). The inset (red frame) shows a calculated STM image; b): Large-scale STM image recorded at lower tunnelling resistance showing inverted contrast (-40 mV; 0.57 nA); c): Part of image 3a at a bias of 40 mV. The coloured inset again shows a calculated STM image, where blue relates to low and red to high LDOS; d): LEED image of the Br induced (4×1) structure on Pt(110). The white rectangle marks the (4×1) unit cell.

3.1.4 Conclusions

All the phases observed up to $3/4$ ML coverage are described, the DFT results are in good qualitative and quantitative agreement with the experiment. Based on the present data, it is not possible to decide, whether long-range forces are actually determining the phase transitions $c(2\times 2) \implies (3\times 1) \implies (4\times 1)$. The same transitions could be caused by short-range interactions as well, due to the strong anisotropic repulsion between neighbouring adsorbates. The repulsive interaction is considerably smaller for the occupation of neighbouring LB than for the more energetically favourable SB sites. Thus the reduced repulsion compensates for the lower binding energy in the LB site. In the (4×1) phase, the repulsion is further reduced by the displacement of the LB Br atoms along $[1\bar{1}0]$, which increases their distance by 0.74 \AA . The displacement pattern in the Pt top-layer could then be explained by the tendency to maintain the optimum bond length to the Br atoms. In such a local-interaction model the main problem is to provide a rationale for the strongly differing repulsion of Br in neighbouring LB and SB sites, respectively. Taking into account the identical distances and the very similar bonding character this has to be attributed to a substrate mediated interaction. In view of the evidence for quasi-1D electronic surface states localised along the close-packed Pt rows [56], it appears plausible that the substrate mediated interaction is rather different for the two sites.

In summary, the present (4×1) results once again demonstrate the high reliability of structure determination using first-principles calculations. It does not resolve the question, whether the Br induced $(n\times 1)$ structures are further stabilised by a Peierls pure CDW mechanism. Clearly, adsorbate-adsorbate interactions mediated by substrate electronic states play an important role in the stabilisation of these peculiar structures. Further investigations of these phases could help to understand the energetics of this interesting, strongly anisotropic system.

3.2 Chlorine on Platinum

The phase transitions observed by adsorption of further chlorine on the Cl-p(2×1) as well as on the Br-c(2×2) surface are analysed and similarities and differences regarding the corresponding pure-Br phases discussed.

3.2.1 Experimental Evidence

Dosing 0.16 and 0.25 ML of Cl on the p(2×1) at room temperature, the formation of respectively (3×1) and (4×1) domains can be observed by STM and by LEED [36, 28, 57]. The order of these structures however is strongly perturbed by the presence of the already mentioned star-shaped protrusion (“stars” in the following), as shown in Fig. 3.13. Upon annealing to about 675 K the (3×1) and (4×1) phases evolve into an array of stars characterised by a (4×2) periodicity. This new structure is well ordered along the $[1\bar{1}0]$ direction, while frequent phase slips occur along the $[001]$ direction.

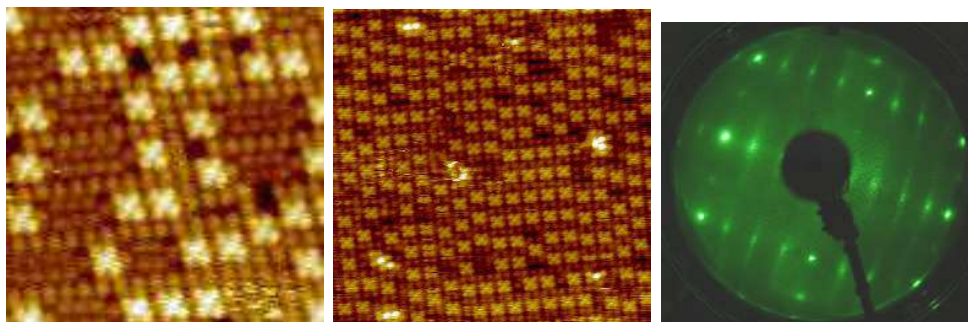


Figure 3.13: Left: RT-STM image showing a coexistence of (3×1), (4×1) and (4×2) domains ($200 \times 200 \text{ \AA}^2$ 0.48 V, 0.34 nA). Centre: RT-STM images of (4×2)-PtCl₄/Cl/Pt(110) ($200 \times 200 \text{ \AA}^2$ 0.48 V, 0.34 nA). Right: The (4×2) periodicity is clearly identified in its LEED pattern [52].

X	d_X	L_{SB}	L_{LB}	d	Δd_{12}	Δd_{23}	Δd_{34}	Δd_{45}
Br present	1.89	2.51	2.58	1.409	-0.045	0.013	0.013	-0.006
Cl present	1.76	2.39	2.50	1.409	-0.041	0.015	0.018	-0.001
Cl FLAIR-LDA	1.83	2.48	2.52	1.378	-0.06	0.00	+0.01	-0.01
X	b_X	b_1	p_1	b_2	p_2	b_3	p_3	b_4
Br present	0.25	0.20	0.01	0.08	0.02	0.00	0.02	0.02
Cl present	0.22	0.21	0.02	0.11	0.02	0.01	0.02	0.03
Cl FLAIR-LDA	0.25	0.21	0.01	0.10	—	0.02	—	0.02

Table 3.3: Comparison of the Cl- and Br-(3×1) structures. d_X is the distance of the halogen layer from the first Pt layer, L_{SB} , L_{LB} the bondlengths on short and long bridge respectively, d the bulk interlayer spacing, the Δd_{ij} 's are the deviations of the surface interlayer spacings from the bulk value, the b 's and the p 's are respectively the bucklings the pairings of the halogen and substrate layers. FLAIR-LDA values are taken from [36]. The difference between the present GGA and the FLAIR-LDA results is mostly due to the different lattice constant.

3.2.2 DFT Interpretation: The Pure (3×1) and (4×1) Phases

DFT calculations predict that for 2/3 ML of Cl on Pt a (3×1) structure, accompanied by a buckling in the Pt substrate as in the case of Br, is energetically possible.

The (3×1) Cl phase was characterised by Franchini [36]. Its geometry is compared with the corresponding (3×1)-Br in table 3.3

The density of states calculated for the Cl-(3×1) structure show a striking similarity to the corresponding Br phase: On SB the p_x state of Cl binds to the d_{z^2} state of the underlying Pt atoms while on LB the p_y state of Cl is bound to the d_{yz} Pt-state. Because of the higher electronegativity of Cl, it attracts more charge than Br and its states are more occupied.

The mentioned energetic trade off, causing the occupation of 2 LB sites per unit cell in the Br-(4×1) phase, is much less efficient for the corresponding Cl phase. In fact, both (4×1)-Cl configurations are almost degenerate, and the relative stability depends critically on computational parameters like the Pt lattice constant.

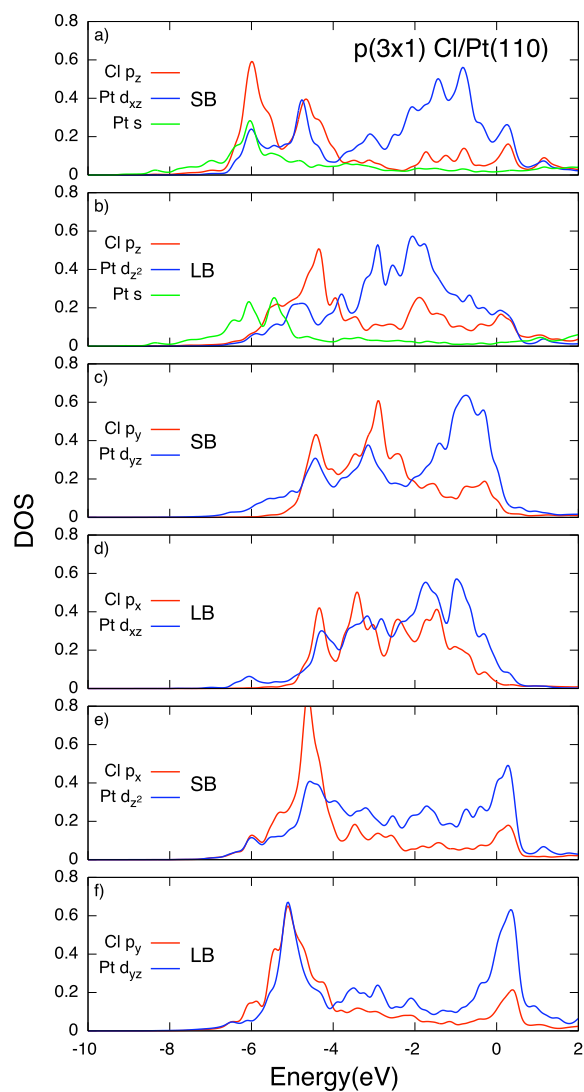


Figure 3.14: Calculated density of states of the Cl-(3 \times 1) phase: On SB the p_x state of Cl binds to the d_{z^2} state of the Pt atoms below while on LB the p_y state of Cl is bound to the d_{yz} Pt-state. Because of its higher electronegativity, Cl attracts more charge than Br and its states are more occupied.

Halogen	arrangement	LDA (eV)	GGA (eV)
		$d = 3.9085 \text{ \AA}$	$d = 3.986 \text{ \AA}$
Cl	SB + 2 LB	-326.320	-265.420
	LB + 2 SB	-326.240	-265.442
	difference (meV)	-80	+21
Br	SB + 2 LB	-325.431	-264.419
	LB + 2 SB	-325.244	-264.343
	difference (meV)	-187	-75

Table 3.4: Comparison of the absolute adsorption energies (in eV per (4×1) cell) and bondlengths of both (4×1) arrangements for Cl and Br in the LDA and GGA (PW91) approximations. In the LDA approximation both halogens prefer a SB LB LB ordering, in agreement with the experiment. The GGA approximation predicts for Cl a slight preference for the LB SB SB ordering.

The GGA approximation is known to overestimate bondlengths, which results in a larger lattice constant for the Pt substrate, which favours the arrangement with 2 adsorbates on SB and one on SB unlike for Br. Calculations performed with experimental and LDA lattice constant show an arrangement with 2 adsorbates on SB and one on LB to be more stable. STM experiments seem to confirm this last result. A detailed investigation of the energetics is shown in Tab 3.4.

3.2.3 The Cl- (4×2) Phase

The analysis of the left image in Fig. 3.13, where (4×1) and (4×2) domains coexist, allows the determination of details of the latter structure. From a comparison between the two domains, one can infer, that the central atom of the stars sits in the four-fold hollow site. The central atom appear to protrude beyond its four ligands, if the unoccupied states are sampled by STM, while in the filled-states image, only the central atom is seen at all [52] (Fig. 3.17). Hence, the unoccupied and even more the occupied local density of states (LDOS) are higher for the central atom, indicating that the central atom belongs to a chemically different species than the

peripheral ones. The distance between peripheral and central atoms in the stars is $\sim 2.44 \text{ \AA}$ while the distance between the peripheral atoms amounts to about 3.5 \AA . An explanation of this cluster in terms of pure Cl structure can be excluded, as the fourfold hollow position is very unstable for Cl (see Fig. 2.7, chapter 2) and the Cl-Cl repulsion is high for distances below 5.5 \AA [31]. The fourfold hollow site is on the contrary the naturally favoured adsorption site for a Pt adatom. The Cl atoms between the stars and the peripheral cluster atoms add up to a coverage of $\Theta = 6/8 = 3/4 \text{ ML}$, which coincides with the Cl coverage calibration. One can therefore conclude that the peripheral cluster atoms are Cl, while the central atom is Pt. A model of this phase is shown in Fig. 3.15.

A DFT stability investigation performed for some mixed Cl-Pt arrangements with (4×2) periodicity, compatible with a (4×1) phase (compare Fig. 3.13 and 3.15) confirms the PtCl_4 hypothesis. The results are shown in Fig. 3.16.

The Pt-Cl bond length in a DFT-GGA simulation is 2.33 \AA , compared to 2.31 \AA in K_2PtCl_4 [58]. STM images, show larger a bondlength of 2.44 \AA for the adsorbed PtCl_4 . DFT VASP simulations yield an almost flat PtCl_4 structure 2.3 \AA above the surface. The Pt-Pt bond distance for the central Pt atom is 3.34 \AA , which is a 24 % increase with respect to the bulk. This supports the idea of an adsorbed PtCl_4 unit as opposed to four chlorine atoms adsorbed around a Pt ad-atom.

The defects seen in the left part of Fig. 3.13 are due to Pt defect atoms which have popped out of the substrate to form the PtCl_4 pentamers. This does not happen for the case of pure Br adsorption and demonstrates the higher corrosive potential of Cl in agreement with the DFT calculations. The energy gain from bonding a Cl atom to the excess Pt atom is comparable to the energy cost of forming a Pt surface defect. In contrast, for Br an energy deficit of about 1 eV is found. From a comparison of the unoccupied to the total LDOS around the adsorbed PtCl_4 cluster one obtains an estimate of about 3.1 electron holes with respect to a Pt d^{10} (Cl

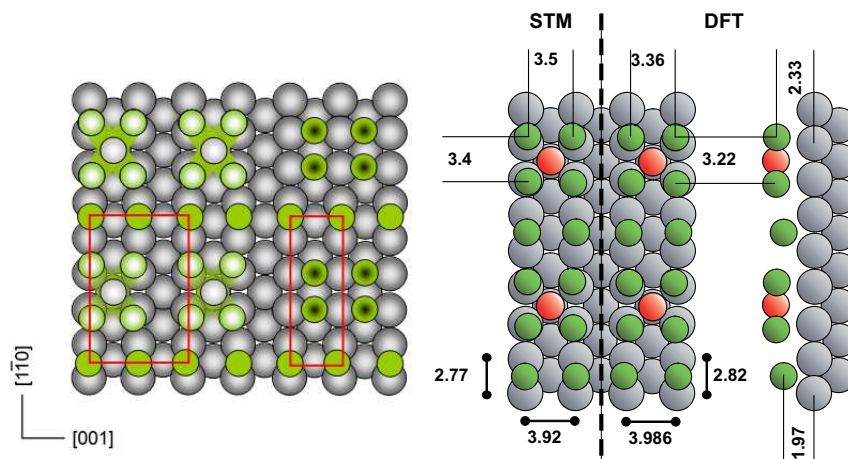


Figure 3.15: Left: comparison of the (4×1) and (4×2) Cl/Pt phases. Right: Ball model of the (4×2) -PtCl₄/Cl/Pt(110) adsorbate system. Gray balls are Pt substrate atoms, green balls Cl atoms and red balls the central Pt atom of the PtCl₄ pentamers. The vertical dashed line separates the experimental STM from calculated DFT (VASP-GGA) results. On the lower left and right the dimensions of the Pt surface unit cell are given, while on the upper left and right the distances between the Cl atoms in the PtCl₄ clusters are designated. In the side view far right the vertical distances between the Cl atoms, respectively the PtCl₄ clusters, and the Pt substrate are given. Almost no buckling (< 0.02 Å) is found both for the PtCl₄ and the surface Pt layer. A larger buckling (0.2 Å) appears in the second Pt layer. The difference between the experimental and the DFT-calculated substrate lattice constant must be considered. All distances are given in Å.

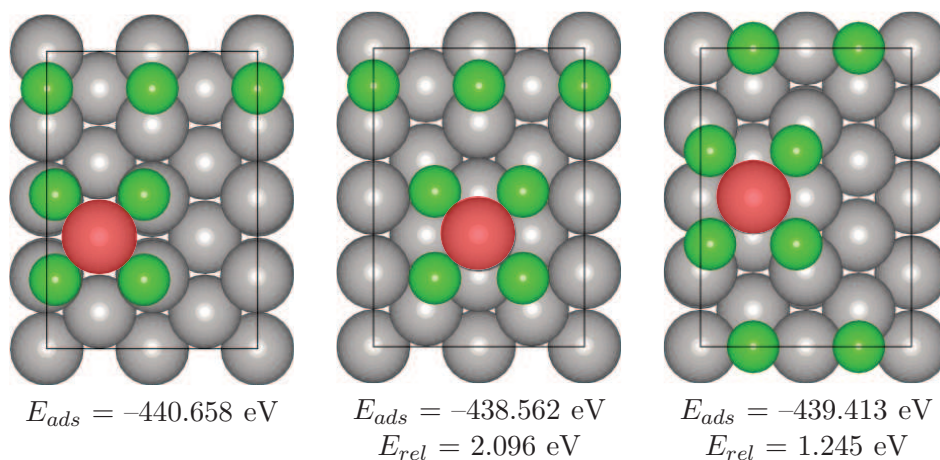


Figure 3.16: Absolute and relative energies per cell of various arrangements with (4×2) periodicity. The substrate Pt atoms are grey, Cl atoms are green, the protruding Pt atom is highlighted in red.

$3p^6$) configuration, while the free tetrachloroplatinate complex $[\text{PtCl}_4]^{2-}$ has two holes. Thus it appears again more appropriate to describe the adsorbed complex as a $[\text{PtCl}_4]^{2-}$ molecule where the additional hole is due to the binding of the Cl atoms to the substrate.

3.2.4 Cl Adsorption on $c(2 \times 2)$ -Br/Pt(110)

Hardly surprising, the same $c(2 \times 2) \implies (3 \times 1)$ phase transition described for pure Br and Cl adsorption has been observed also by dosing Cl on the $c(2 \times 2)$ -Br/Pt(110) (total coverage: $1/2 \text{ ML Br} + 0.16 \text{ ML Cl}$). At room temperature the contrast in STM images strongly depends on the tunnelling parameters and particularly on the sign of the bias voltage (Fig. 3.18). For negative bias (full states) two kind of rows are recognised along the $[001]$ direction, as seen in figure 3.18: one row-type (A for convenience) is well atomically resolved, while the other one (B-type) looks much more blurred and slightly less intense. For positive bias voltages instead (empty states), all the atoms are equally intense and equally well resolved and no

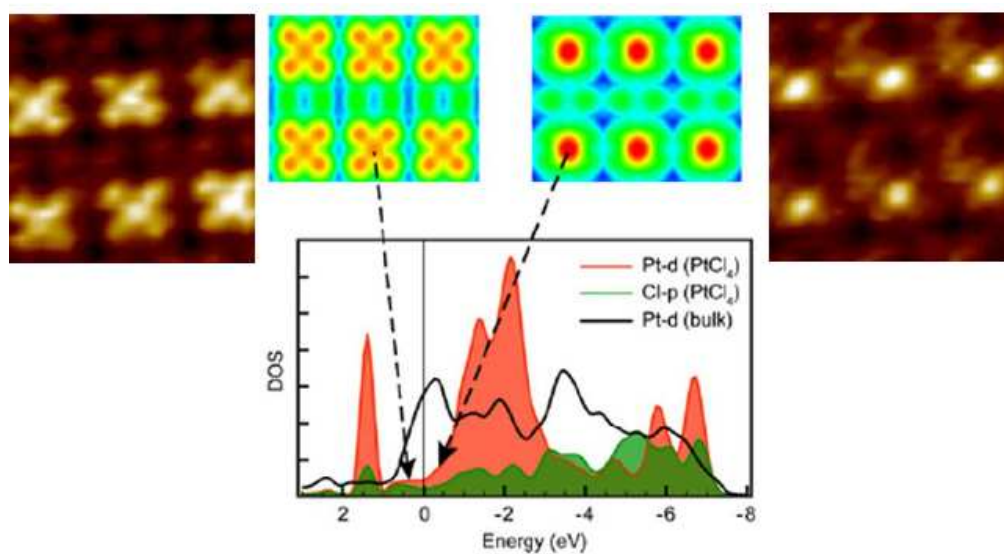


Figure 3.17: On top: RT-STM empty-states (left) and full-states (right) images of $(4 \times 2)\text{-PtCl}_4/\text{Cl}/\text{Pt}(110)$ (0.48 V, 0.34 nA). The middle panels show simulated STM images and the bottom panel the LDOS for the adsorbed PtCl_4 unit compared with bulk Pt.

unresolved continuous rows can be seen parallel to the [001] direction. The surface is described in both cases by a (3×1) unit cell.

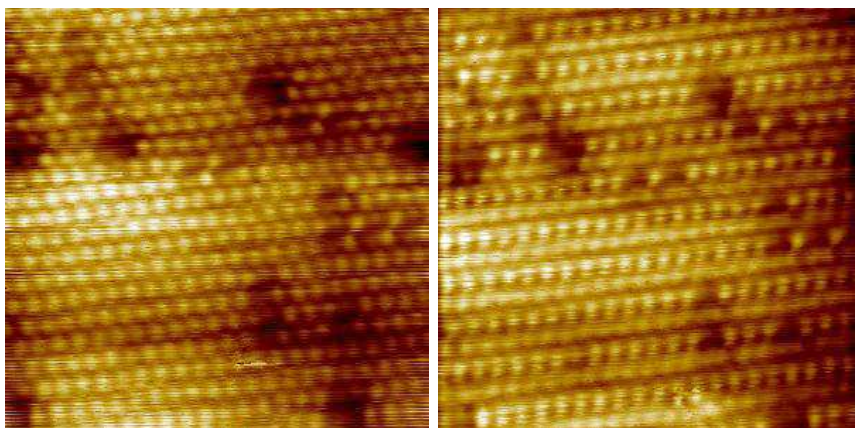


Figure 3.18: RT-STM: (3×1) -ClBr/Pt(110). Left: 0.46 V, 0.17 nA. Right: -0.46 V, 0.17 nA. [52]

Upon cooling to 110 K, a different surface structure appears, looking now the same for positive and negative bias voltages (Fig. 3.19). The system is still characterised by two different kind of rows: while one type (α for convenience) looks homogeneous (i. e. equally bright) and less well resolved, the other one (β) is better resolved and characterised by brighter and darker protrusions. Assuming that each protrusion corresponds to an atom, the α -type chains must be formed by Br, since they account for a coverage of $\sim 1/3$ ML. β -type chains have to be instead formed by both Br and Cl atoms. It seems logical to assume that the brighter protrusions are Br atoms because the covalent radius of Br is bigger and because the brighter spots are more similar to the ones on the α -type chains and because Br has a bigger covalent radius than Cl. The darker protrusion must then correspond to the Cl atoms. This assumption is confirmed by DFT (see below).

Due to the total coverage of $2/3$ ML, it is evident that Br must occupy both SB and LB sites. If one examines the low temperature experimental data and assumes

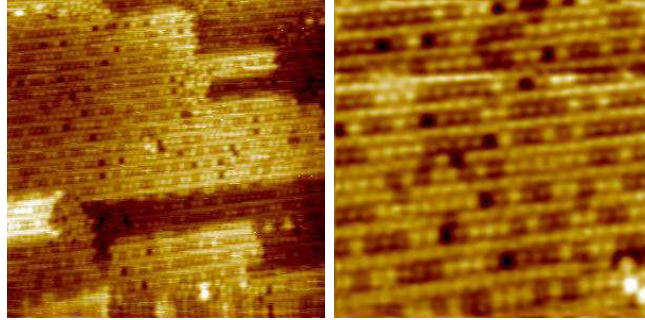


Figure 3.19: LT-STM ($\sim 110\text{K}$): $(3\times 1)\text{-ClBr/Pt}(110)$. Left: 0.27 V , 0.34 nA . Right: -0.34 V , 0.31 nA . [52]

that the darker protrusions are Cl atoms, one has to conclude that Br atoms on SB and LB sites look identical, at variance with the $(3\times 1)\text{-Br/Pt}$ structure. In this latter structure the buckling of the substrate reduces the height difference between SB and LB Br atoms, but does not completely compensate it. It appears that in the present case of a mixed $(3\times 1)\text{-BrCl/Pt}$ system, the buckling is so strong that the height difference between Br atoms in SB and LB sites, respectively, is essentially eliminated. If this explanation is correct, the buckling can not be due to a local Br-Pt bonding interaction, but has to be a collective effect, which is globally enhanced by the presence of the Cl atoms.

As regards the adsorption site of Cl, it can not be determined on the basis of STM pictures only. Although it can be safely stated that Cl must occupy only one type of site, both LB and SB are compatible with the experimental data. A DFT treatment of the problem is also not straightforward. The results are shown in figure 3.20: The Cl on $c(2\times 2)\text{-Br/Pt}(110)$ system was simulated with a (3×2) unit cell with all possible coverages between $\Theta_{Br} = 2/3\text{ ML}$, $\Theta_{Cl} = 0$ (Fig 3.20a) and $\Theta_{Br} = 1/3\text{ ML}$, $\Theta_{Cl} = 1/3\text{ ML}$ (Fig 3.20d, 3.20e). Quite unexpectedly, the arrangement c appears more stable than the corresponding ordering b. This means that a theoretical phase with Br atoms on SB and alternating Br and Cl atoms on

LB would more stable than an ordered phase with Br atoms on LB and alternating Br and Cl atoms on SB. But if Cl–Br phase separation is taken into account, the result is inverted: A phase composed by pure Br domains (Fig 3.20a) and domains with all Br atoms on LB and all Cl atoms on SB (Fig 3.20e), is favoured over the theoretical alternating c-arrangement. A confirmation of this separation mechanism can be obtained by observing the experimental STM images: darker protrusions (Cl atoms) are seldom isolated. Furthermore, the appearance of the purely Br related rows in [001] direction is very similar to that of the continuous rows in the CO/NO induced (4×1) structures (see chapter 4). It can be therefore concluded that these rows are associated with LB-sites, while the atomically well-resolved rows, which contains both, Br and Cl, are associated with SB sites.

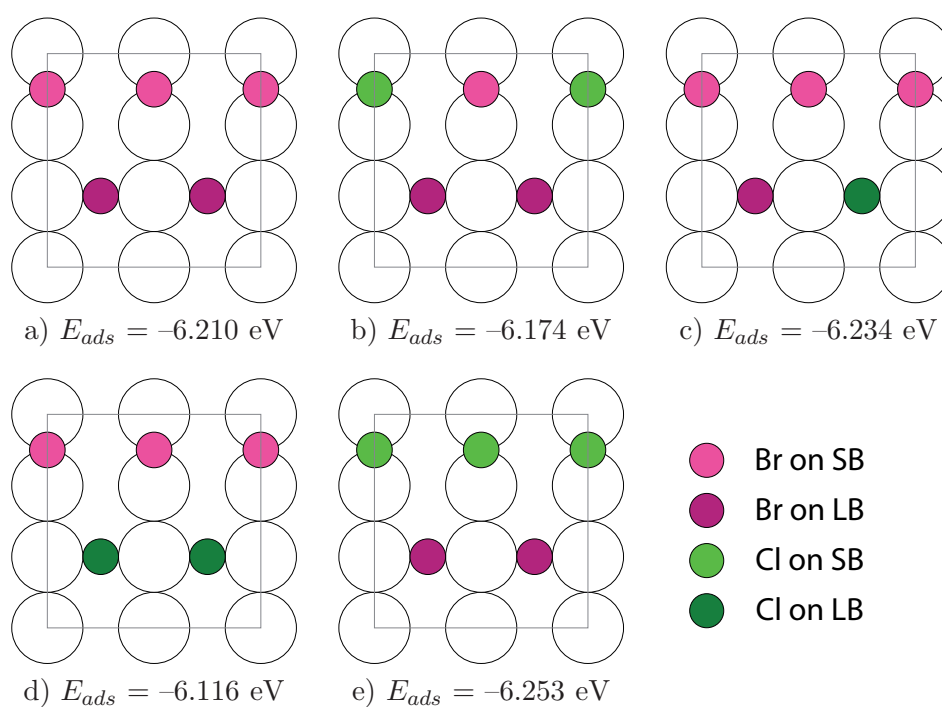


Figure 3.20: Ball scheme for the mixed systems BrCl/Pt(110). The energies are given in eV per cell referred to the halogen molecules.

The STM images obtained for positive bias at room temperature can be again interpreted in terms of a time averaging of mobile atoms: darker and brighter atoms would hop at a fast rate, yielding a time averaged, blurred intensity for the protrusions in the B-type rows, while two types of protrusions become clearly distinguished at low temperature, where the dynamics is frozen. It appears that the darker areas seen in room-temperature images are associated with Cl atoms hopping to neighbouring sites during the sampling time of the STM images. In the darker spots atomic resolution is sometimes not recognisable, suggesting that the Cl mobility is substantially larger.

Chapter 4

Adsorption of CO and NO on Pt(110)

As seen in the previous chapter, a Peierls type mechanism seems to be a candidate in order to explain the unusual order-to-disorder transition upon cooling in the $c(2\times 2)$ -Br/Pt(110) system. In view of this, it is extremely interesting to study the role of adsorbates on the $c(2\times 2)$: they could in fact shift the Fermi surface and trigger similar phase transitions even at higher temperatures. A modulation of the surface geometry induced by a tuning of k_F by means of co-deposition of different adatom species has been proposed by Carpinelli [59], who coined the term Fermi Surface engineering, as an elegant way to produce different two-dimensional commensurate or incommensurate phases on a surface [60, 61].

By adsorption of CO or NO on $c(2\times 2)$ -Br/Pt(110) different phases are indeed observed as a function of the adsorbate coverage. So far however it is not completely clear, whether the various phases are actually driven by a Peierls instability.

4.1 CO and NO Adsorption on a Clean Pt(110) Surface

CO and NO are chemically and geometrically quite similar. Though, NO has an additional unpaired electron, such that similarities as well as differences between

the systems CO/Pt(110) and NO/Pt(110) may be expected on a microscopic level. Both molecules are experimentally known to lift the MR reconstruction at room temperature. Below 250 K, though, the MR ordering is “frozen” and can not be broken by CO (NO) adsorption. [62, 63]

The high symmetry positions on the MR surface considered in the present adsorption study are defined in figure 4.1. The adsorption sites on the (1×1) surface are the same as described in chapter 2.

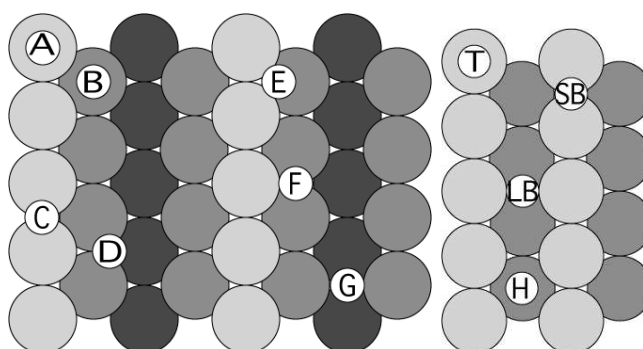


Figure 4.1: Adsorption sites on the MR surface: A is a Top site on a Pt atom of the close-packed rows, B a top position on a Pt atom of the second (first complete) layer, C is a SB site on a CP row, D a SB site between two atoms of the second Pt layer, E and F are nonequivalent 3-fold coordinated hollow positions on the (111) facets, respectively between 2 Pt atom of the first and 1 of the second layer and 1 atom of the first and 2 of the second Pt layer, G is a LB site in the groove. The adsorption sites on the unreconstructed (1×1) surface are described in chapter 2

The calculated adsorption energies and bondlengths are reported in table 4.1. CO is experimentally observed to adsorb on T sites on both the (1×1) and the MR-reconstructed surface (Site A in Fig. 4.1) at low coverages. At CO coverages higher than $\simeq 0.2$ ML on MR also short bridge C sites are occupied [63]. NO adsorbs on SB sites on the (1×1) surface and on short bridge C and D sites on MR [64].

In figure 4.2 the adsorption energies of CO and NO are compared with the already known, corresponding results for Br. It should be noticed that the preference

Site	CO			NO		
	E_{ads} (eV)	d_{CPt} (Å)	d_{CO} (Å)	E_{ads} (eV)	d_{NPt} (Å)	d_{NO} (Å)
A	1.896	1.855	1.159	1.685	1.814	1.173
				1.621	1.822	1.192
B	1.490	1.869	1.161	0.889	1.843	1.171
				0.657	—	—
C	1.913	2.015	1.181	2.113	1.977	1.200
				2.175	1.978	1.216
D	1.697	2.105	1.192	1.763	2.103	1.210
				1.717	2.075	1.210
E	1.754	2.096	1.193	1.937	2.088	1.213
				2.153	1.981	1.215
F	1.420	1.914	1.168	1.324	1.946	1.182
				1.376	1.938	1.198
G	1.611	2.034	1.187	1.669	2.030	1.196
				1.655	2.029	1.211

Table 4.1: Adsorption energies and bondlengths for 1/4 ML CO (NO) adsorption on Pt(110). The adsorption energies are referred to the CO (NO) molecule and the clean MR-(1×2) (8 complete layers plus one semilayer) surface. For NO the experimental values are given under the calculated ones [65]. For comparison see [64]

of SB over LB sites is much stronger for CO (NO) than for Br.

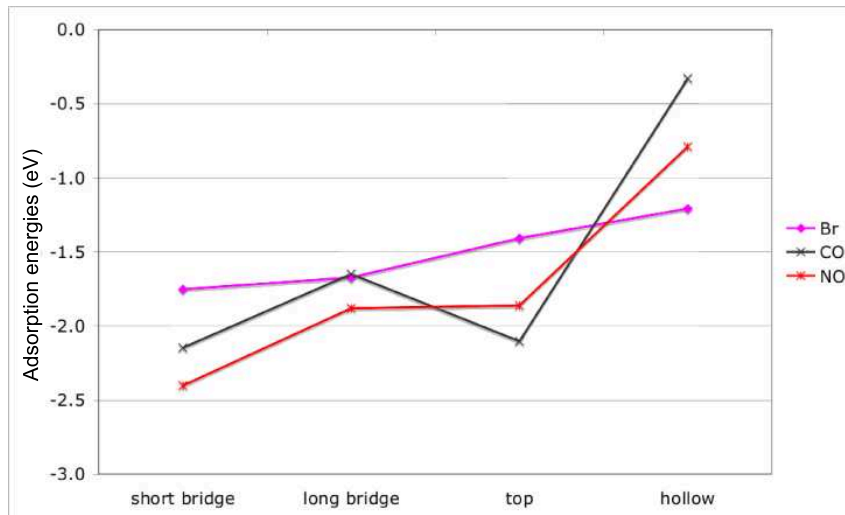


Figure 4.2: CO(NO) vs. Br

The “normal” diffusion energy barrier of an adsorbate species across a homogeneous surface can be described by a simple sine-like function with single hops from one stable high symmetry site to the next, as in the case of Br. CO and NO are more complicated: For CO, both A (top on row) and C (short bridge on row) sites are local minima and the barrier lies in between. Important details can be overlooked unless a fine grid is used for the calculation of the barrier. The adsorption energy was calculated on 9 points equally spaced on the line between both minima. The C (respectively N, Br) atom is relaxed only in the z direction, normal to the surface, no constraint is applied to the other atoms. The results are shown in figure 4.3. While the adsorption potential of Br has a “classical” sinusoidal trend with a minimum on C and a maximum on A, CO shows a double parabola, narrower about C and broader about A site. The barrier for NO seems to be a superposition of both. The barrier between neighbouring close-packed rows is much higher, particularly in the case of CO, than the barrier for diffusion along the rows. Diffusion is therefore

highly anisotropic on the (110) surface.

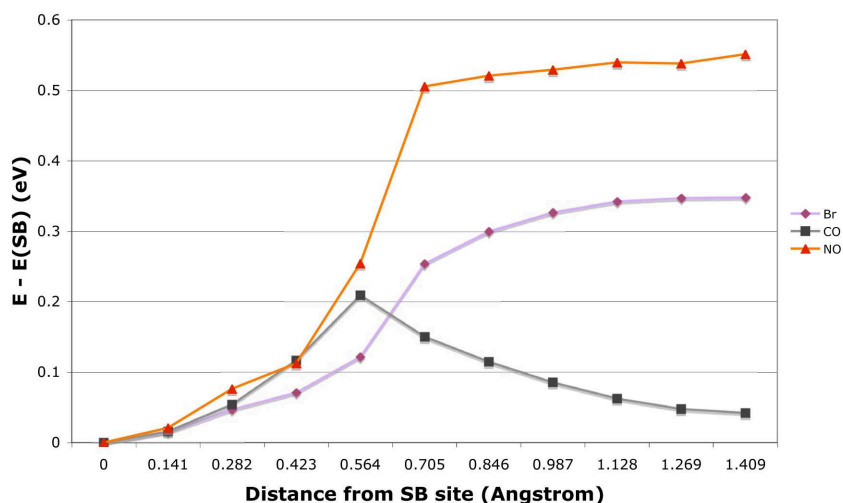


Figure 4.3: Diffusion barriers for CO, NO and Br along the upmost rows of the MR-Pt(110) surface.

The experimental observation, that CO adsorbs preferentially on top (A) sites and that SB (C) sites are occupied only at coverages higher than over 0.2 ML, appears in contradiction with the calculations, which provide almost the same adsorption potential for T (A) and SB (C) sites with even a small preference for the latter. A more accurate analysis of the adsorption energies allowed to determine that the preference for C over A adsorption sites on the MR surface is probably an artefact of the slab geometry. In fact, the energy difference depends slightly on the numerical set-up, particularly on the number of Pt layers in the slab. As shown in figure 4.4, the energy difference has a minimum for 9 layers, that is the thickness of the slab used in the present work. In the limit for thick slabs the top site is slightly preferred.

However, this slight preference for A sites on MR is too small to answer for the strong preference for A sites, and on the non-reconstructed (1×1) surface the

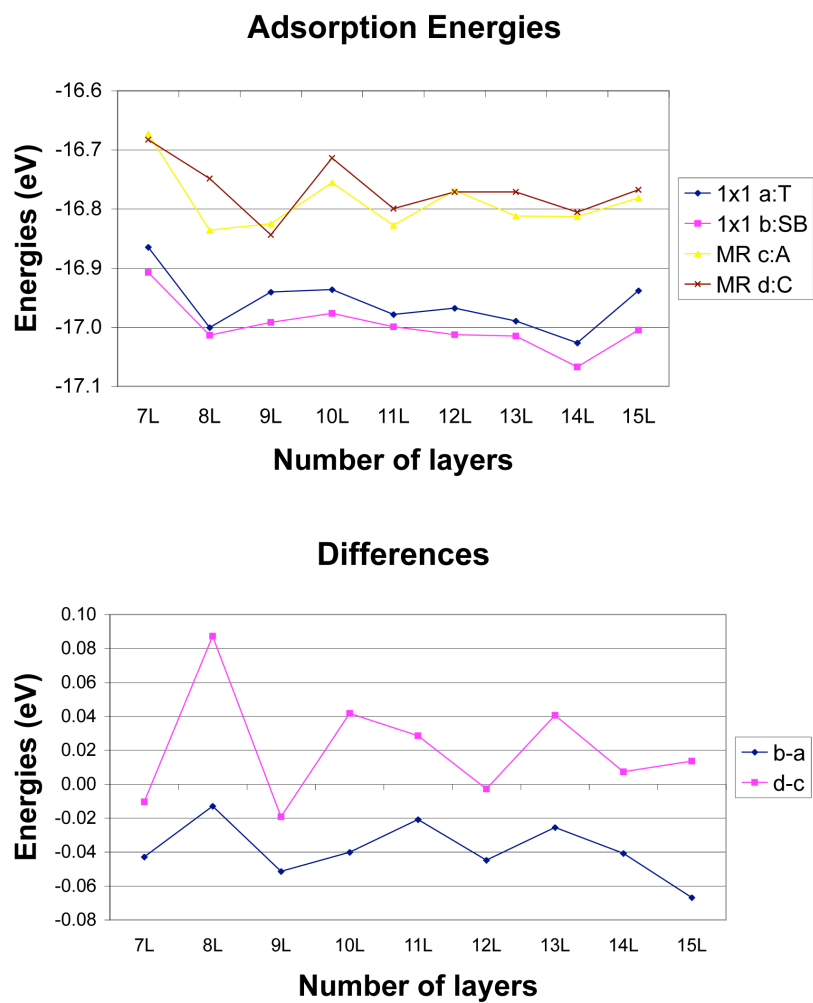


Figure 4.4: Difference (lower panel) between the adsorption energy (upper panel) on short bridge (C) and top (A) sites.

SB adsorption site is always preferred on T, independently of the thickness of the slab. An answer is suggested by Q. Ge and D. a. King [64]: The vibrational entropy contributions from the low frequency hindered translational modes on the atop site along dominate the total adsorbate entropy, yielding an entropy difference between short bridge and top position that stabilises the latter. On the other hand, GGA(LDA) also fails on Pt(111) to predict the occupation of the T site as found in experiment [60]. A solution of this problem might be a better description of the HOMO-LUMO gap in CO as pointed out by Kresse [66]

4.2 Mixed Adsorption CO (NO) with Br

As in the case of pure halogen adsorption, an analysis of the first neighbours interactions in ideal, non-physical systems gives important clues about the interpretation of the real adsorption process. The considered system consists of a (2×2) unit cell with an halogen atom adsorbed on a SB site. An additional CO (NO) molecule can occupy just one of the three remaining SB sites. Depending on the adsorption site a $c(2 \times 2)$, a $p(1 \times 2)$ or a $p(2 \times 1)$ arrangement results (see Fig. 4.5).

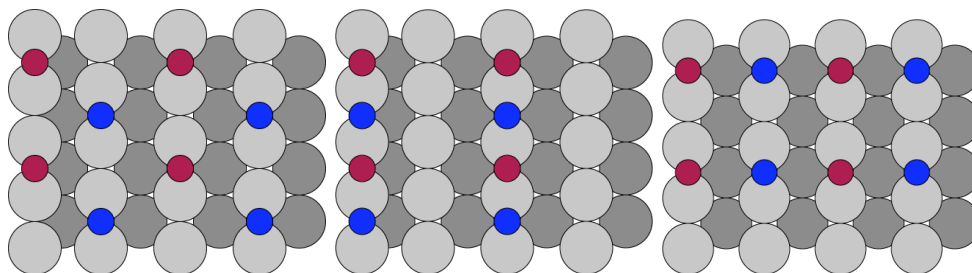


Figure 4.5: Br–CO (NO) interactions: Adsorption arrangements with 1/2 ML total coverage

In the first case the interaction between the halogen atom and the CO (NO) molecule is negligible, in the second case next neighbouring adsorbates are bound to one same Pt atom, thus both a direct and a strong substrate-mediated interaction

occurs, in the third case the next neighbouring adsorbates are not bound to the same Pt atoms, thus just a weak substrate mediated interaction (surface deformation, second neighbour interaction) is possible. The results are shown in figure 4.6

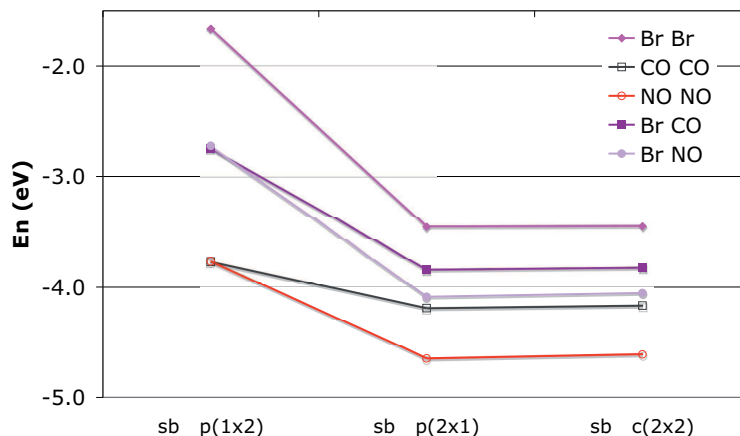


Figure 4.6: CO (NO)–Br adsorbate–adsorbate interactions. The energies are given per (2×2) cell and referred to the isolated Br and CO (NO) molecules.

As in the case of Cl, the next-neighbour interaction in $[001]$ direction stabilises the $p(2\times 1)$ over the $c(2\times 2)$ arrangement, while the direct interaction in $[1\bar{1}0]$ direction has repulsive nature. This repulsion, however, is much weaker (ca. 300 meV for NO and 450 eV for CO) than in the pure-halogen case, which allows the occupation of next neighbouring adsorption sites.

4.3 CO, NO adsorption on the $c(2\times 2)$ -Br/Pt(110) Surface

The adsorption of CO or NO causes the $c(2\times 2)$ -Br/Pt(110) surface to undergo a series of phase transition including a (3×1) and a (4×1) phase. These phase transitions are here treated in detail and similarities as well as differences from the pure Br phases are pointed out.

4.3.1 Experimental Evidence

Most experimental data cited here were taken by C. Deisl and E. Donà at the University of Innsbruck [28, 52]. CO and NO adsorb molecularly on $c(2\times 2)$ -Br/Pt(110), just as on the clean Pt(110) surface, with a saturation coverage at 120 K of one monolayer for both gases. At room temperature, the saturation coverage is $1/4$ ML for NO and ~ 0.4 ML for CO [67, 68].

$c(2\times 2) \Rightarrow (3\times 1)$ Transition

In the coverage range up to $1/4$ ML CO or NO on the $c(2\times 2)$ surface, three global well ordered phases form: One with (3×1) , one with (7×1) and one with (4×1) periodicity. The observed phases are almost identical for both molecules. The CO (NO) induced $c(2\times 2) \Rightarrow (3\times 1)$ transition and the global (3×1) structure will be described first [28, 52].

The system CO on $c(2\times 2)$ -Br/Pt(110) was analysed by LEED by monitoring the sample during CO adsorption (10^{-8} mbar, \sim RT). The evolution of the surface is shown in figure 4.7.

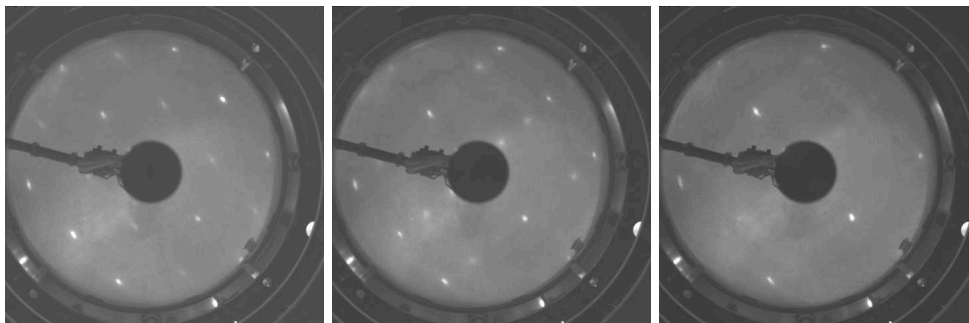


Figure 4.7: LEED pictures (85 eV) of the clean $c(2\times 2)$ -Br/Pt(110) (left), after exposure to $150\text{ s}/10^{-8}$ mbar CO (centre), after $1250\text{ s}/10^{-8}$ mbar CO (right) The $c(2\times 2)$ LEED pattern transforms abruptly into a (3×1) after an exposure of 1.5 L. The phase transition is reported to take place suddenly, no continuous movement of the LEED spots is observed, as would be expected in the case of a compression structure [52].

Figure 4.8 shows a series of STM images, taken during the dosing of CO. Starting from a well ordered $c(2\times 2)$ phase. One observes that the ordering of the surface is destroyed already after adsorption of very little quantities of CO, in the order of magnitude of ~ 0.04 ML [28] (Figure 4.8b).

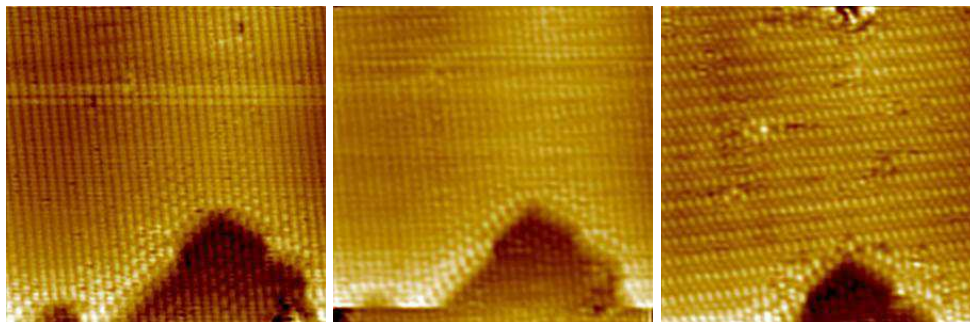


Figure 4.8: RT-STM image of “clean” $c(2\times 2)$ -Br/Pt(110) (left), after 0.2 L of CO (centre), and after 1 L (right). $170\times 170 \text{ \AA}^2$, 0.15 V, 0.3 nA [52].

Starting from a CO coverage of ~ 0.06 ML, a (3×1) structure can be recognised both, with LEED and STM. This (3×1) arrangement is resolved in STM from the beginning as a global phase, also LEED describes the transformation as abrupt (s. Fig. 4.7). The (3×1) phase, as estimated by LEED, is best ordered for a coverage in the order of magnitude of ~ 0.12 ML CO (NO). In the atomically resolved STM picture (Fig. 4.8c) the (3×1) unity cells with Br atoms on long and short bridge sites can be clearly recognised. The corrugation is very similar to the (3×1) -Br phase with $2/3$ ML Br.

Low-temperature STM experiments were performed to clarify the structure of this phase. For 1 L of CO dosed at 110 K, (3×1) domains appear together with residual $c(2\times 2)$ and disordered regions.

The behaviour of NO is very similar to CO, as shown in Fig. 4.10. During the adsorption of NO on the $c(2\times 2)$ -Br/Pt(110) surface at RT, first an apparent (1×1) phase is observed, again indicating fluctuations in the adlayer, then a 3-fold

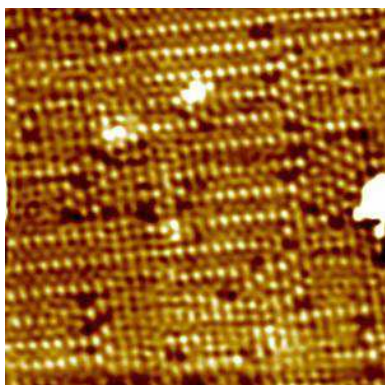


Figure 4.9: LT-STM image (110 K) of CO on $c(2\times 2)$ -Br/Pt(110) ($150\times 150 \text{ \AA}^2$, 0.3 V, 0.1 nA). (3×1) domains with a local coverage $\Theta_{Br} = 2/3 \text{ ML}$ coexist with disordered regions with lower local coverage. The global Br-coverage is $1/2 \text{ ML}$ [52].

periodicity appears in the $[1\bar{1}0]$ direction, developing finally into a well ordered (3×1) structure, indistinguishable from the (3×1) obtained for $\Theta_{Br} = 2/3 \text{ ML}$. The LEED $I(E)$ spectra of the NO-induced (3×1) structure are very similar to the ones obtained for the pure Br (3×1) phase. As in the Br-induced transition, the intensity of the integral spots can be represented as a superposition of the $c(2\times 2)$ and pure-Br (3×1) phases. Also the $1/3$ integer spots show the same spectral dependency as the Br- (3×1) phase. In the last image of figure 4.10, the NO-Br (3×1) phase is already saturated, and the formation of stripes with 4-fold periodicity can be observed, which are typical for higher NO coverages (s. above). The NO-Br (3×1) phase, at least under saturation, appears less well-defined than the corresponding CO-Br phase.

$(3\times 1) \Rightarrow (4\times 1)$ Transition

Increasing the CO (NO) coverage above $\simeq 0.12$ monolayer, the (3×1) phase is gradually destroyed. In LEED a continuous movement of the fractional spots is observed for higher CO coverage and a weak (4×1) pattern forms after an exposure of about 12 L (Fig. 4.7, right).

STM shows first the formation in the (3×1) phase, of stripes elongated in the $[001]$ direction with a width (in the $[0\bar{0}1]$ direction) of two next-neighbour distances with either a “linear” or a “zigzag” ordering. These stripes are always coupled to

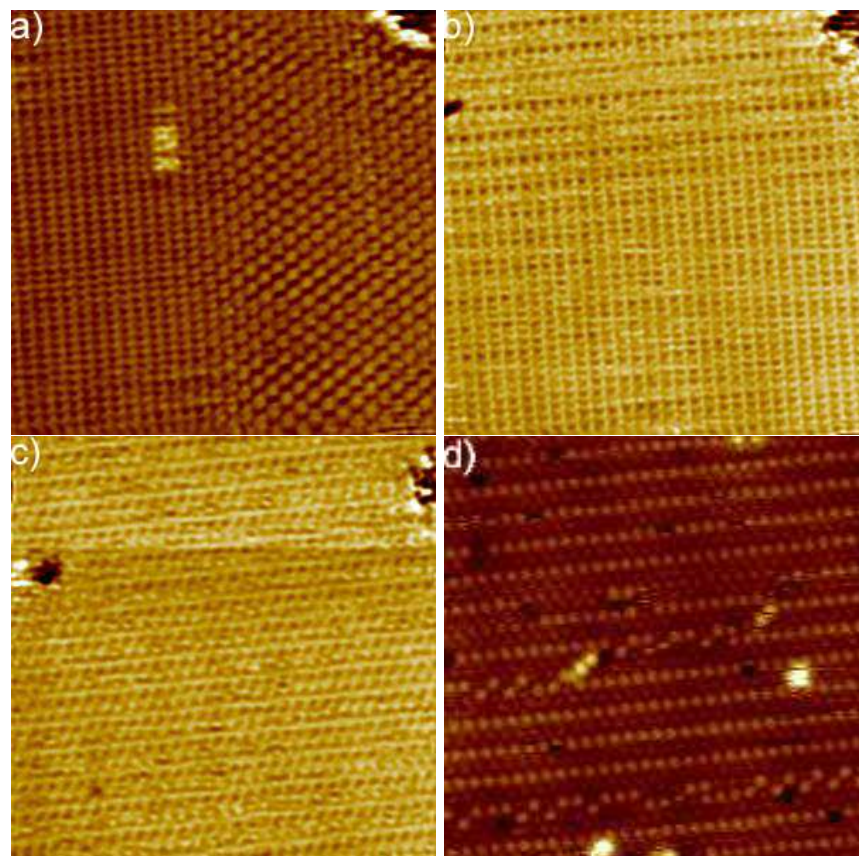


Figure 4.10: Series of STM images acquired during the adsorption of NO on the c(2×2)-Br/Pt(110) at room temperature ($150 \times 150 \text{ \AA}^2$, 0.16 V, 0.36 nA). a) clean c(2×2)-Br/Pt(110) surface; b) $\sim 1 \text{ L}$ NO; c) $\sim 5 \text{ L}$; d) $\sim 10 \text{ L}$. All the four pictures reproduce the scanning of exactly the same region [52].

[001]-lines on both sides for a total width of four next neighbour distances, and preferentially arranged in “zigzag” chains (Fig. 4.11). Theoretically, a perfect “zigzag” structure has a (4×2) periodicity. Since the “zigzag” chains have a finite domain length in [001] direction, with random phase slips between them, they do not lead to a doubling of periodicity in LEED in [001] direction. Thus both, the “parallel-linear” and the “zigzag” chains are referred to as (4×1) structure elements in the following.

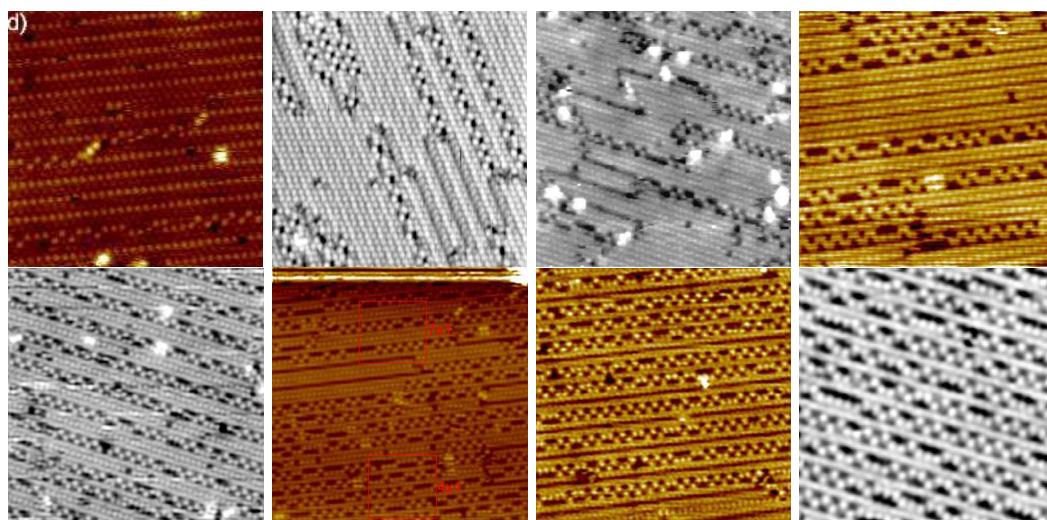


Figure 4.11: Room-temperature STM images showing the transition from a (3×1) to a (4×1) phase. On the left image ($150\times 150 \text{ \AA}$, 0.41 V, 0.35 nA) stripes with (4×1) are formed in the [001] direction. For higher CO exposure domains with (4×1) and (7×1) geometry arise ($240\times 240 \text{ \AA}$, 0.47 V, 0.22 nA). Finally a global (4×1) appears ($120\times 120 \text{ \AA}$, 0.47 V, 0.22 nA).

The formation of the (4×1) stripes causes the global (3×1) ordering to decay in a 2D array of (3×1) antiphase domains. Each (4×1) stripe corresponds to a phase slip of $2\pi/3$ between the bordering (3×1) domains. At low CO (NO) coverage, when the population of CO (NO) is too low to cover the entire phase borders, “naked” solitons (mismatches in the Br adlayer ordering) form too, which are not decorated

by CO (NO). The (4×1) stripes can be thus considered as “dressed” (i.e. decorated with CO (NO)) solitons. Two types of naked solitons exist: α type which induces the

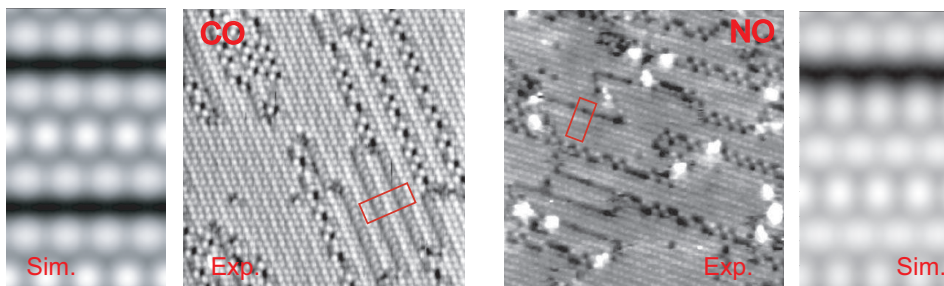


Figure 4.12: The (3×1) phase is transformed into an array of (3×1) antiphase domains, separated either by (4×1) stripes or by single (right: experimental and DFT-simulated image, preferred for NO) or double (left: DFT-simulated and experimental image, preferred for CO) lines of empty sites (soliton lattice)

same phase slip of $2/3\pi$ as a dressed soliton, and β type, which constitutes a phase slip of just $1/3\pi$ and must be doubled to carry the phase slip of a dressed soliton (s. Fig. 4.12). Increasing the CO (NO) coverage, the dressed solitons become longer, until an alternate (3×1), (4×1) and naked-soliton phase is formed, which is periodic in the [001] and random in the $[1\bar{1}0]$ direction (Fig 4.11d). For higher CO (NO) coverage, the portion of surface covered by the (4×1) stripes increases at the costs of the (3×1) phase, until the (3×1) and (4×1) phases are equally widespread and appear alternating, so that a (7×1) phase is observed (Fig 4.11e). A further increase of the CO (NO) coverage causes the breaking of the remaining (3×1) stripes, the increasing of the (4×1) phase (preferably for CO, Fig. 4.11f) and the formation of β -type solitons (preferably for NO, Fig. 4.11g). For NO, an alternate (4×1)-soliton phase is observed, with a total (6×1) periodicity.

Eventually, at a coverage of $1/4$ ML CO (NO), an ordered (4×1) phase forms, where “zigzag” and “linear” arrangement coexist, with a clear preference for the former (Fig. 4.11h).

4.3.2 Discussion

The determination of the CO (NO) coverage in the observed systems is particularly difficult, in [52] the coverage of the observed phases is not quantified, and only exposure values are given, in [28, 68, 55] the coverages are estimated, but the values given differ considerably from one publication to another, which suggests, that the experimental uncertainties in the coverages are quite high. Due to this fact, the interpretation of STM data for the CO(NO)-induced (3×1) phase is nontrivial. The corrugation looks in fact very similar to that for the (3×1) phase with $\Theta_{Br} \simeq 2/3$ ML where each protrusion represents a Br atom (see chapter 3). In the case of the CO-induced (3×1) the total (Br + CO) coverage is just above $1/2$ ML, and a simple interpretation of protrusions in terms of Br atoms is obviously out of discussion. The occupation of the adsorption sites must be statistical: A model of the formation of the (3×1) -CO(NO)/Br must take the following points into account:

- CO (NO) has a strong (CO: 497 meV, NO: 523 meV) preference for SB over LB adsorption sites, much stronger than Br (81 meV, see chapter 2).
- The CO (NO)–Br next-neighbour repulsion in the $[1\bar{1}0]$ direction (CO: 210 meV, NO: 440 meV) is much lower than in the Br–Br case, but strong enough to promote a Br adatom to from short to long bridge

$c(2 \times 2) \Rightarrow (3 \times 1)$ Transition

CO (NO) adsorbs on SB, between four Br atoms. The next-neighbour repulsion pushes Br atoms away on the same close-packed row and breaks the $c(2 \times 2)$ ordering. The surface fluctuates and a global disorder is observed on time average. As more CO (NO) is adsorbed, more Br atoms are pushed to LB adsorption sites, thus spots of a quasi- (3×2) phase nucleate. These (3×2) domains, still surrounded by the remaining (partially disordered) $c(2 \times 2)$ phase, have a coverage slightly higher

than $1/2$ ML, which answers the increased total coverage. This is possible because LB–LB repulsion is much lower than SB–SB repulsion, and thus the (3×2) is more “compressible” than the $c(2\times 2)$ phase. Br atoms on LB are also quite mobile in the $[001]$ direction and both STM and LEED see a (3×1) phase. Furthermore, because of the mobility of CO (NO) and the above $1/2$ ML coverage, the (3×2) domains are not stable, they may propagate across the surface as compression waves without long-range matter transport. However, at room temperature these fluctuations are too fast to be observed by STM and a time average is observed where the (3×2) component prevails, so an apparent global (3×1) phase is observed. At 110 K the compression fluctuations are frozen, and a disordered array of apparent (3×1) , $c(2\times 2)$ and $p(2\times 1)$ domains is observed (Fig. 4.9). A similar explanation was proposed by C. Deisl [28], already before the introduction of a compressible (3×2) phase. He therefore interpreted the apparent (3×1) domains as true CDW stabilised (3×1) domains with $2/3$ ML coverage, and postulated that the remaining phase must be somehow emptied under $1/2$ ML to respond to the total coverage.

However, the possibility that the (3×2) - (3×1) domains are stabilised by an interaction with a CDW can not be either proved or ruled out by means of DFT.

$(3\times 1) \Rightarrow (4\times 1)$ Transition

The $(3\times 1) \Rightarrow (4\times 1)$ phase transition is characterised by the formation of (4×1) stripes: The same periodicity as observed for pure Br adsorption. The NO(CO)/Br- (4×1) structures appear to be very similar to the (4×1) phase observed for pure Br and described in the previous chapter, but they are in fact quite different. For pure Br, a delicate energy trade-off between adsorption potential and repulsion promotes Br-atoms to LB sites (s. Pag. 59) leading to one atom on SB and two on LB site per unit cell. Present DFT calculations, however, yield a clear preference of CO and NO for the short-bridge sites. This implies that the continuous rows running

along the [001] direction in the (4×1) -CO(NO)/Br structure correspond to Br in LB-sites. The (4×1) unit cell is then inverted, with respect to the pure (4×1) -Br/Pt structure. Whereas in the pure Br structure there is one occupied SB- and two occupied LB-sites per unit cell (Fig. 3.9), the mixed (4×1) -CO(NO)/Br structure features one Br-occupied LB-site and two SB-sites, which can be occupied by either Br or CO (NO).

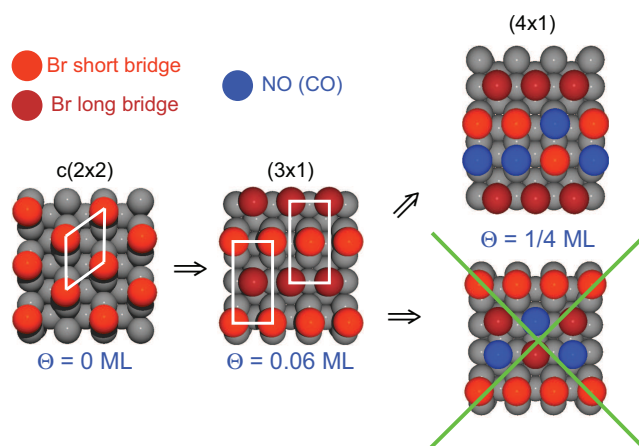


Figure 4.13: The preference of NO (CO) for SB adsorption sites is much stronger and the next neighbour repulsion much weaker than for Br. For NO (CO) the energy trade-off is not sufficient to make it adsorb on LB sites, in contrast to Br. The arrangement with CO (NO) on SB is preferred by 1.17 eV (1.09 eV) per (4×2) cell.

In order to evaluate the adsorption energy difference between the (3×1) and the (4×1) domains, both global phases are simulated. The calculation shows a slight preference for the higher covered (4×1) phase, the results are listed in table 4.2.

This means that the stoichiometric global coverage $2/3$ ML ($1/2$ ML Br + $1/6$ ML CO or NO) of the (3×1) Br-CO(NO) phase can not be reached. The observed (3×1) phase consists of fluctuating $1/2$ ML (3×2) and $2/3$ ML (3×1) domains. As can be seen in figure 4.14, the (3×2) unit cell is a (3×1) cell with a hole i.e. a free LB adsorption site. Therefore a mixed (3×2) - (3×1) phase can be viewed as a (3×1)

	(3×1)	(4×1)	(4×1) + soliton
Br CO	-1.653 eV +13 meV	-1.666 eV —	-1.634 eV +32 meV
Br NO	-1.707 eV +16 meV	-1.723 eV —	-1.660 eV +63 meV

Table 4.2: Comparison of the (3×1)-phase and (4×1)-phase adsorption energies. Values per adsorbate. The (3×1) phase was calculated both on a (3×2) and on a (6×2) cell, the results are identical to the meV, the (4×1) and the (4×1) + soliton phases are calculated with a (4×2) and (6×2) cell respectively.

phase with holes.

Figure 4.14 presents also a very raw estimation of the density of holes on the surface: The overall adsorption energy per adsorbate at different holes concentrations is calculated as a weighted mean of the (3×2) and (3×1) adsorption energies in order to avoid the use of very large unit cells. The result of this estimation is that the fluctuating (3×1) phase is stable up to a critical coverage between $1/12 \simeq 0.083$ ML and $1/9 \simeq 0.111$ ML. This is lower than the experimentally observed critical coverage value $\Theta_{CO(NO)} \simeq 0.12$ ML, the reason is most probably the crudeness of the estimation. A more accurate evaluation of the adsorption energy of the fluctuating (3×1) phase would be an interesting object for a further research.

Above the critical CO(NO) concentration, the (3×1) phase decays spontaneously in the (4×1) phase. The formation of (4×1)-phase stripes causes the formation of solitons, which represents an energetical cost (see figure 4.15). For this reason the (3×1) \Rightarrow (4×1) phase transition is not as fast as the c(2×2) \Rightarrow (3×1) transition.

The phase observed in Fig. 4.11e can be interpreted as an alternation of (3×1) and (4×1) domains, with a global (7×1) periodicity. As shown in figure 4.16, it is not possible to assign a Br atom to every protrusion observed in STM, because this would imply a Br coverage $\Theta_{Br} = 8/14$ ML, whereas the real coverage is $1/2$ ML.

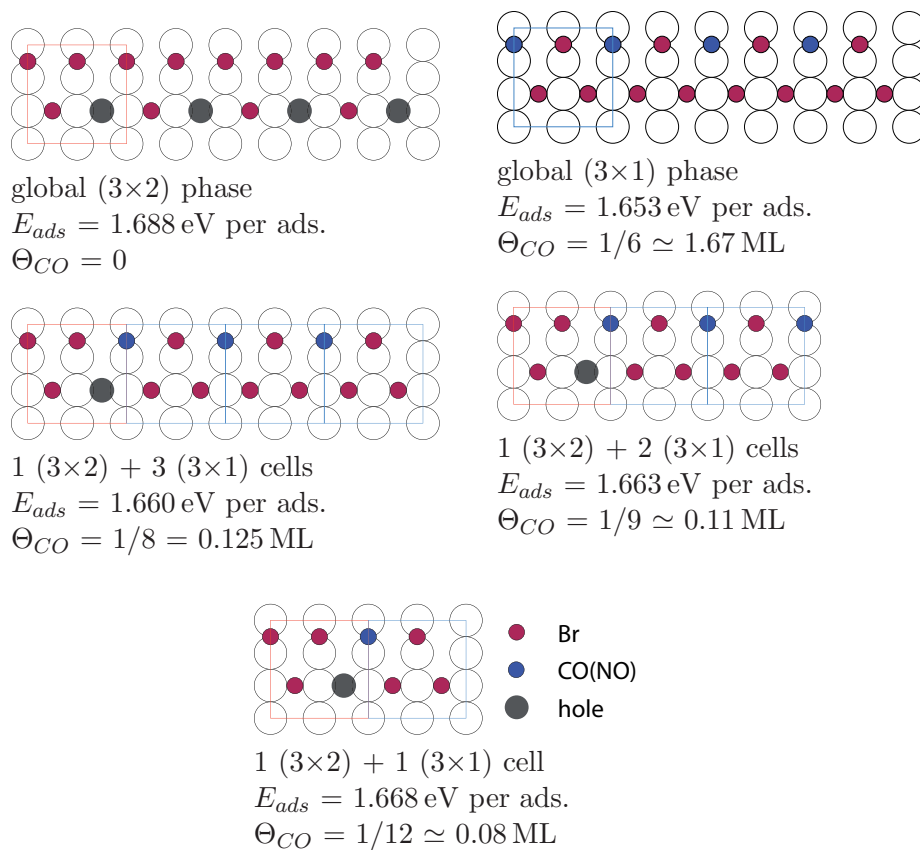


Figure 4.14: Estimation of the CO critical coverage. The energy of a surface supercell is estimated as the sum of the composing (3×2) and (3×1) unit cells.

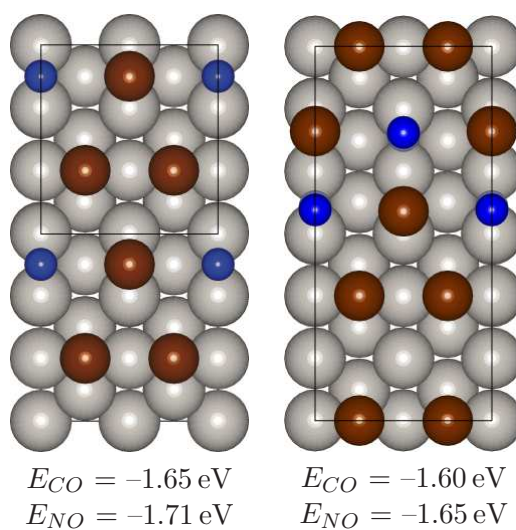
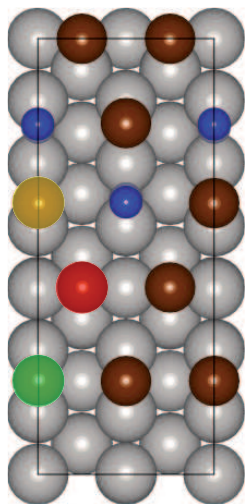


Figure 4.15: Left the global (3×1) Br-CO (NO) phase, right the alternate (4×1)-bare soliton phase. Both phases were simulated on a unit cell with (6×2) periodicity, the energies are given per adsorbate referred to the clean Pt surface and to the isolated Br and CO (NO) molecules. At coverages below $\Theta_{CO(NO)} = 1/4 \text{ ML}$ the formation of dominions of the (4×1) phase causes the formation of bare soliton, which are energetically unfavourable. This phenomenon restrains the decay of the (3×1) in the (4×1) phase.

The global Br coverage can be accounted for by supposing that one Br atom is missing with respect to the nominal coverage.



	Br CO	Br NO
- LB	-15.01	-15.34
- SB (3×1)	-14.46	-14.79
- SB (4×1)	-14.65	-15.02

Figure 4.16: The (7×1) -CO (NO)/Br phase can be interpreted as a regular alternation of (3×1) and (4×1) domains. To answer the real coverage $\Theta_{Br} = 1/2 \text{ ML}$, one Br atom must be missing with respect to the nominal coverage. There are three non equivalent adsorption sites in the unit cell: LB sites (red), SB sites in the (3×1) phase (green) and SB sites in the (4×1) phase (yellow). Simulations show that LB sites are depopulated both for CO and NO adsorption. The energies are given in eV per (7×2) unit cell referred to the clean surface and free molecules.

The remaining (3×1) domains are removed by further CO (NO) adsorption, and bare solitons appear again. For NO a phase with (6×1) periodicity is observed, consisting in (4×1) stripes alternated by bare solitons. In this phase, the “bare” solitons can not be completely empty. Such an arrangement would have the same Br and CO (NO) coverage as the mixed CO (NO)/Br- (3×1) phase. This would be in contradiction both with the present calculations (that predict the (3×1) phase to be more more stable than the (6×1)) and the experiment (the (6×1) phase appears only after further CO (NO) adsorption on the (3×1) surface). It must therefore be supposed that some CO (NO) is adsorbed also in the “bare” solitons.

More CO (NO) adsorption causes a further compression of the surface phase: the remaining bare solitons disappear and, for a coverage of $1/4 \text{ ML}$ a global (4×1) phase is observed.

In apparent contradiction with the fact that the oxygen atom in CO (NO) is higher on the surface (and therefore nearer to the tip) than Br, in most experimental

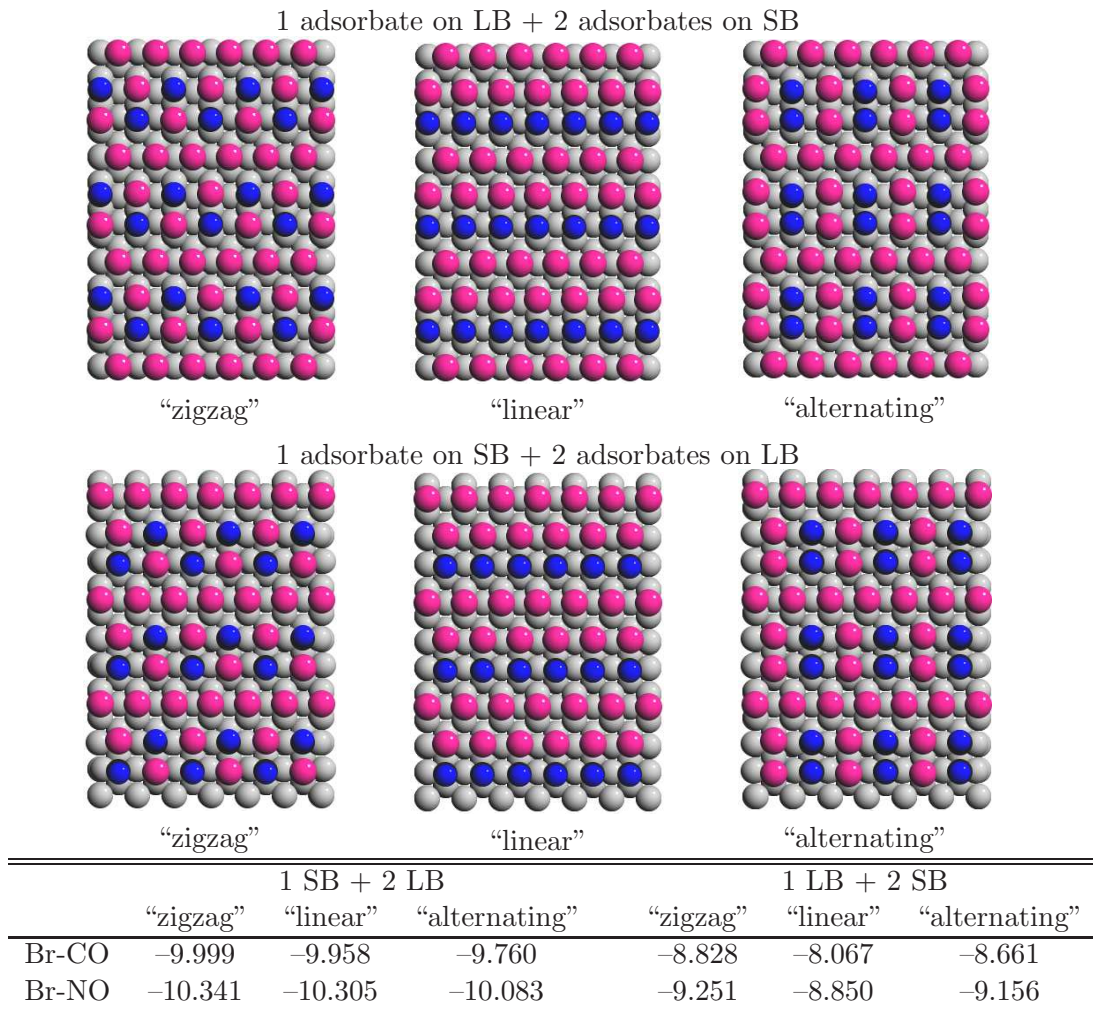


Figure 4.17: The (4×1)-CO (NO)/Br phase: Comparison among various arrangements. The adsorption energies per (4×2) cell are given in Å, referred to the clean unreconstructed Pt surface and to the free molecules. All arrangements with 1 LB + 2 SB are ruled out as is the 1 SB + 2 LB “alternating” system, due to the strong Br–Br repulsion in the $[1\bar{1}0]$ direction.

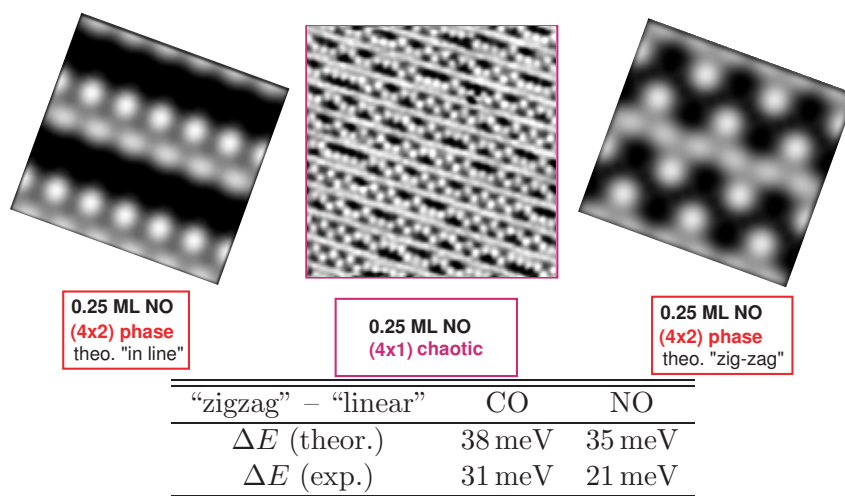


Figure 4.18: Experimental (middle panel) STM image of the CO (NO)-induced (4×1) phase compared with simulated ones showing “linear” and “zigzag” configurations with 1 adsorbate on SB and 2 adsorbates on LB per unit cell are ruled out as is the “alternating”

STM images, CO (NO) appears very dark and is almost indistinguishable from an empty site. This characteristic is reproduced by the present simulations. As can be seen in figure 4.19, the electronic states around oxygen are much more contracted than those around Br atoms. CO (NO) molecules appear thus as depressions of the density of states.

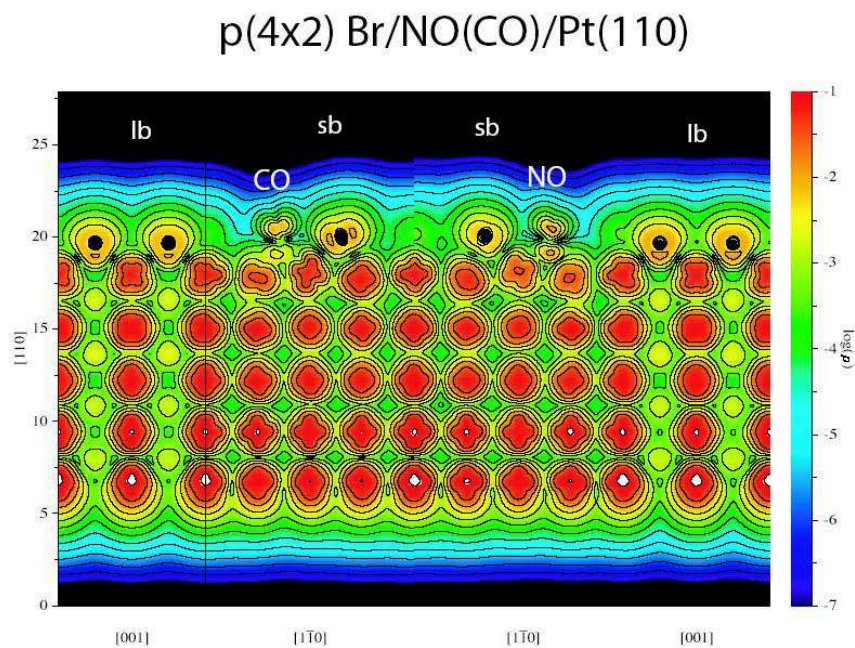


Figure 4.19: Calculated charge density across vertical sections of a CO (NO)-induced (4×1) phase. Even if O atoms lay higher, the electronic states around them are much more contracted than those around Br atoms, therefore CO (NO) molecules appear as depressions.

Chapter 5

Hydrogen adsorption on Pt(110)

The study of the interaction of hydrogen with transition metal surfaces is of fundamental importance. For example, hydrogen plays a central role in a multitude of technologically important catalytic reactions that occur on transition metal surfaces, such as hydrocarbon processing, hydrogenolysis and CO hydrogenation reactions [69]. Other topics of technological interest include hydrogen storage and the embrittlement of materials by hydrogen. More specifically, the H/Pt(110) system is known to be an excellent model system for Pt particles in H fuel cells [70, 71]. Furthermore, the anisotropic Pt(110) surface with adsorbate-covered modifications represents a promising template for the design and characterisation of one-dimensional systems on surfaces [72, 73, 74, 75, 76]. A precise knowledge of H bonding geometry and energetics is extremely desirable, for a detailed understanding of both the quasi one-dimensional properties of H/Pt(110) and the technological application of Pt in fuel cells and catalysis.

At the beginning of this study there was considerable disagreement with respect to the chemisorption site of H on Pt (110). The usual assumption of highly coordinated hydrogen [77, 78] sitting in the deep troughs of the missing rows was supported by work function measurements [79, 80] and vibrational spectroscopy [81], but was

challenged by the first direct structure-probing experiment (Helium atom scattering, HAS), which led to the proposal of a highly coordinated subsurface site [82]. Quite contrary to all these proposals, Low-energy electron diffraction (LEED) experiments together with the present study show evidence that hydrogen at low coverages (β_2 states) occupies adsorption sites above the outermost close-packed rows.

5.1 Computational Details

As in the rest of the present thesis, first-principles density-functional theory calculations have been performed with the projector augmented wave Vienna ab-initio simulation package (PAW-VASP) [13, 12]. Exchange-correlation was treated within the generalised gradient approximation (GGA) [11], yielding a bulk lattice constant of 3.984 Å. Repeated slabs of 11 Pt layers with an ad-layer of H atoms on the missing Pt-row side and a p(1×1) Pt termination on the other side were separated by a 12 Å thick vacuum layer. All layers were relaxed except three layers of the Pt substrate on the far side frozen to the relaxed geometry of a p(1×1)-Pt(110) surface. An energy cutoff of 250 eV and a 8×8×1 Monkhorst-Pack type k -point mesh was considered sufficiently accurate for the present purposes. The values of the adsorption energies are given per hydrogen atom with respect to its binding energy in the H₂ molecule. A well known inconvenience of GGA is its poorer performance for atomic and molecular as compared to bulk or adsorbate systems. In order to avoid systematic errors in the DFT adsorption energies, our GGA energies are taken to be the experimental values [83] $E_H^{at} = 13.60$ eV for the atom and $E_{H_2}^d = 4.75$ eV for the dissociation energy of the H₂ molecule, leading to a reduction of the GGA adsorption energies by 90 meV.

5.2 Discussion

First clues about the structure of the H/Pt(110) surface can be obtained by interpreting experimental results. Temperature programmed desorption and low-energy electron diffraction experiments were performed at the University of Innsbruck by M. Minca, Z. Zhang *et al.* [84, 85]. The TPD spectra obtained in the cited study (see figure 5.1) qualitatively show all features of data sets published previously by other groups [70, 79, 80, 86]: the well known β_2 and β_1 states [79, 80], and – at exposures above 400 L – the additional α -state [70, 86]. In figure 5.1, the open sym-

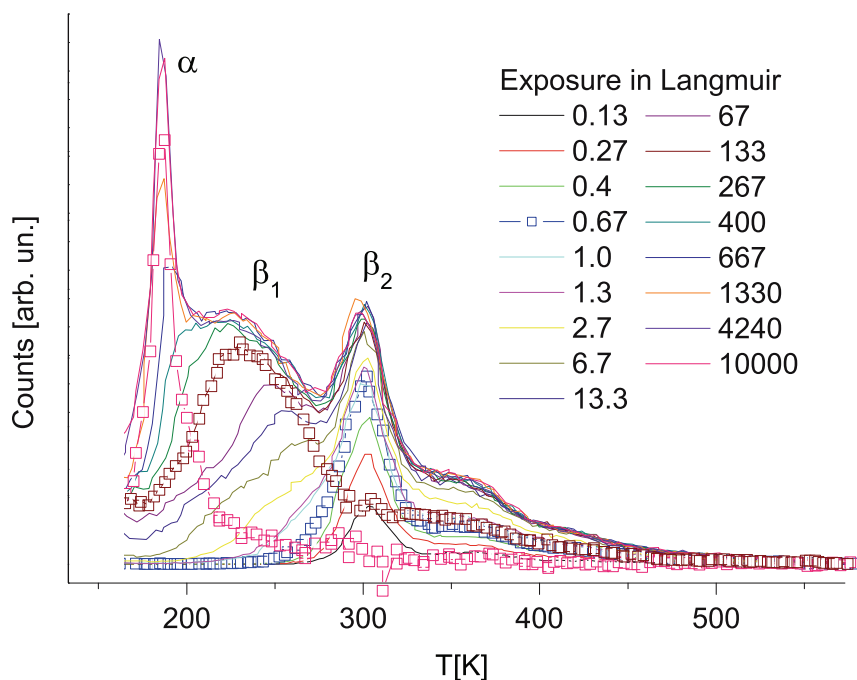


Figure 5.1: TPD spectra for D_2 . The exposure varies from 0.13 to 10000 L. Open symbols represent the principal components of the TPD spectrum at saturation (10000 L) divided into areas due to the α -state (pink symbols, integrated area 27% of total), the β_1 -state (brown, 51%), and the β_2 -state (blue, 22%). See text for a description of the decomposition. M. Minca *et al.* [85]

bols represent a tentative principal component analysis of the TPD at saturation

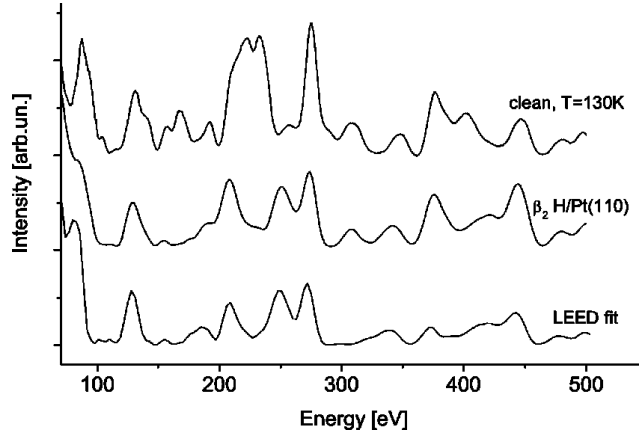


Figure 5.2: I/V curves for the $(1, 1/2)$ beam of the clean and β_2 -H-modified surface together with the best-fit calculation.

coverage. For separating the components, the TPD spectra at 0.67 L and 133 L are assumed to be solely due to the β_2 and the sum of β_2 and β_1 state, respectively. Consequently, the contributions of the β_1 and the α state are represented by the difference of the TPD spectra at 133 L minus 0.67 L and 10000 L minus 133 L, respectively. The partition is of course based on these assumptions and should not be taken too seriously. It is merely intended to show that the TPD at saturation is consistent with a relative ratio of 1:2:1 for $\beta_2:\beta_1:\alpha$ within the error bars of the experiment.

This partition agrees well i) with the approximate ratio of 1:2 for $\beta_2:\beta_1$ which has been found earlier [79], ii) with a CO coadsorption experiment blocking the β_2 state (see below, figure 5.9, and iii) with DFT calculations obtained in the present work (see below, figure 5.11).

According to the calibration of absolute coverage [79] and following the conclusions drawn in Ref. [79], this indicates a saturation coverage of 2 H atoms per (1×1) unit cell (2 ML) or 4 H atoms per missing-row (1×2) unit cell. For fcc(110) surfaces, the coverage in ML is usually referred to the (1×1) unit cell of the unreconstructed

surface which contains one substrate atom on the outermost row. However, these surfaces are quite “open”, the second and third layer atoms are still fairly exposed. Here, in the case of a missing-row reconstruction, the (1×2) unit cell contains four more or less exposed Pt atoms. The saturation coverage of 4 H atoms per (1×2) unit cell found in the cited work thus corresponds to one hydrogen atom per “exposed” Pt atom (see figure 5.11). This saturation coverage is roughly a factor of $4/3$ higher than was assumed previously [79].

5.2.1 The β_2 Surface

Both the clean and the hydrogen-covered Pt(110) surfaces are known to be missing row reconstructed [79]. However, LEED shows considerable difference in the I/V curves between them, indicating a substantial structural change in the surface geometry.[84]

The geometry parameters changed during the structural search are indicated in table 5.1: the first five interlayer distances d_{12} to d_{56} , the vertical bucklings b_3 and b_5 of the third and fifth layers and the lateral pairing amplitudes p_2 and p_4 between neighbouring atoms in $[001]$ direction within the second and fourth layers, as shown in figure 5.3. In order to avoid running into local minima during the fit procedure, the calculations for the hydrogen-modified surface were started both from the clean surface geometry (e.g., $d_{12} = 1.15 \text{ \AA}$) and from the considerably different bulk layer distances (e.g., $d_{12} = 1.38 \text{ \AA}$). In both cases, the same best-fit structure with a relaxation in between the two starting points (e.g., $d_{12} = 1.25 \text{ \AA}$) was obtained.

The calculated LEED intensities are in very good agreement with the experiment for the H-covered surface (see Fig. 5.2). The calculation with the best fit parameters yields a Pendry- R -factor of $R=0.24$ very similar to the clean surface.[40] These seemingly modest R -factors are among the best ever achieved for a fcc(110) surface.[40] The best fit parameters for the β_2 -H/Pt(110)- (1×2) surface are reported

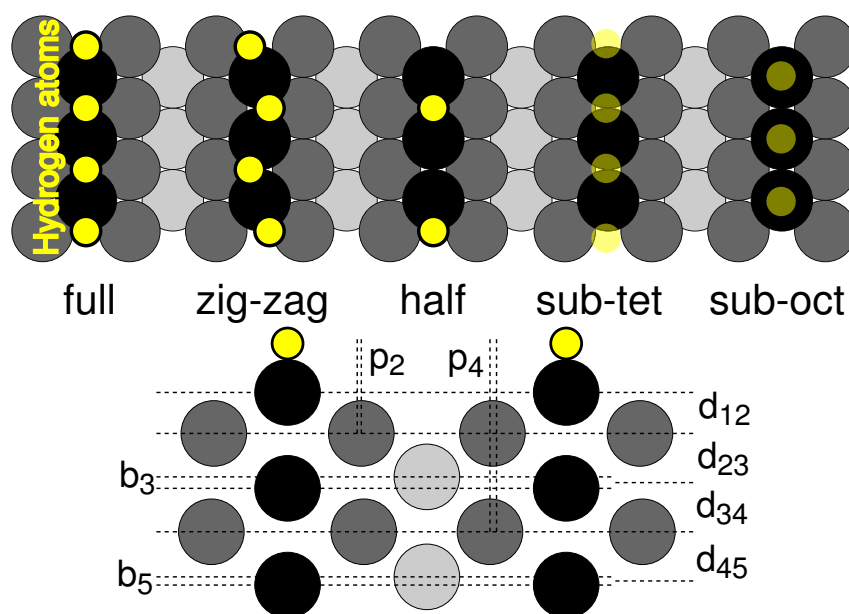


Figure 5.3: Model of the Pt atom geometry on clean and hydrogen-modified H/Pt(110)(1×2) surfaces with structural parameters determined. Typical H atom (yellow) arrangements used in the DFT calculations are denoted as full (β_2 -H), zigzag (slightly distorted β_2 -H to elucidate the effects of low energy lateral H displacements), and half (half-filled β_2 -H), respectively. Sub/surface arrangements considered are denoted as sub-tet (underneath the short-bridge sites) and sub-oct (directly underneath the atoms of the first Pt layer)

System	Pt(110)		β_2 -H-Pt(110)		
	Method	LEED	LEED	DFT	DFT
Ref.	clean	β_2 -H	full	zigzag	half
d_{12}	1.15	1.25	1.32	1.26	1.22
d_{23}	1.37	1.36	1.33	1.34	1.36
d_{34}	1.41	1.41	1.43	1.42	1.42
d_{45}	1.40	1.38	1.42	1.42	1.42
d_{56}	1.38	1.39	1.36	1.35	1.36
b_3	0.26	0.25	0.31	0.31	0.32
b_5	0.03	0.03	0.06	0.07	0.03
p_2	0.035	0.00	-0.022	0.006	0.004
p_4	0.065	0.05	0.057	0.053	0.064

Table 5.1: Experimental[84] and theoretical parameters for the missing-row structure of the clean and hydrogen-modified β_2 -H/Pt(110) (1x2) surface. $d_{i,i+1}$ denotes the (average) inter-layer spacing, while p_i and b_i denote the lateral pairing and buckling in layer i (all values in Å). Error limits for the parameters derived by the present LEED analysis (neglecting parameter correlations) are ± 0.02 Å for $\Delta d_{i,i+1}$, ± 0.05 Å for b_i and ± 0.07 Å for p_i . DFT(full):all top row bridge sites occupied, DFT(zigzag):all top row bridge sites occupied and displaced by 0.4 Å towards microfacets DFT(half): one half of top row bridge sites occupied. For easier comparison all DFT values have been scaled to the experimental bulk interlayer distance of $d_0 = 1.386$ ($d_0(DFT) = 1.409$)

in Table 5.1 together with the results of the DFT calculation. For comparison, the values for clean H/Pt(110)-(1×2) are also given.[40]

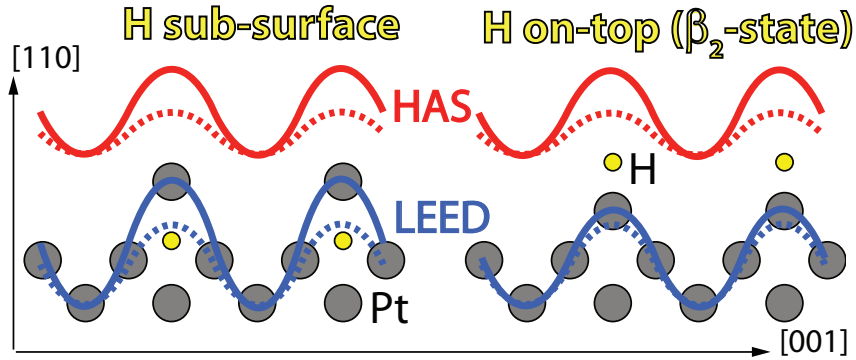


Figure 5.4: fig 3

It is important to notice that the substantial change of relaxation ($+0.1 \text{ \AA}$) provided both by DFT calculations and by LEED experiments is much less than the corrugation change ($+0.5 \text{ \AA}$) observed in the HAS experiment by Kirsten *et al.* [82]. This difference in corrugation and relaxation measured in the HAS and LEED experiments respectively, is precisely the experimental information pinpointing the adsorption site of the β_2 -hydrogen on Pt(110). As shown in Figs. 5.4 and 5.5, these experiments probe the geometry of the charge density at a very different level. The LEED electrons are essentially scattered by the ion cores of the platinum atoms. The dominant interaction here is the Coulomb potential. The helium atoms, in contrast, probe approximately contours of constant valence electron density at low charge density levels outside the surface. The dominant interaction in this case is the Pauli repulsion, preventing substantial overlap between the He and the substrate charge clouds.

In the case of hydrogen chemisorbed in a subsurface site below the outermost Pt row (Fig. 5.4, left; 5.5, c), the large change in corrugation measured by HAS would indicate a similar change in the outermost Pt-atom positions,[82] which is

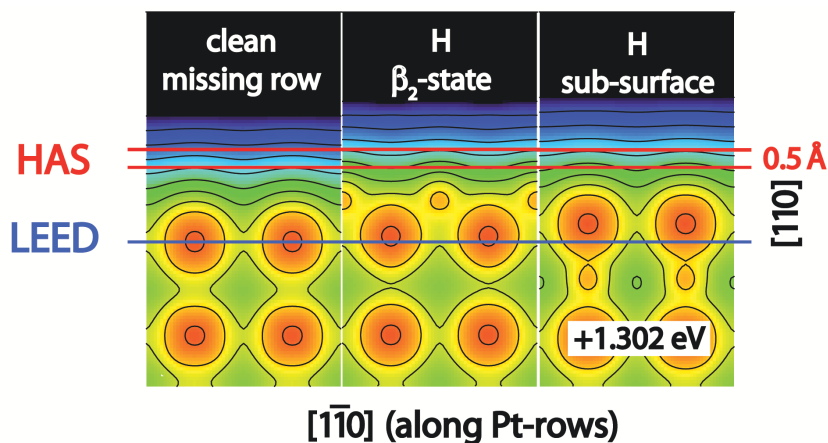


Figure 5.5: Calculated density of states (DOS) image: red is the maximum, black the minimum density, logarithmic scale. Elements probed by different experiments (surface DOS for HAS, atomic positions for LEED) are highlighted

not consistent with the cited LEED results. However, in the case of hydrogen adsorbing on top of the outermost row (top and/or short-bridge sites), the change in valence density corrugation is due to the position change of platinum atoms plus the hydrogen-induced electron density, whereas the LEED experiment measures the (smaller) change in the Pt-atom positions (Fig. 5.4, right). Thus only chemisorption sites above the outermost rows are consistent with the combined experimental evidence from LEED and HAS.

This conclusion is corroborated by the present DFT calculation of the adsorption geometry. In order to explore the dependency of the relaxation on coverage and H atom position, 44 different geometries were calculated. Generally, the calculation shows that both small H displacements from the ideal short bridge site and lower coverage lead to a lowering of the first substrate interlayer spacing (see some examples in Fig. 5.3 and Table 5.1). The strong coupling to both the hydrogen position and coverage is obviously the reason for the slight difference in interlayer spacing measured by LEED as compared to the ideal $T=0\text{K}$ fully occupied short bridge

geometry calculated.

The calculated energies, in fact, support the conclusions drawn from figure 5.4 and 5.5, that only on-row short-bridge adsorption sites are compatible both with HAS and LEED observations. On the other hand, the calculated interlayer spacing $d_{12} = 1.32 \text{ \AA}$ for a perfect $\beta_2\text{-H/Pt(110)}$ phase at 0.5 ML, is slightly bigger than the experimental $d_{12} = 1.25 \text{ \AA}$. Since the calculation does not include finite temperature effects, we calculated the dependency of the Pt relaxation and the chemisorption energy on the H atom position. The adsorption on sites along high symmetry surface lines — $(1\bar{1}0)$ direction and (001) direction— at different distances from the on-row short-bridge adsorption site was simulated. Table 5.2, shows the calculated inter-layer spacings and energies depending on the H positions on the surface, figure 5.7 shows the same energies, and the structure of the bonding for some adsorption sites described below.

$1\bar{1}0$	Position in $[001]$										
	0	5	10	15	20	25	30	35	40	45	50
Top	1.195 116	1.203 118	1.189 125	1.185 163	1.098 190	1.086 159	1.086 165	1.086 186	1.11 260	1.115 439	1.124 559
TB	1.2 169	1.198 173	1.203 178	1.149 213	1.107 125	1.099 193	1.094 202	1.089 185	1.077 236	1.108 333	1.064 415
Bridge	1.224 0	1.2 19	1.169 69	1.134 74	1.121 164	1.091 187	1.083 124	1.09 82	1.086 120	1.05 233	0.949 276

Table 5.2: Theoretical interlayer spacing (upper value, in \AA) and adsorption energies (lower value, in meV) relative to the short bridge site (absolute chemisorption energy $E_{sb} = -0.489 \text{ eV}$ per H-atom) of the hydrogen-modified $\beta_2\text{-H/Pt(110)}$ (1×2) surface at a coverage of 0.25 ML. Labels on columns (in percent of unit cell) and rows (top, tb, and bridge) refer to the H positions on the grid shown in Fig. 5.2.1.

It can be seen from both table 5.2 and figure 5.7, that the positions with highest binding energies are located in the vicinity of the Pt-row and correlate with the biggest interlayer spacings d_{12} . Adsorption in the trough is most unfavourable and leads to the lowest d_{12} . The energies and geometries as given in table 5.2 enable

an estimate of the potential landscape and to picture the diffusion and vibrational amplitudes of the hydrogen atom in correlation with d_{12} . The potential in the direction vertical to the bridge site (line b in figure 5.2.1, see figure 5.7 and lower row in table 5.2) is obviously very flat. The small energy differences (74 meV) for a shift of 15% perpendicular to the row allow for large vibrational amplitudes which are in turn intimately connected to the relaxation of the first Pt interlayer. Thus, we conclude that the difference between calculated and experimental interlayer spacings is mainly due to thermal motion of the hydrogen, which is strongly coupled to the Pt positions below. This large vibrational smearing might also explain the relatively small corrugation along the row measured by HAS which was taken as counter-evidence for the short bridge site [82].

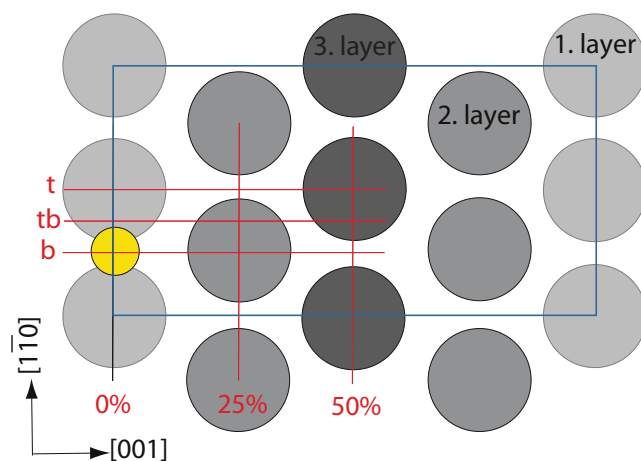


Figure 5.6: fig 5

Supporting the view of adsorption on SB-sites on the Pt rows, adsorption sites in the facets or in the trough give a much smaller $d_{12}=1.10 \text{ \AA}$, not consistent with the experiment (see figure 5.7). Sites inside the trough (fig. 5.7 d) are energetically (276 to 559 meV) in between the sites on top of the row and the (unstable) subsurface sites. On the (111) facets, the low coordinated site on top of the second layer Pt

atoms (fig. 5.7 c, 82 meV) is preferred over the higher coordinated sites (fig. 5.7 b, 130 to 180 meV). The data in table 5.2 and figure 5.7 establish also anisotropic diffusion: Whereas the effective barrier for diffusion along the rows is of the order of 120 to 160 meV, the activation barriers for diffusion perpendicular to the rows amount to roughly 280 meV. Besides, these last barriers are also a factor $2\sqrt{2}$ thicker than the first one. This behaviour is in contrast to H/Ni(110), where diffusion barriers are lower in the direction perpendicular to the rows [87].

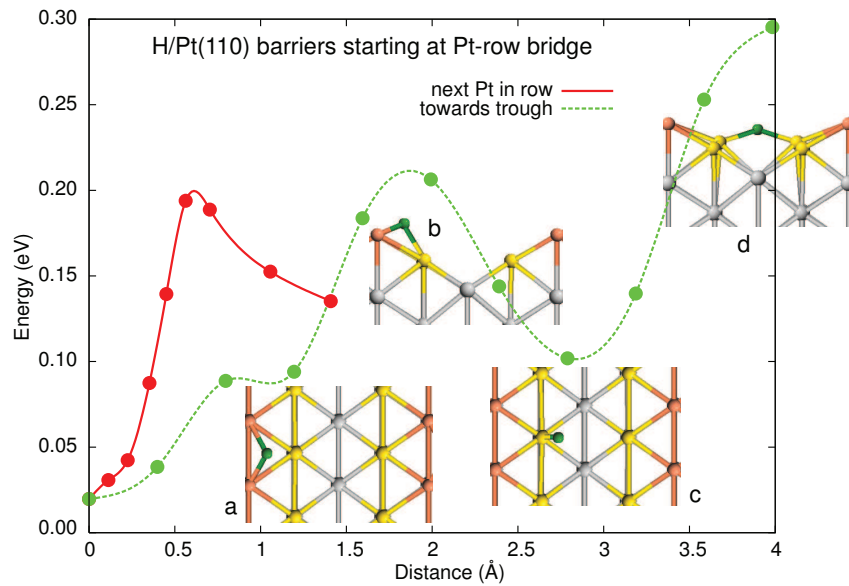


Figure 5.7: Adsorption energy calculated for different distances from the stable short-bridge adsorption site on the Pt row. The red full curve describes the variation in the $(1\bar{1}0)$ direction on the rim to the next on-top site, the green broken line the variation of the energy in the (001) direction to the middle of the trough.

Interestingly, and also in agreement with experiment,[79] the DFT calculation yields a small nearest neighbour attraction for hydrogen adatoms in the top-row bridge site. Thus, with increasing coverage, hydrogen occupies first all short bridge sites (β_2 state) before the sites in the troughs/microfacets are occupied (β_1 state). These results confirm an HREELS experiment of H/ Pt(110) [88] indicating a 2-fold

bridge site at low coverage.

The small induced work function change [79, 80] indicates a rather covalent bonding within the present model. In comparison, the most stable bonding site of H on Ni(110) and Pd(110) is the fcc pseudo-threefold site at the (111) microfacets of the (110) surface [87, 89]. The peculiar bonding characteristics of H on Pt can be attributed to a strong covalent interaction with the Pt d-orbitals. As it was suggested earlier in this work for Br/Pt(110) and also in a comparative study of CO-bonding on the transition metal surfaces [90], these bonding characteristics result from the relativistic contraction of the s-orbitals and the concomitant d-shell expansion. Independent support for the short bridge site as the preferred adsorption site can be found by preadsorption of CO as performed by M. Minca *et al.* [85]. As shown in figure 5.9, the β_2 -state in TPD is completely quenched by preadsorption of CO (exposure 0.66 L), whereas the β_1 -state and the shoulder at higher temperatures are not affected. Since CO is known to adsorb on top of the outermost Pt rows (s. also [63]), the quenching of the β_2 -state supports an adsorption site for hydrogen on the outermost row, too. As has been mentioned above, the CO coadsorption experiment can also be analysed with respect to the relative coverage of the β_2 state. Assuming that all β_2 adsorption sites have been blocked with CO, the difference curve in figure 5.9 should correspond to the contribution of the β_2 state.

5.2.2 Higher Coverages

Up to 1/4 ML adsorption occurs only on on-row SB sites as already shown. In the β_2 state, which corresponds exactly to a coverage of 1/4 ML, all these SB sites are occupied. At higher coverage, H must adsorb on other sites too. In order to find more convenient adsorption sites on the surface, an investigation of the adsorption potential was carried out. The results are shown in figure 5.8, which refers to a representative portion of the unit cell (see figure 5.2.1). On the (111) facets, the

low coordinated site (figure 5.7c) on top of the second layer Pt atoms (82 meV) is slightly preferred over the higher coordinated sites (figure 5.7b) (130 to 180 meV). The adsorption in the groove, on the contrary, is energetically much more expensive.

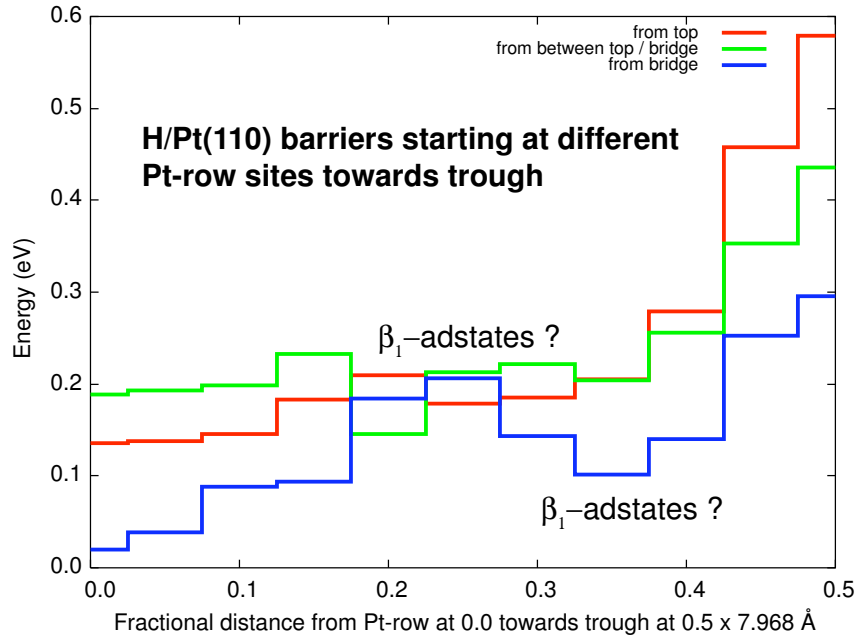


Figure 5.8: Adsorption energies for sites along three representative high-symmetry surface lines from the Pt-row to the groove: Starting from on-top of a Pt atom (in red, line t in fig 5.2.1), starting from between t and sb position (in green, line tb in fig 5.2.1 and starting from the sb position (in blue, line b in fig 5.2.1).

An integration of the curve in fig. 5.9 yields 20% of saturation coverage, which is —taking into account the crudeness of the approximation— agreeing reasonably well with the results discussed above. Judging from the same figure 5.9, the higher temperature feature at 350 K contains both, a tail and a shoulder related to the β_2 and the β_1 -state, supporting the partition as shown in figure 5.1. As has been discussed above, the cited TPD experiments — in agreement with some of the previous investigations [70, 86] — show clear evidence for the so-called α -state at the highest coverages. In the following, the occurrence of a new (1×4) superstructure

induced by these high coverages of hydrogen is discussed as seen in experiment to accompany the development of the sharp peak of the α -state in TPD.

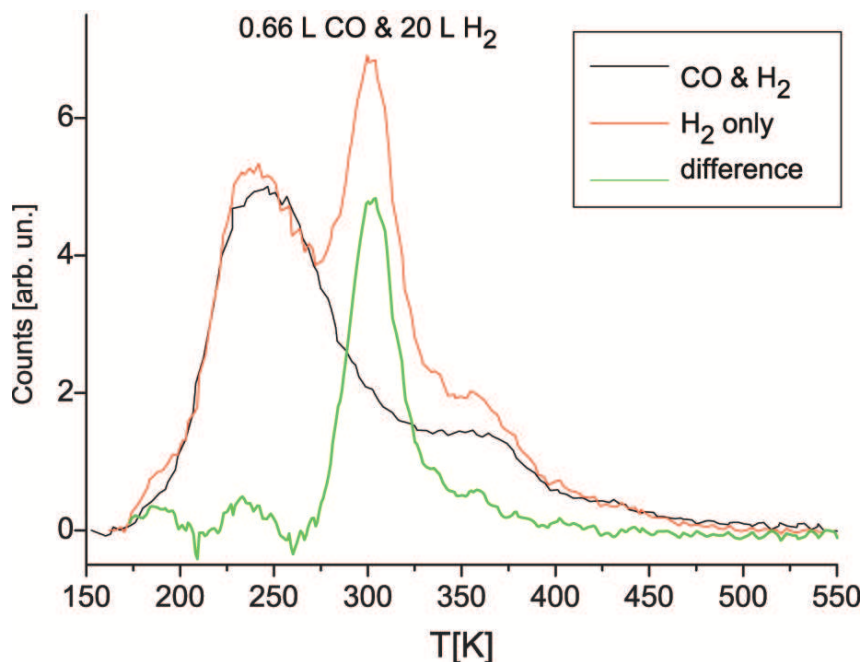


Figure 5.9: TPD spectra of H_2 with and without preadsorption of CO. The difference (green) of the TPD spectra of the H-covered surface (red) and the CO+H covered surface (black) is equivalent to the β_2 -state. M.Minca *et al.* [85]

Figure 5.10 shows the LEED patterns observed for three different coverages. At low LEED energies (49 eV), the (1×2) periodicity of the missing-row reconstruction remains unchanged up to exposures of 380 L. In a TPD of the same surface, the sharp peak related to the α -state is not yet observed, the coverage is evaluated to be about $0.84(\pm 0.04)$ of saturation. At higher exposures (840 and 1430 L), a very intense (1×4) spot becomes visible in LEED and the sharp α -state starts to develop in TPD (coverage $0.90(\pm 0.03)$ to $0.96(\pm 0.04)$). The LEED intensity decreases sharply for exposures higher than 2000 L (coverage $0.98(\pm 0.02)$), but is still clearly visible for highest exposures (7100 L, saturation coverage), whereas the α -state in TPD

increases up to saturation. Since the (1×4) spots in LEED at 49 eV are almost as intense as the (1×1) spots, it seems unreasonable to assign the (1×4) superstructure solely to a new periodicity within the overlayer of the (weakly scattering [78]) hydrogen atoms. Instead, the Pt(110) substrate atoms are involved in this reconstruction and the local cluster of rearranged Pt atoms around the additional α -state H atom is responsible for the diffraction spots. The local rearrangement as calculated by DFT is essentially a horizontal shift (see figure 5.11e) of the second layer Pt atoms towards the (red) α -state H-atom. Based on preliminary STM data, we speculate that a pairing row reconstruction is responsible for the 1×4 overstructure. The analysis of I/V-LEED experiments did not yield a conclusive result on the geometry, since the data-base is severely restricted by the small energy range where the 1×4 spots are clearly visible. A pairing row reconstruction has also been observed in the case of H/Ni(110) (see e.g. [87] and references therein) and is suggested to be one of the competing phases for the H induced (1×2) overstructure of H/Pd(110). Surprisingly, however, a possible row pairing in the present case would involve rows which are separated by almost 8 \AA due to the missing row reconstruction, and would indicate a rather long range interaction induced by the hydrogen. In order to complete the picture of H chemisorption on Pt(110), we calculated several geometries for 1.5 ML (β_1 -state) and 2.0 ML (α -state) hydrogen on the surface. Figure 8 summarises the results of our DFT calculations. The three different adsorption states (β_2 , β_1 and α) identified in the TPD spectra are confirmed by the calculations as well as the suggested saturation coverage partition of 1:2:1. The rather large difference in adsorption energies between the β_2 -hydrogen (figure 5.11a, white circles) and β_1 state (figure 5.11b, green circles) explains the predominant filling of the former at low coverages. For the β_1 state the situation is different, as filling the 111 pseudo-facets (figure 5.11c) is only by 22 meV less stable, suggesting considerable disorder upon heating, and making desorption from different sites possible (see also figure 5.11d),

consistent with a broader TPD signal.

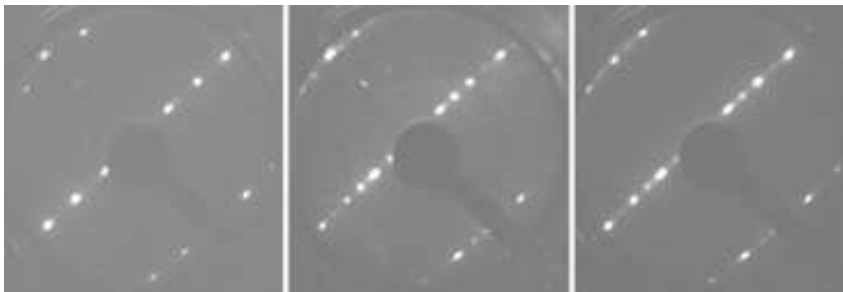


Figure 5.10: LEED diffraction patterns at $T = 130$ K and 49 eV electron energy after D_2 exposures of 380 L (left, 1×2 pattern), 840 L (middle, 1×4 pattern), and 7100 L (right, weaker 1×4 pattern). M. Minca *et al.* [85]

The first interlayer spacing ($d_{12}(1.5 \text{ ML}) = 1.23 \text{ \AA}$) is again less than in the β_2 -state ($d_{12}(0.5 \text{ ML}) = 1.32 \text{ \AA}$). This is consistent with the HAS experiment by Kirsten *et al.* [82], where a lowering of the corrugation at higher coverage has been found. The occupation of the β_1 state with two additional H atoms left and right of the missing row is plausible, since the distance between the H atoms is large enough to prevent a strong repulsion, and as shown in table 5.2, the trough states are not favourable. The latter fact is also evident from figure 5.11e, the α -state, where the additional H trough atom (red circle) induces a significant distortion of the Pt 111-like microfacets, leading to a row pairing of 0.4 \AA in the second Pt layer. In order to reduce the H–H repulsion on the 111 microfacets, the additional H atom has to be put in the troughs, which according to 5.2 costs 276 meV as compared with H in the the β_2 -state for a single atom. This is remarkably close to the adsorption energy difference for the additional α -H with respect to the full β_2 -H-layer ($489 - 192 = 297 \text{ meV}$) as moving the β_1 -H to the microfacets is easily accomplished, which makes repulsion between the α -H and the β_1 -H no longer an issue. Now, that the microfacets and trough sites are occupied, adding additional H (blue circles) strongly decreases the H–H distance as seen in figure 5.11f, which makes further

atomic adsorption unlikely.

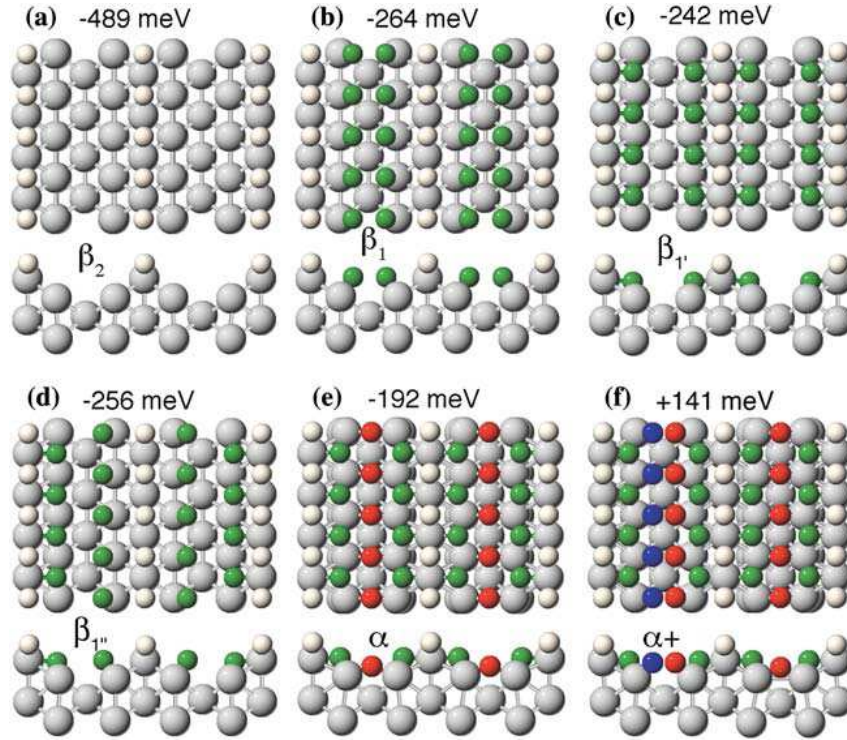


Figure 5.11: DFT-calculated adsorption energies for H on (1x2) Pt(110). Numerical values refer to the adsorption energy change per additional hydrogen atom (white, green, red, blue) in the specific adsorption site (β_2 , β_1 , α , $\alpha+$) and are given with respect to its binding energy in the H₂ molecule. The saturation coverage found in this work corresponds to full occupation of the α state as shown in e). There are 4 hydrogen atoms per (1x2) unit cell which translates to a nominal coverage of 2 ML.

5.2.3 Conclusions

In conclusion, the present study reveals an atypical binding site for H/Pt(110) at low coverage (β_2 -state), namely the low-coordinated short bridge site on the outermost row of the missing-row reconstructed substrate. Furthermore, a substantial derelaxation of the Pt(110) substrate and a strong coupling of the Pt lattice relaxation to the H atom position has been found. At higher coverages (β_1 -state), sites on the

(111) microfacets become occupied. For exposures higher than approximately 400 L the α -state is evident in the TPD experiments. The relative weight of the three states is near to 1:2:1 and the absolute coverage is compatible to 1:2:1 H atoms per 1×2 unit cell. Thus, the saturation coverage is higher than previously assumed and amounts to 4 H atoms per (1×2) unit cell. At low LEED energies, a distinct (1×4) pattern develops in the coverage range of the α -state.

Conclusions

In the following the most important results achieved in this work are summarised.

The Density-Functional-Theory based Vienna Ab-initio Simulation Package (VASP) in the Generalised Gradient Approximation (GGA) was used to investigate pure halogen (particularly bromine and chlorine) adsorption, halogen CO (NO) co-adsorption, as well as hydrogen adsorption on a Pt(110) surface.

In the first chapter, the clean Pt surface is characterised, both as a check-up of the computational setup and as substrate for the adsorbate systems. The correct relaxations are obtained, and they are, as well as the binding energy, independent of the size of the unit cell. Following that, the adsorption of halogens at low coverage is investigated. The already known general trends in the single adsorbate approximation (1/4 ML coverage) were confirmed with both adsorption energy and Hal-Pt bond-length increasing in the order $\text{Cl} < \text{Br} < \text{I}$. The increase of bond-length reflects the increasing covalent radius of the halogen.

At 1/2 ML coverage, Cl is found to prefer a $p(2 \times 1)$ arrangement, while I prefers a $c(2 \times 2)$ configuration. Both are characterised regarding geometry and electronic structure. For Br both configurations are energetically degenerate and a third phase with (3×2) periodicity is found very close in energy. A DFT study of next-neighbours interactions and of vibration potentials allows to shed some light on the observed temperature-dependent fluctuations and phase separations.

In the second chapter the phase transitions $c(2\times 2) \Rightarrow (3\times 1) \Rightarrow (4\times 1)$ are investigated for a Br adsorbate and the global (3×1) and (4×1) phases are analysed. A quite good agreement with experiment, both LEED and STM is found. In particular, the interpretation of the Br- (3×1) phase between 1/2 and 2/3 ML coverage as the time average of a fluctuating (3×2) phase and the characterisation of the (4×1) phase are important findings.

The phase transitions occurring after adsorption of Cl at higher than 1/2 ML coverages are also investigated. Cl is found to show the same (3×1) and (4×1) phases as Br, but due to its higher corrosive potential, as compared to Br, it already tears up Pt atoms from the substrate and forms a new phase best described as a (4×2) -PtCl₄/Cl/Pt(110) phase.

The adsorption of Cl on the $c(2\times 2)$ -Br/Pt surface makes the surface to undergo the same $c(2\times 2) \Rightarrow (3\times 1)$ transition observed for pure Br, with Cl atoms residing preferentially on SB positions.

In the third chapter, adsorption of CO (NO) on both a clean and on a $c(2\times 2)$ -Br/Pt surface is investigated. At low coverages, CO and NO leaves the MR-reconstructed Pt(110) surface intact. The most stable adsorption site is for both the SB position on the first layer rows. For CO this position is energetically degenerate with the neighbouring Top site. The adsorption of CO is particularly interesting because the corresponding diffusion energy barrier is untypical: non sinusoidal with a maximum between SB and Top positions and lower.

On the unreconstructed (1×1) -Pt surface, both CO and NO adsorb on SB sites. Compared to the halogens, CO and NO show a higher preference for SB on LB sites and a lower next-neighbour repulsion. Here again, Top is the second preferred position for CO.

The adsorption of CO (NO) on the $c(2\times 2)$ -Br/Pt surface leads to the same

$c(2\times 2) \Rightarrow (3\times 1)$ transition as observed for pure Br. The transition takes place at very low CO(NO) coverage. The $(3\times 1) \Rightarrow (4\times 1)$ transition is more complex than for pure Br, and shows many intermediate ordered ((7×1) , (6×1)) and disordered phases. Regarding the occupation of SB and LB sites the global CO(NO)/Br- (4×1) phase is inverted with respect to the pure Br- (4×1) phase.

The fourth chapter deals with the adsorption of hydrogen on the MR reconstructed Pt(110) surface.

The present study reveals an atypical binding site for H/Pt(110) at low coverage (β_2 -state), namely the low-coordinated short bridge site on the outermost row of the missing-row reconstructed substrate. Previously hypothesised sub-surface adsorption sites are ruled out. At higher coverages (β_1 -state), sites on the (111) microfacets become occupied. For even higher exposures the α -state is formed. The relative weight of the three states is near to 1:2:1 and the absolute coverage is compatible to 1:2:1 H atoms per 1×2 unit cell. Thus, the saturation coverage is higher than previously assumed and amounts to 4 hydrogen atoms per (1×2) unit cell.

Bibliography

- [1] M. Imada, A. Fujimori, and Y. Tokura, *Rev. Mod. Phys.* **70**, 1039 (1998).
- [2] J. Voit, *Rep. Prog. Phys.* **57**, 977 (1994).
- [3] T. Valla, P. D. Johnson, Z. Yusof, B. Wells, Q. Li, S. M. Loureiro, R. J. Cava, M. Mikami, Y. Mori, M. Yoshimura, and T. Sasaki, *Nature(London)* **417**, 627 (2002).
- [4] P. Segovia, D. Purdie, M. Hengsberger, and Y. Baer, *Nature(London)* **402**, 504 (1999).
- [5] P. Hohenberg and W. Kohn, *Phys. Rev. B* **136**, 864 (1964).
- [6] W. Kohn and L. J. Sham, *Phys. Rev.* **140**, A1133 (1965).
- [7] L. J. Sham and M. Schlüter, *Phys. Rev. B* **32**, 3883 (1985).
- [8] O. Gunnarson and B. I. Lundqvist, *Phys. Rev. B* **13**, 4274 (1976).
- [9] R. M. Dreizler and E. K. U. Gross, *Density Functional Theory* (Springer-Verlag, Berlin-Heidelberg, 1990), p. 177.
- [10] J. P. Perdew and A. Zunger, *Phys. Rev. B* **23**, 5048 (1981).
- [11] Y. Wang and J. P. Perdew, *Phys. Rev. B* **44**, 13298 (1991).
- [12] <http://cms.mpi.univie.ac.at/CMSPage/main/>.
- [13] G. Kresse and J. Furthmüller, *Phys. Rev. B* **54**, 11169 (1996).
- [14] D. R. Hamann and C. C. M. Schlüter, *Phys. Rev. Lett.* **43**, 1494 (1979).
- [15] D. R. Hamann, *Phys. Rev. B* **40**, 2980 (1989).
- [16] D. Vanderbilt, *Phys. Rev. B* **41**, 7892 (1990).

-
- [17] G. Binnig, H. Rohrer, C. Gerber, and E. Weibel, *Appl. Phys. Lett.* **40**, 178 (1982).
- [18] G. Binnig, H. Rohrer, C. Gerber, and E. Weibel, *Phys. Rev. Lett.* **49**, 57 (1982).
- [19] C. J. Chen, *Introduction to Scanning Tunneling Microscopy* (Oxford University Press, New York, 1993).
- [20] W. Hofer, Ph.D. thesis, CMS-TU Wien, 1999.
- [21] J. Tersoff and D. R. Hamann, *Phys. Rev. Lett.* **50**, 1998 (1983).
- [22] J. Tersoff and D. R. Hamann, *Phys. Rev. B* **31**, 805 (1985).
- [23] J. Bardeen, *Phys. Rev. Lett.* **6**, 57 (1961).
- [24] N. D. Lang, *Phys. Rev. B* **34**, 5947 (1986).
- [25] A. A. Lucas, *Europhys. News* **21**, 63 (1990).
- [26] H. Lüth, *Solid Surfaces, Interfaces and Thin Films* (Springer-Verlag, Berlin Heidelberg, New York, NY, 2001).
- [27] A. Zangwill, *Physics of Surfaces* (Cambridge University Press, ADDRESS, 1988).
- [28] C. Deisl, Ph.D. thesis, Leopold-Franzens-Universität Innsbruck, 2004.
- [29] H. Pfnür, C. Voges, K. Budde, and L. Schwenger, *Prog. Surf. Sci.* **53(2-4)**, 205 (1997).
- [30] K. Swamy, P. Hanesch, P. Sandl, and E. Bertel, *Surf. Sci.* **466**, 11 (2000).
- [31] C. Deisl, K. Swamy, N. Memmel, E. Bertel, C. Franchini, G. Schneider, J. Redinger, S. Walter, L. Hammer, and K. Heinz, *Phys. Rev. B* **69**, 195405 (2004).
- [32] E. Donà, T. Loerting, S. Penner, M. Minca, A. Menzel, E. Bertel, J. Schoiswohl, S. Berkebile, F. P. Netzer, R. Zucca, and J. Redinger, *Surf. Sci.* **601**, 4386 (2007).
- [33] Z. Nussinov, I. Vekhter, and A. Balatsky, *cond-mat* 0409474 (2004).
- [34] F. Guinea, G. Gómez-Santos, and D. Arovas, *Phys. Rev. B* **62**, 391 (2000).
- [35] H. Ibach, *Surf. Sci. Rep.* **29**, 193 (1997).

-
- [36] C. Franchini, Ph.D. thesis, Technische Universität Wien, Institut für Allgemeine Physik, 2002.
- [37] P. J. Feibelman, *Phys. Rev. B* **51**, 17867 (1995).
- [38] H.-J. Brocksch and K. H. Bennemann, *Surf. Sci.* **161**, 321 (1985).
- [39] S. M. Foiles, M. I. Baskes, and M. S. Daw, *Phys. Rev. B* **33**, 7983 (1986).
- [40] V. Blum, L. Hammer, K. Heinz, C. Franchini, J. Redinger, K. Swamy, C. Deisl, and E. Bertel, *Phys. Rev. B* **65**, 165408 (2002).
- [41] P. Fery, W. Moritz, and D. Wolf, *Phys. Rev. B* **38**, 7275 (1988).
- [42] E. C. Sowa, M. A. V. Hove, and D. L. Adams, *Phys. Rev. B* **199**, 174 (1988).
- [43] P. Fenter and T. Gustafsson, *Phys. Rev. B* **38**, 10197 (1988).
- [44] E. Vlieg and I. K. Robinson, *Surf. Sci.* **233**, 248 (1990).
- [45] M. Stock, J. Risse, U. Korte, and G. Meyer-Emsen, *Surf. Sci.* **233**, L243 (1990).
- [46] U. Korte and G. Meyer-Ehmsen, *Surf. Sci.* **271**, 616 (1992).
- [47] E. Donà, T. Loerting, S. Penner, M. Minca, A. Menzel, E. Bertel, J. Schoiswohl, S. Berkebile, F. P. Netzer, R. Zucca, and J. Redinger, *Surf. Sci.* **601**, 4386 (2007).
- [48] E. Donà, T. Loerting, S. Penner, M. Minca, A. Menzel, E. Bertel, J. Schoiswohl, S. Berkebile, F. P. Netzer, R. Zucca, and J. Redinger, *Phys. Rev. Lett.* **98**, 186101 (2007).
- [49] P. A. Lee, T. M. Rice, and P. W. Anderson, *Phys. Rev. Lett.* **31**, 462 (1973).
- [50] R. H. McKenzie, *Phys. Rev. B* **52**, 16428 (1995).
- [51] J. Orenstein and A. J. Millis, *Science* **288**, 468 (2000).
- [52] E. Donà, Ph.D. thesis, Leopold-Franzens-Universität Innsbruck, 2007.
- [53] C. Deisl, E. Dona, S. Penner, M. Gabl, E. Bertel, R. Zucca, and J. Redinger (unpublished).
- [54] K. Swamy, C. Deisl, A. Menzel, R. Beer, S. Penner, and E. Bertel, *Phys. Rev. B* **65**, 121404 (2002).

-
- [55] C. Deisl, K. Swamy, R. Beer, A. Menzel, and E. Bertel, *J. Phys.: Condens. Matter* **14**, 4199 (2002).
- [56] A. Menzel, Z. Zhang, M. Minca, T. Lrting, C. Deisl, and E. Bertel, *New J. Phys.* **7**, 102 (2005).
- [57] R. Beer, Ph.D. thesis, Universität Innsbruck, 2003.
- [58] S. Ohba, S. Sato, and Y.Saito, *Acta Cryst.* **B39**, 49 (1983).
- [59] J. M. Carpinelli, H. H. Weitering, E. W. Plummer, and R. Stumpf, *Nature* **381**, (1996).
- [60] P. J. Feibelman, B. Hammer, J. K. Nørskov, F. Wagner, M. Scheffler, R. Stumpf, R. Watwe, and J. Dumesic, *J. Phys. Chem. B* **105**, 4018 (2001).
- [61] M. Gajdoš, A. Eichler, and J. Hafner, *J. Phys.: Condens. Matter* **16**, 1141 (2004).
- [62] R. von Glan and U. Korte, *Surf. Sci.* **375**, 353 (1997).
- [63] R. K. Sharma, W. A. Brown, and D. A. King, *J. Chem. Phys.* **414**, 6876 (1998).
- [64] Q. Ge and D. A. King, *J. Chem. Phys.* **111**, 9461 (1999).
- [65] W. A. Brown, Q. Ge, R. K. Sharma, and D. A. King, *Chem. Phys. Lett.* **299**, 253 (1999).
- [66] G. Kresse, A. Gil, and P. Sautet, *Phys. Rev. B* **68**, 073401 (2003).
- [67] C. Deisl, Master's thesis, Leopold-Franzens-Universität Innsbruck, 2000.
- [68] C. Deisl, K. Swamy, S. Penner, and E. Bertel, *Phys. Chem. Chem. Phys.* **3**, 1213 (2001).
- [69] M. Fuchs, B. Jenewein, S. Penner, K. Hayek, G. Rupprechter, D. Wang, R. Schlögl, J. Calvino, and S. Bernal, *Appl. Cat. A* **294**, 279 (2005).
- [70] C. Lu and R. I. Masel, *J. Phys. Chem. B* **105**, 9793 (2001).
- [71] W. Chrzanowski and A. Wieckowski, *Langmuir* **14**, 1967 (1998).
- [72] P. Segovia, D. Purdie, M. Hengsberger, and Y. Baer, *Nature* **402**, 504 (1999).
- [73] A. Mugarza, A. Mascaraque, V. Prez-Dieste, V. Repain, S. Rousset, F. J. G. de Abajo, and J. Ortega, *Phys. Rev. Lett.* **87**, 107601 (2001).

-
- [74] N. Nilius, T. M. Wallis, and W. Ho, *Science* **297**, 1853 (2002).
- [75] W. Widdra, P. Trischberger, and J. Henk, *Phys. Rev. B* **60**, R5161 (1999).
- [76] W. Widdra, *Appl. Phys. A* **72**, 395 (2001).
- [77] G. Burns, *Solid State Physics* (Academic, New York, 1985).
- [78] K. Christmann, *Surf. Sci. Rep.* **9**, 1 (1988).
- [79] J. R. Engstrom, W. Tsai, and W. H. Weinberg, *J. Chem. Phys.* **87**, 3104 (1987).
- [80] C. Shern, *Surf. Sci.* **264**, 171 (1992).
- [81] W. Stenzel, S. Jahnke, Y. Song, and H. Conrad, *Prog. Surf. Sci.* **35**, 159 (1991).
- [82] E. Kirsten, G. Parschau, W. Stocker, and K. H. Rieder, *Surf. Sci.* **231**, L183 (1990).
- [83] S. Wilke, D. Hennig, and R. Löber, *Phys. Rev. B* **50**, 2548 (1994).
- [84] M. Minca, C. Deisl, T. Loerting, A. Menzel, E. Bertel, R. Zucca, and J. Redinger, *Phys. Rev. B* **70**, 121401 (2004).
- [85] M. Minca, S. Penner, T. Loerting, A. Menzel, E. Bertel, R. Zucca, and J. Redinger, *Topics in Catalysis* **46**, 161 (2007).
- [86] G. Anger, H. F. Berger, M. Luger, A. W. S. Feistritz, and K. D. Rendulic, *Surf. Sci.* **219**, L583 (1989).
- [87] G. Kresse and J. Hafner, *Surf. Sci.* **459**, 287 (2000).
- [88] W. Stenzel, S. Jahnke, Y. Song, and H. Conrad, *Progress in Surf. Sci.* **35**, 159 (1991).
- [89] W. Dong, V. Ledentu, P. Sautet, E. Eichler, and J. Hafner, *Surf. Sci.* **411**, 123 (1998).
- [90] E. Bertel, N. Memmel, G. Rangelov, and U. Bischler, *Chem. Phys.* **177**, 337 (1993).

Credits

First I would like to thank my supervisor Josef “Sepp” Redinger for his scientific and personal help. And, of course, for his infinite patience.

A sincere thank also to all other members of the scientific college: Especially to Peter Mohn for his help in settling down in Vienna and the very useful discussions. Mostly about opera. To Peter Weinberger, the kind and gentle appearance of authority. To Raimund Podloucky, who made me discover Richard Strauss etc.

And I’d like to mention some of the colleagues too: Robert and Jan, who tried in vain to get from me information about Italian football, Vladan and Jaime, and then Sergei and Tanja, Martin and Hannes, who were such nice neighbours. And Corina, who helped me to protract my lunch breaks to an unprecedented extent. And I’m sure I’m forgetting someone.

A special, special thank to Maria, who was not just a secretary, but almost a second mother (and not just to me, I’m sure).

Of course I’d like to thank all my friends: people who i knew already before I came to Vienna, whom I missed most of the time, and with whom I managed to keep in contact during all this time despite the distance, ant the ones I first met here in Vienna, and whom I will surely miss, if I ever leave the city.

And last but not least, my family, the best and most supportive of all possible families, who always showed an incredible confidence in me. Despite of everything.

And and and... This short list of people I would like to express my gratitude to

can by no mean be considered complete.

Vita

Surname: Zucca
Given Name: Rinaldo

Place of Birth: Cagliari, Italy
Date of Birth: July 25th, 1977
Citizenship: Italian
Marital status: single
Parents: Slvana Sulis, Francesco Zucca

Present address: Institut für Allgemeine Physik
Center for Computational Materials Science
Technische Universität Wien
Getreidemarkt 9, A-1060 Vienna, Austria
Tel. +43-1-58801-15837

Private address: Ehrenfelsgasse 8/9, 1120 Wien, Austria
Tel. +43-1-9051294

E-mail: rz@cms.tuwien.ac.at

EDUCATIONAL

Liceo Scientifico L.B.Alberti di Cagliari, Italia	1991-1996
MS, Physics: Università degli Studi di Cagliari, Italia	1996-2002
PhD, Physics: Technische Universität Wien, Österreich	2003-2007

Publications:

1. Z. Zhang, M. Minca, C. Deisl, T. Loerting, A. Menzel, E. Bertel, **R. Zucca**, and J. Redinger, *H on Pt(110): An atypical chemisorption site at low coverages*, Phys. Rev. **B70**, (2004) 153403.
2. A. Menzel, Z. Zhang, M. Minca, E. Bertel, J. Redinger, and **R. Zucca**, *Switching between coherent and incoherent electronic states*, J. Phys. Chem. Solids **67**, (2006) 254-258.
3. M. Minca, S. Penner, T. Loerting, Z. Zhang, A. Menzel, E. Bertel, **R. Zucca**, and J. Redinger, *Chemisorption of hydrogen on the missing row Pt(110)-(1x2) surface*, Topics in Catalysis Vol. **46**, (2007) 161-167.
4. E. Dona, T. Loerting, S. Penner, M. Minca, A. Menzel, E. Bertel, J. Schoiswohl, S. Berkebile, F. P. Netzer, **R. Zucca** and J. Redinger, *Fluctuations and Phase Separation in a Quasi-One-Dimensional System*, Phys. Rev. Lett. **98**, (2007) 186101-4.
5. E. Dona, T. Loerting, S. Penner, M. Minca, A. Menzel, E. Bertel, J. Schoiswohl, S. Berkebile, F. P. Netzer, **R. Zucca** and J. Redinger, *Fluctuations and phase separation in Br/Pt(110)*, Surf. Sci. **601**, (2007) 4386-4389.

Conference presentations and seminars:

1. R. Zucca, C. Franchini, and J. Redinger
Halogen adsorption on the Pt(110) surface: structure and stability of mixed Br/CO phases,
XXII Convegno di sica Teorica e Struttura della Materia,
Fai della Paganella, Italy, March 20-23, 2003.
2. R. Zucca and J. Redinger
Mixed Br/CO adsorbate phases on Pt(110),
XIII. Workshop of Computational Materials Science,
Geremeas(CA), Italy, September, 13.-18., 2003.
3. R. Zucca, *NO/CO adsorption on halogen precovered Pt(110): DFT studies*,
CMS Science College Seminar,
Vienna, Austria, May 24, 2004
4. R. Zucca and J. Redinger,
CO/NO adsorption on halogen precovered Pt(110): DFT studies,

IVC 16 - 16th International Vacuum Congress,
Venice, Italy June 28 - July 2, 2004.

5. R. Zucca and J. Redinger
NO/CO adsorption on halogen precovered Pt(110): DFT studies,
XIV. Workshop on Computational Materials Science,
Geremeas(CA), Italy, September 18-23, 2004.
6. R. Zucca and J. Redinger
NO/CO adsorption on halogen precovered Pt(110): DFT studies,
1st workshop "Nano Science on Surfaces",
Schloss Seggau, Austria, October 18-20, 2004.
7. R. Zucca, C. Franchini, J. Redinger, C. Deisl, T. Loerting, A. Menzel, and E. Bertel
The Structure of Chlorine Phases on a Platinum(110) Surface,
ICSOS 8 The 8th International Conference on the Structure of Surfaces,
Munich, July 18 - 22, 2005.
8. R. Zucca, C. Franchini, J. Redinger, C. Deisl, T. Loerting, A. Menzel, and E. Bertel
The Structure of Halogen Phases on a Platinum(110) Surface,
ECOSS 23 European Conference on Surface Science,
Berlin, September 49, 2005.